The Dissertation Committee for Emanuel Norbert Lissek
certifies that this is the approved version of the following dissertation:

Advanced Imaging of Biopolymer Networks and Filaments to Resolve Structure, Filament-level Mechanics, and Cell-matrix Interactions

Committee:

Ernst-Ludwig Florin, Supervisor

Vernita Gordon

Michael Marder

Aaron Baker

Manfred Fink

Advanced Imaging of Biopolymer Networks and Filaments to Resolve Structure, Filament-level Mechanics, and Cell-matrix Interactions

by

Emanuel Norbert Lissek

DISSERTATION

Presented to the Faculty of the Graduate School of
The University of Texas at Austin
in Partial Fulfillment
of the Requirements
for the Degree of

DOCTOR OF PHILOSOPHY

THE UNIVERSITY OF TEXAS AT AUSTIN
December 2018

for my parents

Acknowledgments

I am deeply grateful to my supervisor Prof. Ernst-Ludwig Florin for having given me the opportunity to work in his lab. E.-L. never picks the 'boring', safe route in his pursuit of knowledge, rather he is full of novel ideas and chooses the exciting and more intriguing path of science. I very much benefited from and enjoyed his mentorship and guidance.

Fellow lab member and office mate Aaron Foote has become one of my best friends over the years. Countless discussions on life and politics expanded my mind and helped me understand many angles and viewpoints not previously considered. I admire very much his confidence and sense of self that he holds and will always value his advice.

Dr. Tobias Bartsch was a member of the lab until 2013 and trained me during my first year in graduate school. His Ph.D. work was crucial in building the instrument and developing the method that I started working with. He also played a significant role in obtaining the results and developing the techniques that are described in this work. Tobias has an unstoppable drive and motivation, that served as a tremendously helpful source of inspiration during my time in graduate school. I have great respect for his work ethic and intellect. He became a very close friend over the years, whose advise and company I very much cherish outside and inside the lab. Likewise I want to thank Dr. Martin Kochanczyk, also former member of the FlorinLab, who laid the groundwork for my research by developing and building most of the optical tweezer based microscope that I was fortunate enough to have inherited for my time in graduate school. His attention to detail showed in the quality during the development process and his advise and help made my work a lot easier.

I cannot thank enough my parents, who throughout my entire life have given everything to create possibilities for me to be successful in life. Their unconditional love and support, and constant encouragement keeps me striving to make them proud. Thank you.

My sister Susanna, while living across the Atlantic was never but a phone call away. Her continued support and advice cannot be overstated. Her and I share our love for animals and the desire to end their senseless exploitation, in food, clothing, science or entertainment. I am extremely proud of her achievements to date and can't wait to see her grow even further.

I am eternally grateful to Margaret and Lynn Dixon who accepted me as a part of their family back in 2004 during a high school exchange program and first taught me the American way of life. Both have helped and supported me tremendously over the years and continue to be very close friends. Thank you.

Michael Himmelsbach spent countless hours helping me to align optical components and shared the photonic force microscope with me. Of course I also want to mention the remaining current and past members of the Florin-Lab: Daniel Losowyj, Suzanne Jacobs, Irakli Gudavaze, Dr. Sara Cheng and Dr. Guilherme Nettesheim who made the lab a fun, positive and supportive environment to work in.

A big thank you also to the entire Center for Nonlinear Dynamics, and especially Prof. Harry L. Swinney and Olga Vera, who deserve special mention for keeping everything running smoothly and making this place special.

My gratitude is also owed to Manuel Lindel, Katharina and Johann Schmidt who made my undergraduate studies in Leipzig so special and memorable and continue to be good friends today.

And last but not least I want to mention three very influential teachers during my time in high school. Jürgen Parsch, and Dietmar Werchner, who both instilled in me my love for the natural sciences, and especially physics by constantly challenging me with, at the time new, and mind-boggling experiments. And also the late Wolfgang Kammel, who inspired and shaped my love for music, be it listening to, understanding, or playing it. He also was an inspiring role model for what it means to be a honorable man.

I am deeply and eternally grateful to all these individuals and many more. It is truly amazing to be alive in this wonderful world today and to have the opportunity to live and work for my dreams.

Advanced Imaging of Biopolymer Networks and Filaments to Resolve Structure, Filament-level Mechanics, and Cell-matrix Interactions

Publication No. ________________

Emanuel Norbert Lissek, Ph.D.
The University of Texas at Austin, 2018

Supervisor: Ernst-Ludwig Florin

The extracellular matrix (ECM) makes up the environment of many cells in our body and gives tissues their stability. It is comprised of highly non-linear fibrous biopolymer networks which display unique mechanical properties, such as stiffening by several orders of magnitude under strain. Cells interact with individual filaments of these networks, exploiting their properties to communicate and orient themselves, while migrating through the extracellular space. Its mechanical properties in turn profoundly influence the fate of cells. The cell-matrix interaction, however, is not well understood due to a lack of experimental techniques to both study the mechanical interplay between cells and their local environment on the single filament length scale, and quantify the contribution of single filaments to the large-scale network properties. To address this need, two novel microscopy techniques are described.

First, quantitative Thermal Noise Imaging (TNI), a three-dimensional scanning probe technique which relies on a trapped nanoparticle as the probe. TNI is capable of imaging soft, optically heterogeneous and porous matter, with submicroscopic spatial resolution in aqueous solution. TNI images of both collagen fibrils in a network and grafted microtubules are shown, and it is demonstrated that structures can be localized with a precision of $\sim 10\,nm$. As a direct consequence of the work done with TNI, Activity Microscopy (aMic), a new way to visualize local network mechanics with single filament resolution is also introduced. Fibril positions in large two-dimensional slices through a collagen network with nanometer precision are localized, and fibrils' transverse thermal fluctuations with megahertz bandwidth along their contour are quantified. The fibrils' thermal fluctuations are then used as an indicator for their tension. The network displays a heterogeneous stress distribution, where "cold" fibrils with small thermal fluctuations surround regions of highly fluctuating "hot" fibrils. Finally, HeLa cells are seeded into the collagen network and the anisotropy in the propagation of their forces is quantified. While the data shown is limited to collagen, aMic will be of significant use when studying the mechanics of other fibrous networks and their application to artificial tissue and organ growth.

Table of Contents

List of Tables

List of Figures

Chapter 1

Introduction

Imaging microscopic structures in living organisms and understanding their processes has fascinated scientist for hundreds of years, with the invention of the microscope thought to date back to the 16^{th} century. The simple light microscope opened up many possibilities for unprecedented insights. Nevertheless it has a fundamental limitation in resolution. The wavelength of the illumination source used, determines the smallest features that can be resolved. This is coined the diffraction limit and was stated more quantitatively by Abbe: two converging spots of light can only be resolved as separate, if they are at least a distance $d = \frac{\lambda}{2\mathrm{NA}}$ apart, where λ is the wavelength of light used, and NA the numerical aperture of the lens. If we use visible green light $\lambda \approx 500\,\mathrm{nm}$ together with a common numerical aperture in current optical systems $\mathrm{NA} \approx 1.4$, the smallest resolvable feature will be $\sim 180\,\mathrm{nm}$. A cell, the fundamental biological unit, is usually micrometer sized, but many interesting processes on the inside happen on a much smaller length scale. There are many biopolymer filaments only several nanometers, or $10s$ of nanometers in diameter, and individual molecules like proteins, exist on an even smaller length scale.

To overcome this fundamental limitation when imaging, the electron microscope (EM) was introduced in the 1930s [1]. Here electrons are used as the source of illumination. They are first focused into a beam and accelerated towards the surface of the object to be imaged, gaining several $10s$ of keV in energy. The De Broglie wavelength for these high energy electrons is then well below a nanometer enabling small scale structures to be resolved more easily. However, to image biological substrates with the use of charged particles requires for the surface to be conductive, or coated by a conducting thin film. In addition, the sample needs to survive very low air pressures in high vacuum ($\sim 10^{-6}\,\text{Torr} \approx 10^{-9}\,\text{atm}$), required to minimize electrons scattering on air molecules while travelling to and from the surface of the substrate. Any biological sample to be imaged by an electron microscope is therefore usually chemically fixed (i.e. killed) and dried (usually cryogenically) to rid it of water. Despite the extensive preparation requirements remarkable structural insights were gained from cryo-EM [2].

Ideally, one would like to observe biological substrates like human cells, as close to physiological conditions as possible, i.e. under atmospheric pressures, in solution, at room or body temperature (37° C). An important step in that direction was the introduction of fluorescence microscopy [3]. Once again employing light, it relies on small molecules called fluorophores, which absorb a very specific wavelength of light, yet emit a longer, Stoke's shifted, wavelength. Fluorophores can be attached to small scale structures of interest like little lightbulbs illuminating their locations or motion. The image formed by the light each fluorophore emits however, is still diffraction limited. To finally overcome this fundamental limitation, recently, diffraction-limit breaking techniques, or super-resolution microscopy techniques have been developed. Many of them produce remarkable images [4], and the concept of super resolved fluorescence microscopy was honored with the Nobel prize in Chemistry in 2014 [5].

Nonetheless much work remains to be done. Super-resolution microscopy still suffers from some limitations and problems, e.g. it still depends on the attachment of fluorophore labels, to the substrates. This can be an issue if the fluorophore is as big or bigger than the molecule of interest, and especially when the goal is to observe dynamics. It also is not yet fast enough to account for thermal position fluctuations of the structures to be imaged. Since much of biological matter, when in its natural setting, will usually be in solution at room temperature or higher, it will either exhibit Brownian motion and move around randomly, or fluctuate and vibrate around a fixed position. This can happen on very fast-time scales and requires equally fast detectors or cameras. In this work we introduce two novel forms of microscopy, which turn the above mentioned limitation into an advantage. Thermal noise of a trapped nanoparticle is in one case used as a scanner for biopolymer filaments; vibrations of those filaments in turn are used as an indicator for the stress they experience when in a network. Thermal Noise Imaging and Activity Microscopy both work under physiological conditions, in solution, for thick samples and without the need for labels. Each gathers information inaccessible to other techniques.

1.1 Research Objectives and Thesis Outline

The need for new types of microscopes arises from the realization that biochemical processes and genetics alone are insufficient to explain many phenomena in biology. Rather we are slowly learning the significance of mechanical forces, and mechanical properties in determining cellular behavior and survival. In fact, it is becoming increasingly clear that a comprehensive characterization of cellular forces and their surrounding mechanical landscape is needed, both *in vitro* and *in vivo* [6, 7]. Only then we can deliberately manipulate their environment to trigger a distinct behavior or prevent certain disease. Further, an improved understanding may allow for the design of better biomimetic materials, like artificial skin.

The remaining sections of Chapter 1 serve to introduce the biological components of interest, on a cellular lengths scale and below, as well as motivate the importance of mechanics in a biological setting. The two microscopy techniques described later in this work require the implementation of a complex, mechanically stable optical setup, together with a high bandwidth, high speed detector and an optical trap. Important theoretical concepts to understand the working principles are introduced in Chapter 2. Finally, Chapter 3 describes Thermal Noise Imaging as a microscopy technique and shows results of its application to collagen fibrils and suspended microtubules. Chapter 4 introduces for the first time Activity Microscopy and its images taken in a collagen network. To conclude, Chapter 5 lays out two possible directions for future work and potential applications.

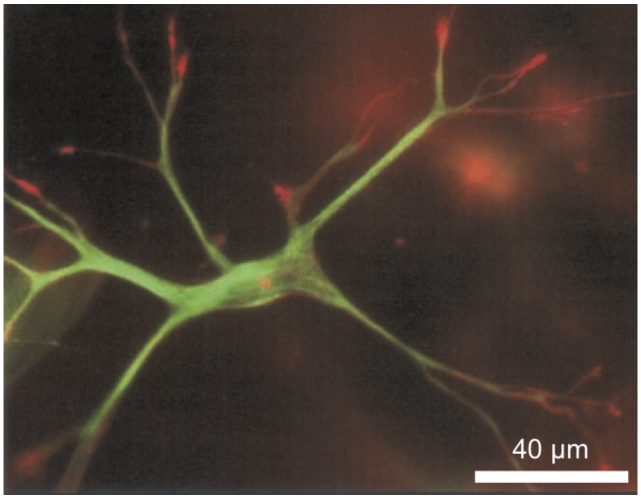

Figure 1.1: 3T3 fibroblast suspended in a three-dimensional collagen matrix. The cells are fluorescently stained for actin (red) and tubulin (green), the protein forming microtubules. To acquire the image, cells were chemically fixed. Adapted with permission from [8].

1.2 The Cell

As the fundamental structural, functional and biological unit, the cell underlies all known living organisms. First described back in 1665 by Robert Hooke [9], cells can fulfill a variety of different functions, and are found in many different morphologies spanning two orders of magnitude in size, from $1 - 100\,\mu$m. [1] Cells can survive as individuals, or form multicellular organisms, e.g. a human has $\approx 10^{13}$ cells [10, 11]. **Figure 1.1** shows as an example a human fibroblast, which is found in the connective tissue, suspended in a

---

[1] Robert Hooke did not actually discover living cells, rather he saw dead plant cells while observing cell walls in cork tissue, but is credited with coining the term 'cell', as his observations reminded him of the cells in a monastery.

three dimensional matrix. Cells that make up the human body require very specific environmental conditions for survival, such as a temperature of 37° C and carefully adjusted pH of the surrounding fluid (usually pH $\sim$ 7.4 [12]). However there exist many other organisms, that can withstand the harsh conditions of habitats such as ice glaciers, high elevation volcanic soil, or even total darkness [13–15]. This highlights the diversity in form and function one finds among living organisms. In addition to their structural functionality, cells are highly active and exist outside of thermodynamic equilibrium [16, 17]. This is achieved, by metabolizing nutrients like glucose, to produce ATP, an energy carrier molecule fueling a myriad of intracellular processes. These include protein synthesis, cellular proliferation, or migration, among many others. Cells can also feel and probe the structural, and mechanical properties of their immediate environment using the information they gather to move or even communicate with each other. A cell is enclosed by a lipid bilayer, called the cellular membrane, which is sufficiently stable to separate the cell from its environment, yet is able to rearrange and flow like a viscous medium [18, 19]. The membrane is selectively permeable and allows passive diffusion of small molecules through the lipid-bilayer, as well as facilitated diffusion through transmembrane channels formed by large protein complexes, for larger molecules and ions [20, 21]. There also exist active transport of matter, which is carried out via transporter proteins or pumps [22]. The inside of the cell, called the cytoplasm contains multiple organelles, functional membrane enclosed structures, like the nucleus, mitochondria, the endoplasmic reticulum, golgi apparatus, lysosomes,

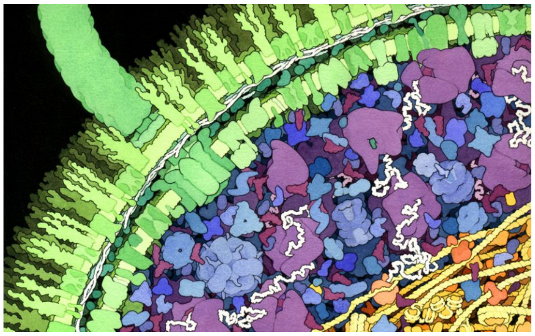

Figure 1.2: Cells are crowded on the inside: an artist's rendition of an E. Coli bacterial cell. The drawing shows on the top left the base of one flagellum, as well as a cross-section of the lipid membrane, together with its many transmembrane channels. On the inside of the cell one can gain an intuition for the crowdedness of the cytoplasm, containing many globular and filamentous proteins and molecules. Illustration by David S. Goodsell, the Scripps Research Institute.

vacuoles, and in plants, chloroplasts. These fulfill a variety of functions, from ATP production to protein synthesis. In addition to organelles, one also finds many filamentous structures and networks, which from the backbone of the cell, or cytoskeleton, providing structural integrity and mechanical resistance. Overall the cytoplasm is a very crowded space; anywhere from $20-30\,\%$ of the volume is filled with various macromolecules [23]. On first glance, this might seem a hindrance for many diffusion-limited processes, like enzymes trying to find their substrate to bind to. However, it also gives rise to a phenomenon termed depletion attraction whereby the crowding can act as a catalyst for interactions between molecules. **Figure 1.2** shows an artist's rendition of the inside of an *E. Coli* bacterial cell and displays well its crowdedness.

Located roughly at the center of the cell and enclosed in its own lipid

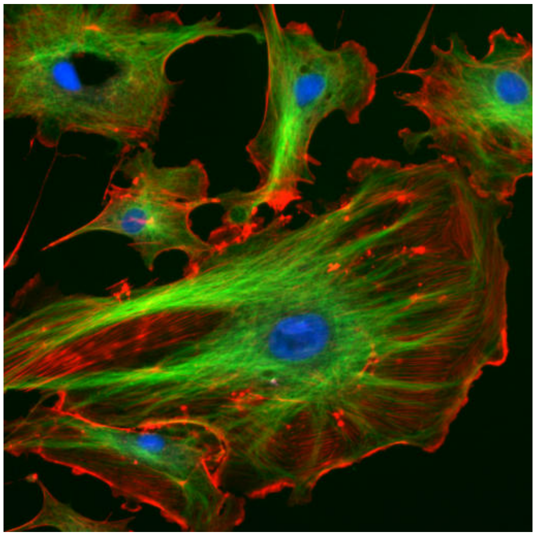

Figure 1.3: Bovine pulmonary artery endothelial cells imaged with fluorescence microscopy. Actin is labelled in red, microtubules in green and the nuclei are stained in blue. Example image from ImageJ available in the public domain [24].

membrane one finds the nucleus, which contains most genetic material in the form of DNA, together with an extensive enzyme machinery to read, repair and duplicate the genetic code. **Figure 1.3** shows two major components of the cytoskeleton, actin (red) and microtubules (green), as well as the nucleus (blue) made visible with the use of stunning fluorescent labels.

In general, we can differentiate between two distinctly different groups of cells: prokaryotic and eukaryotic cells (**Fig. 1.4**) [22]. The type of cell we alluded to above belongs to the latter group of Eukaryotes, which encompass all plants, fungi, animal, and human cells. They are generally sized on the order of $10 - 100\,\mu$m. Eukaryotes contain membrane bound organelles, such as

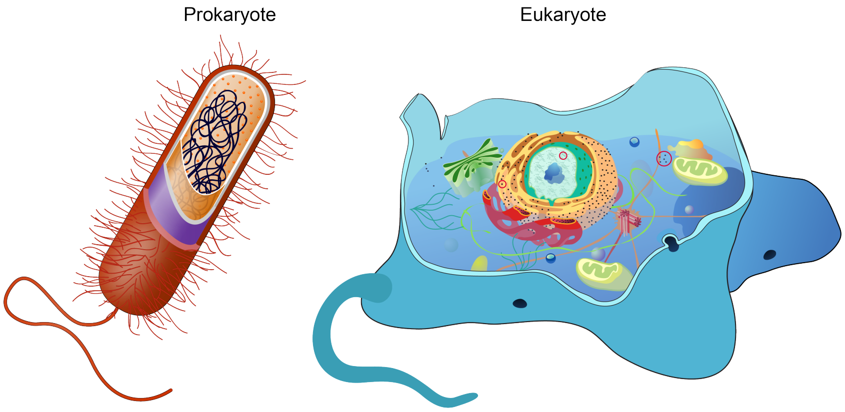

Figure 1.4: The difference between prokaryotic and eukaryotic cells. The image shows schematic drawings of a typical prokaryotic cell on the left and a common eukaryotic cell on the right. Characteristic features include a long flagellum on the bottom, which is used for forward propelling motion, as well as multiple pili (small hair like structures) lining the outer membrane (orange). Prokaryots typically have an additional cell wall (purple) and another inner membrane (yellow). In the cytoplasm, the DNA (black strings) is freely moving around. It has only one enclosing envelope (cell membrane in blue). The cytoplasm contains many filamentous proteins, and membrane enclosed structures, most prominently the spherically appearing nucleus which contains all genetic material. Adapted and modified from [25, 26].

mitochondria, and a nucleus, which separates and protects all genetic material in the form of DNA as described above. Furthermore, these strands of DNA are arranged into more complicated three-dimensional structures facilitating tight packing in the nucleus, necessitated by a larger genetic code [27].

The former group includes all bacteria and archaea, which were the first forms of life on earth. Both are single celled organisms, sized usually from $1 - 10\,\mu$m, and are mainly distinguished by their lack of a nucleus and other membrane bound organelles in the cytoplasm. As such, the DNA is found distributed within the cell body. Bacteria especially, while functioning as individual entities, will arrange in complex colonial and at times three-dimensional structures such as biofilms, which may provide an evolutionary advantage via increased resistance to external stressors by increasing mechanical stability [28]. Bacteria also distinguish themselves by the existence of extrusions from their membrane, either flagella or pili, which enable them to swim in a liquid or crawl on surfaces [29]. Some strains produce what is known as the lubrication layer, a thick viscous fluid promoting bacterial swarming [30]. Prokaryotes likely served an integral part in the evolution of Eukaryotes, which may have developed membrane bound organelles through the ingestion of bacterial cells [22]. In the following we will focus on eukaryotic cells, and list some of their important properties and components.

1.3 Biopolymer Filaments and their Networks

1.3.1 The Cytoskeleton

The cytoskeleton is found on the inside of cells and is composed of a system of interlinking biopolymer filaments and their networks. It fulfills many crucial functions for the cell: It provides mechanical stability and integrity to the cell; it organizes internal structures inside the cytoplasm; it serves as tracts for intracellular transport by motor proteins; it enables the cell to interact mechanically with its environment, linking to the extracellular matrix (section 1.3.2); and finally allows the cells to change shape and thereby crawl and migrate. There are three major globular protein families, that comprise the cytoskeleton in their filamentous form as microtubules, actin and intermediate filaments. They enable all of the above via their ability to rapidly polymerize into filaments, crosslink into networks and fall apart again into individual proteins depending on the cell's need. In the following we will describe important details about all three.

1.3.1.1 Microtubules

Microtubules are thin, hollow tubes with an outer diameter of about 25 nm, and which can grow to $10s$ of μm in length. They have a higher bending stiffness than many other biopolymer filaments, with a persistence length in the millimeter range. The persistence length is a quantity that roughly describes the length scale over which a filament can be considered straight in its conformation (for a more detailed description see Chapter 1.4.2.1). Microtubules are formed by $9-17$ protofilaments (most probable are 13 protofilaments), which first align in parallel to form a sheet and then successively roll into a hollow cylinder (**Fig. 1.5**) [31]. A protofilament polymerizes out of individual monomers, that are themselves dimers consisting of α- and β-tubulin. After a nucleation event tubulin dimers can attach to each other and grow into filaments. This process is strongly dependent on the overall tubulin concentration.

The tubulin dimer has two nucleotide binding sites at each of which a guanosine triphosphate (GTP) nucleotide, an energy carrier molecule akin to ATP, is bound; one in the middle, and one at the end of β-tubulin. After a

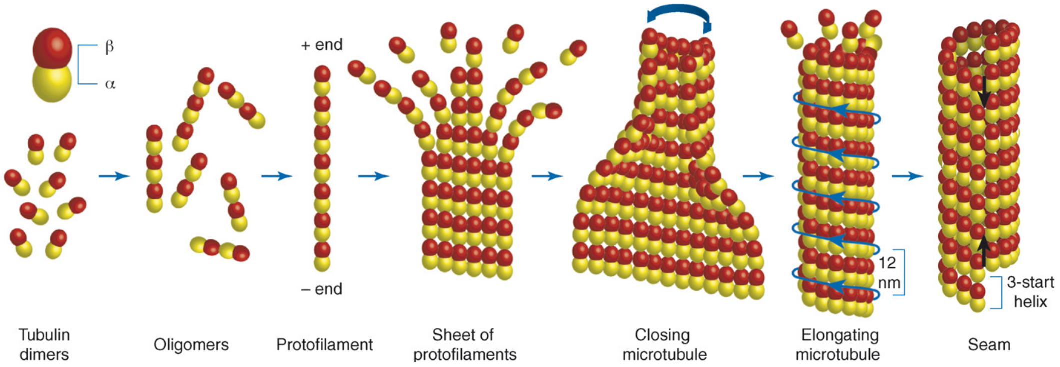

Figure 1.5: The process of microtubule polymerization. Tubulin dimers assemble head-to-tail to form protofilaments, which in turn align laterally into a sheet. After a typical number of protofilaments (13) have assembled the sheet rolls up into a hollow tube forming the microtubule. The last two panels show, that it does so asymmetrically, leading to a characteristic pitch. Adapted with permission from [31].

tubulin-dimer attaches to the growing filament, the outer GTP, bound to β-tubulin will hydrolyze to guanosine diphosphate (GDP) releasing a phosphate, which mechanically destabilizes the filament. Depending on which process is faster, growth via polymerization or hydrolization, the microtubule can start to depolymerize and fall apart again. The latter is known as catastrophe. If however, it grows fast enough to outpace hydrolization, there will always be a cap of GTP bound dimers which 'rescue' the microtubule. Termed dynamic instability, this interplay of growth and shrinkage is a stochastic process, and plays an important role in many cellular processes. Microtubules are polar filaments with a (+) end (β-tubulin) and (−) end (α-tubulin). Both ends can grow, but the (+) end grows faster. Many drugs have been developed targeting microtubule dynamics, e.g. Taxol which acts to stabilize by protecting the microtubule from disassembly and thereby suppressing dynamics. Taxol is a cancer therapeutic agent, but is also used in laboratory settings to enable the detailed study of microtubules [32]. Within the cell, microtubules are organized and originate from the Microtubule Organizing Centers (MTOCs) and are involved in many crucial functions. For instance, one often finds microtubule arrays in elongated structures such as hair cells or long axons providing the tensile strength and resistance to bending. There exist also many microtubule associated proteins, the most notable ones being motor proteins like the kinesin family. Motor proteins use microtubule filaments spanning the cell as tracks to walk on and thereby facilitating intracellular transport.

1.3.1.2 Actin

Actin is another crucial filamentous protein that is part of the cytoskeleton, and is found in all eukaryotic cells. Actin is the thinnest and most flexible in the group of cytoskeletal filaments. Its microfilaments have a diameter of only 7 nm and its persistence length is in the micrometer range ($l_p = 17 \pm 2\,\mu$m) [33]. Actin is mainly found lining the periphery of the cell's interior, the cell cortex, providing stability to the lipid membrane. It acts as the main driver for cell motility by extending and contracting the membrane via rapid polymerization into filaments, crosslinking into networks, and then depolymerization. A good example are muscles cells, which are able to contract and thereby generate significant force with the help of actin.

One generally distinguishes between G-actin, the globular protein monomer,

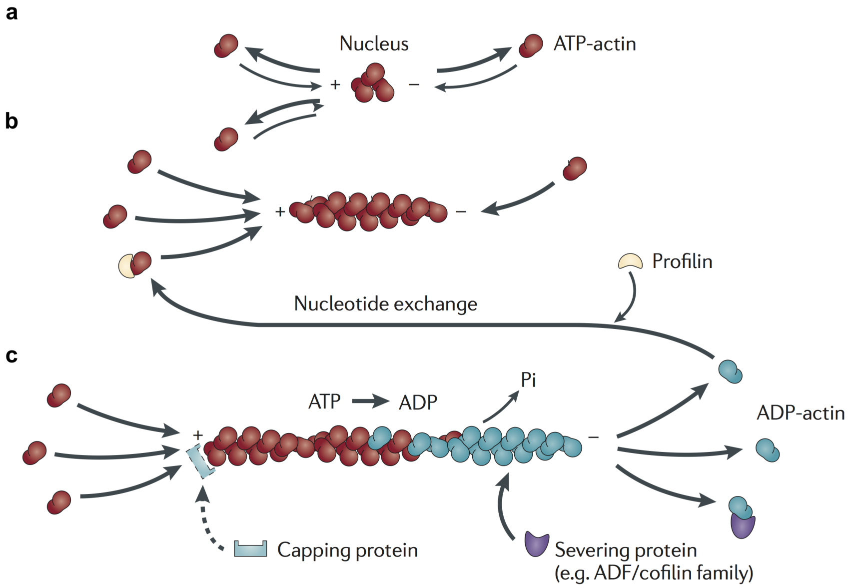

Figure 1.6: Actin polymerization. Actin monomers spontaneously bind together in a first nucleation step (**a**), and grow into small filaments (**b**). The (+) end grows faster than the (−) end at first, which is indicated by the arrows. After the filament has reached a certain length, the bound nucleotides ATP hydrolyze to ADP (green part of the filament) thereby destabilizing the filament and causing its depolymerization on the (−) end (**c**), while the (+) end continues to grow. The overall dynamics are regulated via actin binding proteins, three examples are shown: capping proteins stabilize and arrest growth or shrinkage at one end, severing proteins are able to cut a filament and profilin bind to free monomers promoting polymerization. Adapted with permission from [34].

and F-actin, the filamentous, polymerized actin microfilaments made up out of two strands wrapped around each other in a right-handed helix. G-actin itself has a diameter of $4-7\,\mathrm{nm}$ and one nucleotide binding site for adenosine triphosphate (ATP), the prominent energy carrier in the cell. Provided that the concentration of monomers in solution exceeds a certain critical value C^*,

	ATP-actin		ADP-actin	
	Barbed (+)	Pointed (−)	Barbed (+)	Pointed (−)
$k_{\mathrm{on}}(\mu\mathrm{M}^{-1}s^{-1})$	11.6	1.3	3.8	0.16
$k_{\mathrm{off}}(s^{-1})$	1.4	0.8	7.2	0.27

Table 1.1: Actin polymerization reaction rate constants. The table shows the rate constants for actin polymerization and depolymerization for both ends. Note that k_{on} is dependent on the monomer concentration in solution, where k_{off} is not. Adapted with permission from [35].

actin will first undergo nucleation events (**Fig. 1.6 a**), followed by a rapid growth phase (**Fig. 1.6 b**). Like microtubules, filamentous actin is a polar filament with a (+) end (also called the barbed end), and a (−) end (referred to as pointed). Both ends have different rate constants describing growth and shrinkage, where the former tends to be faster growing. The on-rate k_{on}, which describes the addition of G-actin to an existing filament is concentration dependent, while the off-rate k_{off} is independent of monomer concentration, yet differing for both ends (see **Table 1.1**) [35].

The critical concentration above which the filament will grow, is also different for either end, $C^*_+ = 0.12\,\mu\mathrm{M}$, and $C^*_- = 0.60\,\mu\mathrm{M}$ (ignoring rate constant values for ADP monomers). This leads to a very interesting phenomenon, characteristic to actin called treadmilling. Imagine three scenarios as displayed in the different shaded regions of **Figure 1.7**: if the monomer concentration in solution $C < C^*_+$, an existing filament will predominantly lose monomers on both ends, leading to net shrinkage. If $C > C^*_-$, both ends will grow and elongate the filament. If however $C^*_+ < C < C^*_-$, the filament will grow at the (+) end and shrink at the (−) end, which leads to an apparent for-

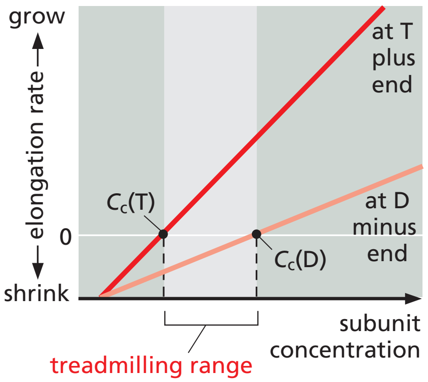

Figure 1.7: Actin treadmilling. A simplified graphic shows the overall reaction rate for the (+) and (−) end and their different critical concentrations. The light grey shaded area marks the bounds on solution monomer concentration between which an actin filament will exhibit treadmilling. Adapted with permission from [36].

ward motion of the filament. Within treadmilling concentration range, there is also the special case of a steady state, where the filament length is constant, which is $\sim 0.17\,\mu$M for our example.

Actin polymerization and crosslinking is used by the cell not only to stabilize the membrane, but also to apply forces to it. This can change the morphology of the cell and enable it to crawl across a surface and interact with its environment in numerous ways. The energy associated with force generation comes from a release of free energy ($\Delta G < 0$), which occurs when a monomer attaches to an existing filament, and the following hydrolyzing event of the bound ATP nucleotide. In fact, there are three different actin species when taking the nucleotide and its hydrolization state into account. First the ATP bound G-actin binds to an existing filament. After a short delay

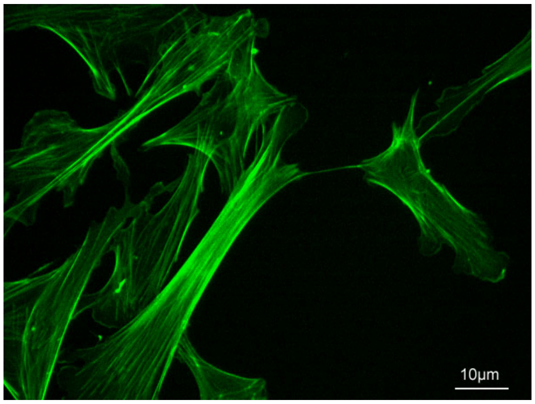

Figure 1.8: Actin stress fibers. Fluorescently stained embryonic mouse fibroblast show thick actin fiber bundles aligned in parallel and spanning the interior of the cells. Adapted from [39].

ATP is hydrolyzed, but the thereby released phosphate group P_i will remain bound to the protein for another while before being finally released. As the rates for hydrolyzing and phosphate release are slower than polymerization, a growing filament will effectively have an ADP + P_i and ADP-actin cap (**Fig. 1.6 c**). This is thought to regulate the binding of several actin associated proteins, which facilitate cross-linking, or severing filaments to give just two examples [37]. Higher order structures of actin beside microfilaments described above, exist as well. Microfilaments can bundle into thicker stress fibers, found for instance in fibroblast cells (**Fig. 1.8**) [38] or form sarcomeres, an important unit of muscle cells, all with the help of actin binding proteins like the motor protein family myosin.

1.3.1.3 Intermediate Filaments

While the aforementioned polymers actin and microtubules are well conserved across many species and time, there is a third protein family, which is also part of the cytoskeleton, but is more specific to certain types of tissues and are also more diverse. The so-called intermediate filaments are not found in all eukaryotic cells, but are predominately present when the cell is subject to significant mechanical stress [40]. Intermediate filaments are non-polar and comparatively flexible. Their persistence length is $l_p < 1\,\mu$m. Unlike actin and microtubules, they do not have any nucleotide binding sites. Their monomers usually bind to each other via hydrophobic forces, although not much detail is known about their assembly processes. There exist three major subgroups of intermediate filaments which deserve mention here. The Keratin family of proteins can form strong networks utilizing disulfide bonds, which can outlast the lifetime of their cell. This can be observed in the outer layer of the skin, hair and nails. Neurofilaments are found alongside microtubules, at time outnumbering them, in neural axons. And finally, vimentin plays a role in muscle fibers. Yet another class of cytoskeletal proteins are septins, which bind the nucleotide GTP and can form cages and ring-like structures. These have been observed to aid compartmentalization during cell division and help to organize actin. Septins themselves are rather static when compared to the bustling activity of actin or microtubules.

1.3.2 The Extracellular Matrix

Outside of cells in all tissues and organs one finds a complex network of multiple different proteins, as well as polysaccharides, together forming the extracellular matrix (ECM). The ECM is mainly passive, with its primary role being to provide mechanical stability and integrity to different types of tissues [41]. For this reason, it has a variety of interesting mechanical properties, which will be covered in more detail later (see section 1.4). The ECM comes in many different forms and makes up very stiff and hard substances like, bone or tendons, but can also be soft and elastic as in epithelial connective tissues. Its components are largely secreted by fibroblast cells and subsequently self-assemble into networks and gels [41]. Fibroblasts also interact and reshape the ECM, and are in turn effected by its architecture and mechanical properties. **Figure 1.9** shows an electron microscopy image of corneal fibroblasts suspended in their ECM.

There are three main groups of macromolecules that make up the ECM: (i) Polysaccharides which can covalently bind to proteins; (ii) Fibrous proteins, mainly from the collagen family; and (iii) Glycoproteins. The latter form a gel-like base structure in which filaments such as collagen are embedded. Collagen and other filamentous proteins mainly resist stretching forces through high tensile strength, whereas glycoproteins counter compression. Collagen networks are for instance a main component of the heart and heart valves, providing the necessary stability and elasticity [43]. Degradation and failure of the heart and its valves is closely related to the breakdown of the underlying

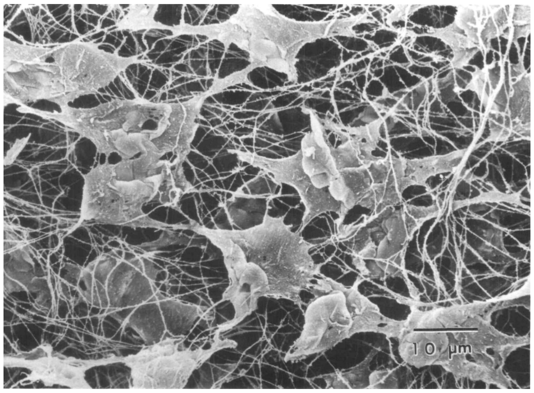

Figure 1.9: Cells suspended in the extracellular matrix. The picture shows a scanning electron microscopy image of corneal fibroblasts suspended in the ECM, thin filaments visible are collagen fibrils. Adapted with permission from [42].

collagen network either with age, of disease [44]. One also finds a myriad of matrix-associated proteins with a variety of functions, as well as cross-linking enzymes. All together there are more than 300 different proteins found in the ECM of mammals. For the scope of this work we will focus mainly on collagen and its networks as arguably the most important member of the ECM.

1.3.2.1 Collagen

Collagen is the major component of the ECM and also the most abundant protein in mammals, making up about 25 % of the total protein mass. It is not surprising that is has been of great interest to researchers for many years [45–47]. There are 28 different types of collagens in humans [48], but type I makes up about 90 %, and is also the most studied among them. Collagen displays many different levels of hierarchy over multiple orders of magnitude in

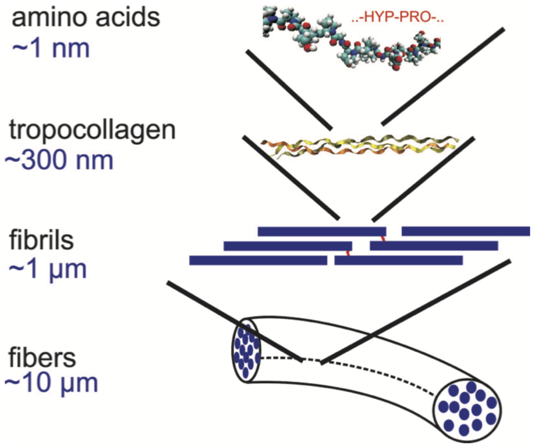

Figure 1.10: Levels of hierarchy of collagen. Collagen exists on many different length scales, from the collagen molecule only $\sim 1.5\,\text{nm}$ in diameter, to the thick collagen fibril bundles underlying tendons. Adapted from [49]. Copyright 2006 National Academy of Sciences.

size (**Fig. 1.10**). At its smallest lies the collagen molecule, or tropocollagen, a triple helix out of three polypeptide strands about 300 nm long and 1.5 nm in diameter. The α-chains are rich in amino acids proline and glycine, to be found at almost every third residue along the chain.

Collagen is secreted by fibroblasts in the form of the tropocollagen molecule. Any higher order structure following secretion forms via self-assembly under favorable conditions. Collagen molecules can arrange and grow into fibrils, which range from $10-300\,\text{nm}$ in diameter, yet can be $100s$ of μm long [46] and entangled into networks. In fact, when imaging a network of collagen fibrils, no fibril ends are usually observed. Many fibrils can bundle together to form even thicker fibers, as found in tendons, and they can cross-link via enzymes, like lysyl-oxidase. This fibrillogenesis is an entropy driven process

(**Fig. 1.11**) that depends on a variety of factors such as temperature, pH, and ionic strength of the solution. Tropocollagens bind together mainly through hydrophobic and electrostatic interactions as is shown in **Figure 1.11**.

At low temperatures, water molecules tend to arrange in organized sheets around the non-polar regions of the protein [51], due to increased hydrogen bonding between the neighboring molecules. When the temperature rises however, these sheets of water "melt" away, which increases the overall entropy of the system, and hydrophobic forces start binding tropocollagens together. At this point, electrostatic forces at the polar regions become significant as well. The filamentous shape with circular cross-section, assumed by the final structure, minimizes the ratio of surface area to volume. Tropocollagens underlying the fibrils also tend to arrange and stagger in a very ordered and patterned fashion, such that there will be an area of less dense packing, or "gap" with a periodicity of $D = 67\,\text{nm}$. This is most strikingly visualized using atomic force microscopy (AFM), where one will observe the varying topography as dark and light areas repeating along the fibril (**Fig. 1.12**).

For *in vitro* studies of collagen, it is usually extracted out of animal tissues (commonly bovine or rat) and dissolved into cold neutral salt solutions, or dilute acids like acetic acid [54]. This process is reversible: collagen starts self-assembling into an entangled network of fibrils again as described above, when the temperature is raised, and the pH neutralized [45]. **Figure 1.13** shows two images of such a network using scanning electron microscopy (SEM). Networks are often studied in isolation for their interesting mechan-

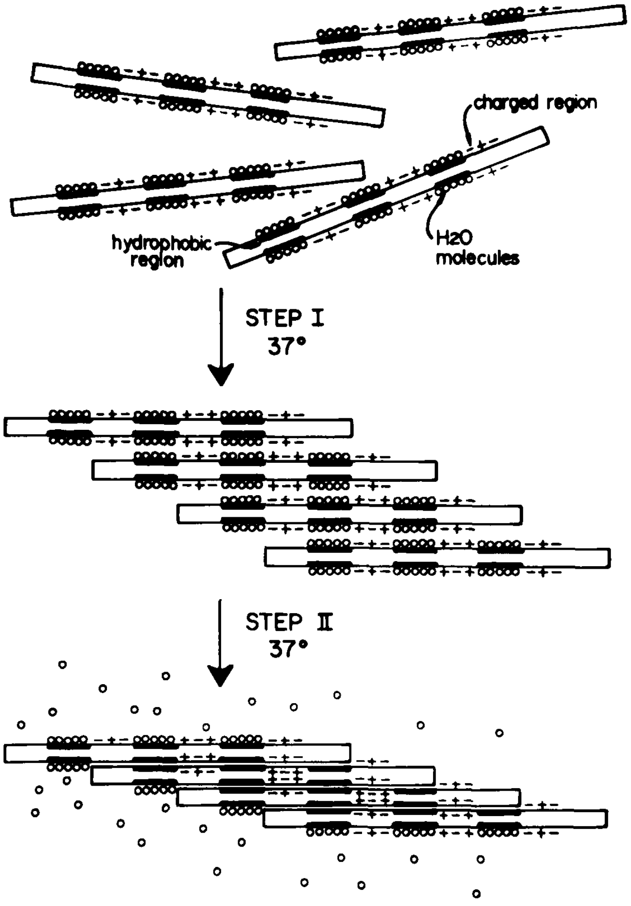

Figure 1.11: Mechanism of collagen fibril polymerization. Top shows the start of fibril formation by collagen molecules binding together via electrostatic attraction. Collagen molecules have both polar and non-polar regions. At low temperatures the non-polar parts are covered with hydrogen bound water sheets, which "melt" away with rising temperature. This increases the overall entropy therefore making it more favorable. The non-polar regions then contribute to fibril formation via hydrophobic binding. Adapted with permission from [50].

ical properties, but are also commonly used as scaffolds for 3D cell culture or to aid cell surface attachment. They might also be combined with other

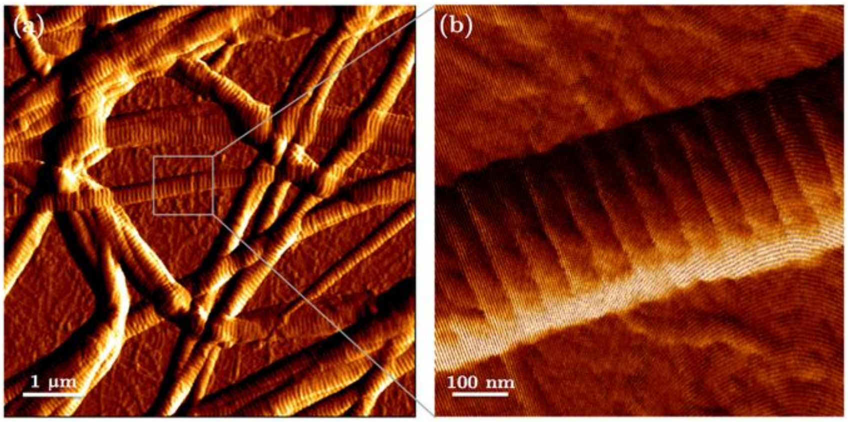

Figure 1.12: Atomic force microscopy image of collagen fibrils. (**a**) Several fibrils attached to a surface are imaged. **b** shows a close up of **a**. The fibril's surface very clearly shows the D-banding with a periodicity of 67 nm characteristic to collagen type I (bright and dark stripes). Adapted from [52].

biopolymer networks, to serve as scaffolds for 3D cell culture, or the formation of organoids which are miniature organ models [55, 56]. Matrigel is a widely commercially available scaffold employing such a combination.

1.4 Mechanics and Biology

1.4.1 Mechanics and Cells

Over the past 100 years it has become clear that biochemistry and genetics alone only insufficiently explain many cellular phenomena [57]. Rather, we are learning that mechanical properties of the ECM as well as of the cell itself, play a major role. Cells secret ECM proteins, remodel and reshape the ECM's architecture, and are in turn strongly affected by its mechanical properties in a constant back and forth between the ECM and cells [6]. The process

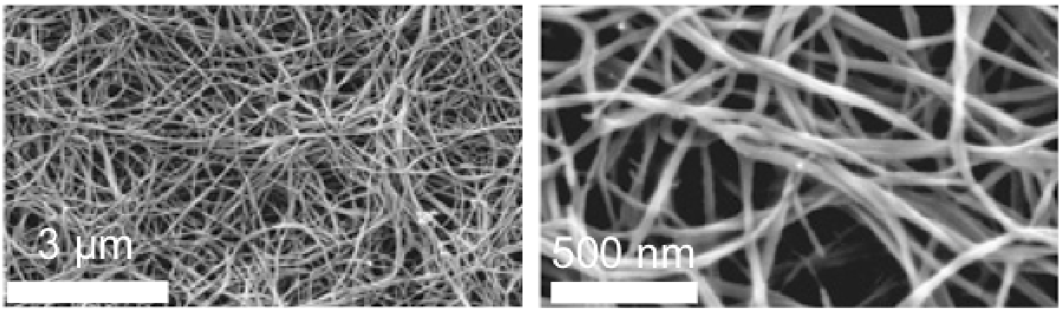

Figure 1.13: Scanning electron microscopy image of a collagen network. The network was polymerized at 37° C, then chemically fixed and dried, and finally imaged at two different magnifications. Adapted with permission from [53].

by which cells are influenced by their surroundings is termed mechanotransduction, which describes the action of translating a mechanical signal into a biological response. This occurs via a coupling chain: the ECM connects to transmembrane proteins called integrins. After contact, many transmembrane proteins including integrins, can cluster and form a focal adhesion complex, which in turn connects to the actin cortex as part of the cytoskeleton. The elastic response of the ECM to a cellular pulling force can for instance lead to conformational changes in the integrin proteins of the focal adhesion complex. This in turn, can trigger signaling cascades further downstream, which may propagate all the way to the nucleus. Along this path the signal may also lead to cytoskeletal or protein alterations, or even change gene expression via epigenetics [58].

Differentiation

Cells in our bodies only have a limited life time, while constantly dividing and reproducing. That cycle only occurs a finite amount of times before it stops. Programmed cell death, so-called apoptosis is crucial in healthy tissue. In cases where it is disrupted, and cells divide uncontrollably, cancerous tissue will form. In order to replace dead cells, the body harbors stem cells; there are different types: adult stem cells which exist in many organs of an adult body can only differentiate into the organ's specific cell types. Embryonic stems cells however are pluripotent and capable of differentiating into any cell type. As it turns out, this differentiation process seems to be largely determined by the elastic properties of the surrounding matrix: Engler *et al.* [59] cultured pluripotent mesenchymal stem cells in two-dimensional cell culture, on substrates with elasticities spanning three orders of magnitude (Young's modulus $E = 0.1 - 40\,\mathrm{kPa}$). They found that the cells differentiated into neurons when adhered to a soft substrate mimicking the brain, but become osteoblasts (bone cells) when cultured on a stiff matrix. It largely appears that the fate of a cell is determined by the mechanical properties of the ECM surrounding it.

Morphology

The strong influence of mechanics on the cellular life is highlighted by another striking example when studying cell morphology: how much cell shape is influenced by the mechanical environment the cell is growing in. Take fibroblasts for instance. As an important part of connective tissues, they assume very different shapes when cultured on a stiff substrate like glass as compared to when cultured on a much softer layer of collagen [60]. Even more striking, in the first case fibroblasts will form so-called stress fibers (see **Fig. 1.8**), which are thick actin myosin bundles in the cytoskeleton, spanning the entirety of the cell and allowing it to apply pulling forces to its environment [38].

The above are only two examples of the overall importance of mechanics in the life of a cell. Other cases include cellular communication [61] and cellular migration [62]. To migrate, cells grab on to extracellular matrix filaments and produce pulling forces. Eventual translation of these pulling forces into translocation depends on the local mechanics of the network, e.g. how well the cell is able to squeeze through the network's pores. Cells need to navigate through these networks, in wound healing, development, or differentiation. However, migration also plays a crucial role in the case of cancer. There, tumor cells will actively remodel and stiffen the ECM by realigning otherwise curly collagen filaments. This aids metastasis, as straightened collagen fibers can act like highways for migrating cells [63].

1.4.2 Single Filament Mechanics

The above sections have introduced and described the ECM, its underlying biopolymer networks, and its different constitutive proteins. Over the past few decades many research groups have studied these biopolymers and their mechanics, mainly *in vitro*. In the following we will introduce some use-

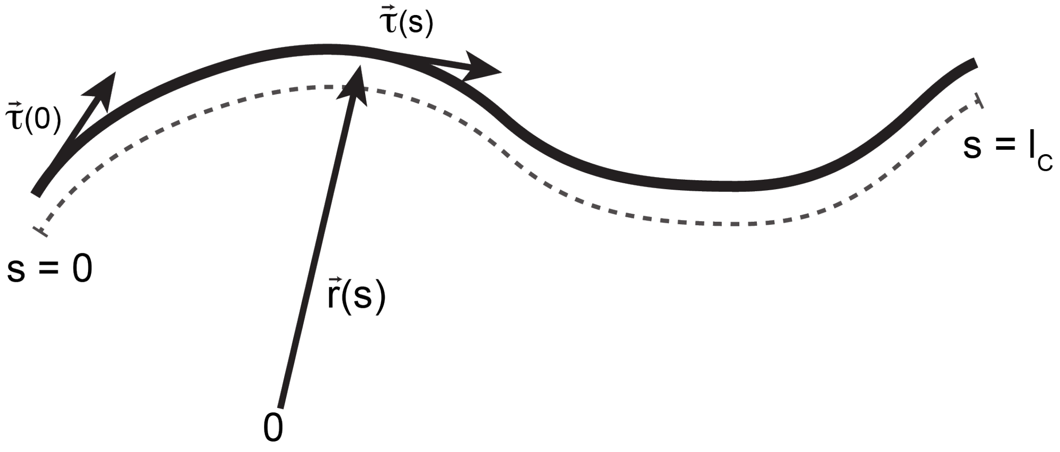

Figure 1.14: Persistence length of a semiflexible biopolymer filament. The filament (thick black line) undergoes random fluctuations from the straight configuration, but is mostly straight. Coordinate s describes the position along the contour (dashed line) from $s = 0$ to the total contour length $s = l_c$. Two tangent vectors $\vec{\tau}$ are indicated, as well as the position vector $\vec{r}$.

ful concepts and results. It is helpful to begin with a description of individual biopolymer filaments.

1.4.2.1 Persistence Length

Individual biopolymer filaments are often described as semiflexible, a qualitative description, that has a two-fold meaning. Semiflexible filaments are mostly straight and rod like, yet will still experience significant deviations from the straight configuration, due to random thermal forces originating from the surrounding medium (see Chapter 2.1.3.1). The persistence length quantifies this behavior and is a useful descriptor of a filament's stiffness. It defines the length scale over which a filament will be mostly straight. More rigorously it describes the length over which a correlation of two tangent vectors along the filament will decay. **Figure 1.14** shows a filament of contour length l_c. The correlation between two tangent vectors will fall off exponentially as:

$$< \vec{\tau}(0)\,\vec{\tau}(s) >= \exp[-s/l_p], \tag{1.1}$$

where s is the coordinate along the filament, and l_p the persistence length. l_p can also be related to the bending stiffness, the so-called flexural rigidity κ, and the thermal energy of the surrounding medium [64]:

$$l_p = \frac{\kappa}{k_B T}, \tag{1.2}$$

where k_B is the Boltzmann constant and T the temperature. For simple geometries κ can in turn be described by $\kappa = EI$, where E is the Young's modulus and I the second moment of the area. The Young's modulus describes a material's resistance to tensile stress, as $E = \frac{\text{stress}}{\text{strain}} = \frac{\sigma}{\epsilon}$; I depends strongly on the given geometry, e.g. is $I = \frac{\pi}{4} r^4$ for a filled cylinder bend away from its long axis [65]. In most cases, a semiflexible polymer will have a persistence length roughly on the same order as its contour length $l_p \approx l_c$. Two examples include:

$$l_{p,\text{F-actin}} = 17\,\mu\text{m}, \tag{1.3}$$

$$l_{p,\text{microtubules}} = 1 - 5\,\text{mm}. \tag{1.4}$$

However, one can describe two other regimes in which either $l_p \ll l_c$, or $l_p \gg l_c$. In the former case the polymer is described as flexible. A good example here is DNA, which if left unperturbed in a thermal bath (see Chapter 2.1.3.1), will coil up into random entangled configurations. On the other end of the spectrum, the polymer will be almost entirely straight with a very high bending stiffness. The persistence length of collagen places it closer to the latter category with $l_{p,\text{collagen}} \approx 1\,\text{m}$. [2]

1.4.2.2 The Wormlike Chain Model

When describing the behavior of semiflexible biopolymers the Wormlike Chain Model (WLC) as first described by Kratky and Porod in 1949 [67] is a useful tool (see also Broedersz *et al.* [68]). It incorporates the fact that over a finite length scale, the filament in question is mostly straight, and can be assigned a bending stiffness κ. The WLC model therefore assumes for the filament to be a continuous flexible rod of length l_c, variable s describes the positon along the contour (**Fig. 1.14**). A unit tangent vector at s along the filament is defined as:

$$\hat{t} \equiv \frac{\partial \vec{r}(s)}{\partial s}, \tag{1.5}$$

and the energy associated with bending the rod is:

$$H_{\text{bend}} = \frac{\kappa}{2} \int_0^{l_c} \left| \frac{\partial \vec{t}}{\partial s} \right|^2 ds. \tag{1.6}$$

---

[2] Assuming a fibril radius of $r = 80\,nm$ and Youngs modulus between $E = 0.07\,\text{GPa} - 0.17\,\text{GPa}$ [66], one arrives at a persistence length of: $l_p = \kappa/k_B T = (\pi/4r^4)/k_B T = 0.54\,\text{m} - 1.32\,\text{m}$.

End-to-end Distribution

When the tangent vectors are integrated over the full contour, it gives the so-called end-to-end distance $\vec{R}$, which is the vector connecting both ends of the filament, $s = 0$ and $s = l_p$:

$$\vec{R} = \int_0^{l_c} \hat{t}(s) ds. \tag{1.7}$$

This expression alone is not very useful; however with the exploitation of the correlative relationship between two tangent vectors in **equation 1.1** we can derive the mean square end-to-end distance:

$$\begin{aligned} \left\langle R^2 \right\rangle &= \left\langle \vec{R}\,\vec{R} \right\rangle = \left\langle \int_0^{l_c} \hat{t}(s) ds \int_0^{l_c} \hat{t}(s') ds' \right\rangle \\ &= \int_0^{l_c} ds \int_0^{l_c} \left\langle \hat{t}(s)\hat{t}(s') \right\rangle ds' = \int_0^{l_c} ds \int_0^{l_c} \exp\left[\frac{-|s - s'|}{l_p}\right] ds', \qquad (1.8) \\ \left\langle R^2 \right\rangle &= 2 l_p l_c \left[1 - \frac{l_p}{l_c}\left(1 - \exp\left[\frac{-l_c}{l_p}\right]\right)\right]. \end{aligned}$$

The above expression contains the persistence length l_p which, as we saw above is related to the thermal energy $k_B T$ in **equation 1.2**. Therefore, the end-to-end distance when measured for a given semiflexible polymer follows a probability distribution as seen in **Figure 1.15**, showing an example of the end-to-end distribution for a 75 nm long strand of DNA. This particular contour length only represents roughly $2 \times l_p$ for DNA, and can therefore still be thought of as close to straight. The distribution changes significantly for longer samples, which will be more coiled up. An analytical description can be derived as well and is described by Wilhem *et al.* [69]. The distributions are non-gaussian in shape mainly due to complications arising from self-avoidance of the polymer, i.e. even in a coiled up configuration it cannot intersect with itself because of steric hindrance.

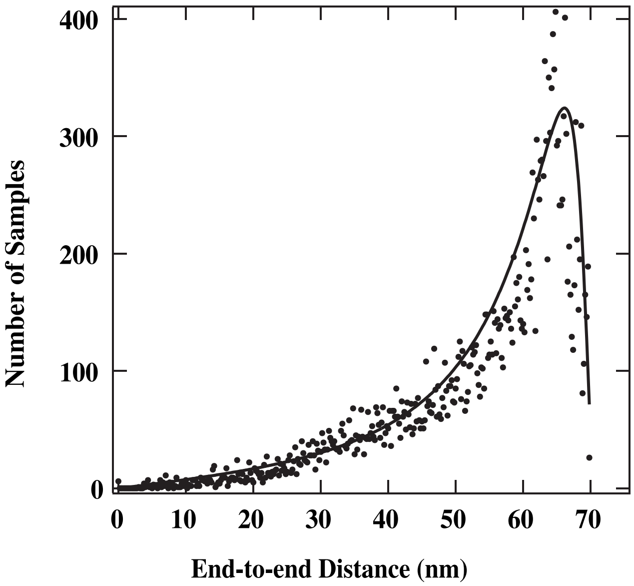

Figure 1.15: End-to-end distribution of a semiflexible biopolymer filament. The particular histogram shows the distribution of the end-to-end distance for a 75 nm long DNA string. Adapted with permission from [70].

Force-Extension

Let us now imagine a single semiflexible biopolymer, attached on one end to a fixed support and free to fluctuate on the other end, immersed in a thermal bath. The filament will undergo thermal fluctuations and its end-to-end distance will be smaller than its contour length. Let us further suppose we apply a tension force τ in the longitudinal direction. We will then register two different force-response regimes. First, with increasing τ the magnitude of the thermal fluctuations drops and is suppressed, the filament effectively acts as an entropic spring. With further increasing force however, we will begin to stretch the bonds attaching individual monomers to each other. This is called the enthalpic response and will give a much stronger resistance. While linear at first, the response becomes non-linear already in the entropic regime. An example for a force-response determined experimentally by applying piconewton forces to DNA strands by Wang *et al.* [71] can be seen in **Figure 1.16**.

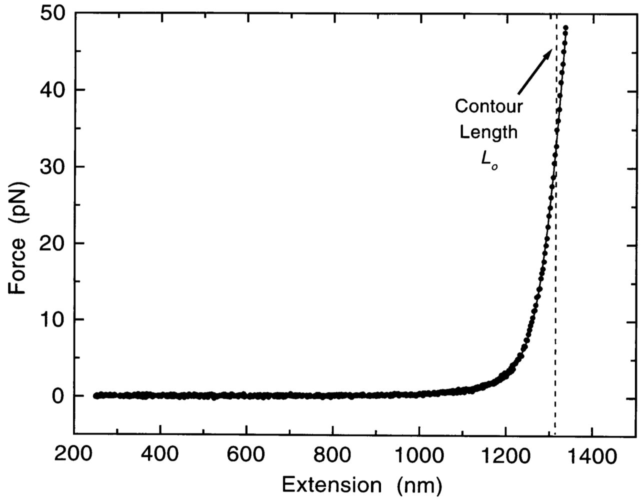

Figure 1.16: Force-extension relationship for DNA string. Piconewton forces were applied via an optical trap to a string of DNA, ~ 1300 nm long and the extension (end-to-end distance) was measured. The contour length is marked with a vertical dashed line. One can see that at extensions well below the contour length, significant forces are needed to further extension the filament. This is the entropic force response dominated by thermal forces. Once exceeding the contour length, the stretching over intermolecular bonds dominates the response. Adapted and modified with permission from [71].

Thermal Undulations as Function of Applied Tension

An analytical description of how the amplitude of thermal fluctuations depends on an applied tension force was for example presented by MacKintosh *et al.* [72] and is briefly restated below. **Figure 1.17** shows a filament supported on one end, but free to fluctuate at the other, both in the force free state and with a tension force τ applied. Let us call the coordinate perpendicular to the filament's support x, and the function describing the filament's deviation from a straight line dependent on x and t, $u(x,t)$, which represented as its Fourier

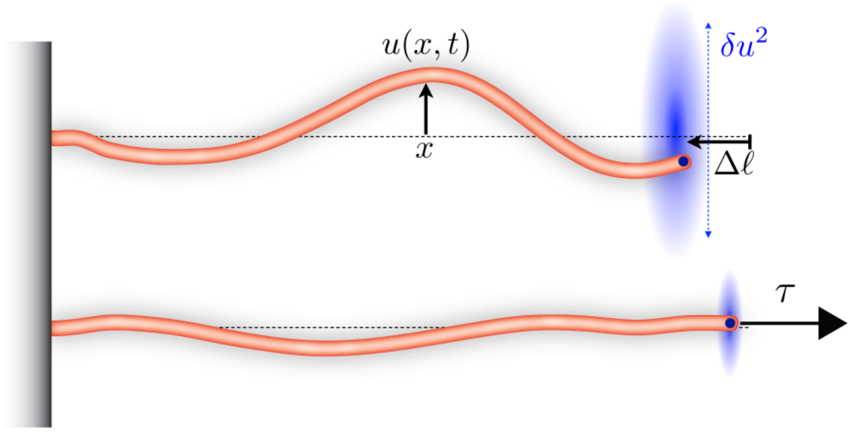

Figure 1.17: Transverse filament fluctuations. The figure shows a filament attached on one end to a support, but free to fluctuate on the other. In the zero forces state (top) the filament undergoes significant transverse fluctuation which can be described with amplitude $u(x,t)$ where x is the coordinate along the horizontal direction, and t is time. The deviation from the straight configuration causes the filament to contract on average from its contour length by $\langle \Delta l \rangle$. The mean-squared fluctuation around this average is δu^2. When a longitudinal tension force τ is applied (bottom), transverse fluctuation will be suppressed and the filament elongated. Adapted with permission from [68].

decomposition is:

$$u(x,t) = \sum_q u_q sin(qx), \tag{1.9}$$

with q being the different modes of filament fluctuations expressed as $q = n\pi/l_c$, and $n = 1, 2, 3, \ldots$. The bending energy (**equation 1.6**) needs to be amended to include a term for the tension applied and is written now as:

$$H = \frac{1}{2}\int dx \left[\kappa\left(\frac{\partial^2 u}{\partial x^2}\right)^2 + \tau\left(\frac{\partial u}{\partial x}\right)^2\right] = \frac{l}{4}\sum_q (\kappa q^4 + \tau q^2) u_q^2. \tag{1.10}$$

Using the equipartion theorem one can rewrite the amplitudes:

$$\langle |u_q|^2 \rangle = \frac{2k_B T}{l_c(\kappa q^4 + \tau q^2)}. \tag{1.11}$$

To arrive at an expression for the fluctuation amplitude we integrate over all wave modes q to arrive at an expression for the average transverse filament fluctuations as driven by thermal energy:

$$\sqrt{\langle |u|^2 \rangle} = \sqrt{\int_{q_1}^{q_\infty} \langle |u_q^2| \rangle} \approx \left[\sum_{n=1}^{\infty} \frac{2k_B T}{\kappa n^4 \pi^4 / l^3 + \tau n^2 \pi^2 / l}\right]^{\frac{1}{2}}. \tag{1.12}$$

This result is plotted in **Figure 4.12** for multiple different contour filament lengths.

1.4.3 Biopolymer Network Mechanics

As we have seen above, the mechanics of biopolymer networks play a crucial role for many biological functions in a cellular context. Naturally there has been significant interest in studying these networks both by developing theoretical models, and experimental techniques. Since tissues as a whole are almost prohibitively complex, it is preferred to study their component networks in isolation for improved understanding in a bottom up approach. To this end many protocols have been developed to isolate proteins and reconstitute them into a network *in vitro* (see section 1.3.2.1 for collagen). When reconstituting biopolymer networks, many individual filaments either cross-link with the help of cross-linking proteins or become entangled. The resulting networks display many curious characteristics with respect to their mechanics. Biopolymer networks generally are *viscoelastic*, i.e. they behave both elastically like a Hookean spring, and resist flow like a viscous fluid. Upon the application of a force to the network, the first response is elastic and can be described using the Young's modulus:

$$E = \frac{\sigma}{\epsilon} = \frac{F/A}{\Delta L/L}, \tag{1.13}$$

where $\sigma = F/A$ is the stress, defined as force F per unit area A in units of Pascal. ϵ is the unitless strain of the material, written as $\epsilon = \Delta L/L$ in one-dimension. The Young's modulus is only useful for small strains, because often times the elasticity displays non-linear behavior at larger strain values. In that case we can use the differential modulus:

$$K = \frac{\partial\sigma}{\partial\epsilon}. \tag{1.14}$$

After the application of a force to the network, it slowly 'flows', i.e. internally rearranges to relax internal stress. To both incorporate elastic and viscous behavior into one parameter, one can use the dynamic (or complex) modulus G, which combines the storage modulus G' capturing the elastic behavior, and the loss-modulus G'' for viscous behavior. Under oscillatory loading conditions with frequency f, such that $\epsilon = \epsilon_0 sin(\omega t)$ and $\sigma = \sigma_0 sin(\omega t + \theta)$, with frequency $\omega = 2\pi f$, there will be a phase lag θ between stress and strain. For pure elastic materials, $\theta = 0$; a pure viscous material will display a phase lag $\theta = 90°$, with the strain lagging behind the stress. A viscoelastic sample will show a phase difference somewhere in between. The dynamic modulus is defined as:

$$G = G' + iG'', \tag{1.15}$$

$$G' = \frac{\sigma_0}{\epsilon_0} cos(\theta), \tag{1.16}$$

$$G'' = \frac{\sigma_0}{\epsilon_0} sin(\theta). \tag{1.17}$$

To detect such a response, often macroscopic bulk measurements are performed using a cone-plate rheometer (**Fig. 1.18**). The network is usually directly polymerized between the rheometer's plates. To measure a response to shear stress for instance, the top-plate is rotated with respect to the bottom plate. This can be done either linearly or oscillatory.

When subject to shear stress, most materials show an increase in volume caused by an internal positive stress that forms normal to the shear direction. One prominent example is polyacrylamide, a tunable hydrogel, which is often compared to various biopolymer networks. Polyacrylamide displays constant elasticity even under high strain [73] and exhibits positive normal stress [74]. Members of the cytoskeleton or ECM however show the opposite,

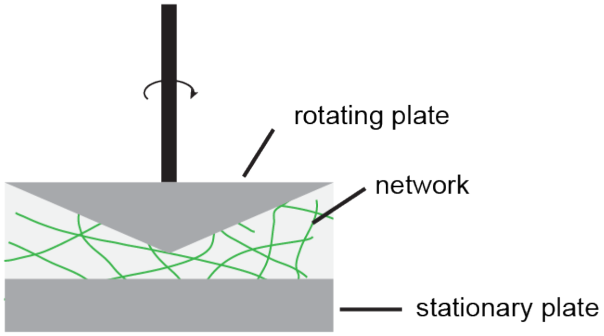

Figure 1.18: A cone-plate rheometer. As is used to measure shear stress response to a variety of bulk samples, such as a collagen network (fibrils in green) polymerized between the plates.

very unique response. Upon shearing, they contract and develop a *negative normal stress* [74]. This is thought to arise from the force response of individual filaments, recall the force extension curve we saw above (**Fig. 1.16**). A filament resists very strongly to stretching, but buckles more easily under compression. In a network with isotropic filament orientation, about the same number of filaments will be subject to compressive and stretching forces. But since the resistance to stretching is so much greater, there will be a net force pulling the network together.

The negative normal stress is also thought to be one of the origins of another highly notable property that almost all biopolymer networks display and which is not found in synthetic hydrogels: *strain-stiffening* (**Fig. 1.19**) [73]. *Strain-stiffening* describes the non-linear increase in stiffness under increasing strain, and can largely be thought of as a protective mechanism for tissues.

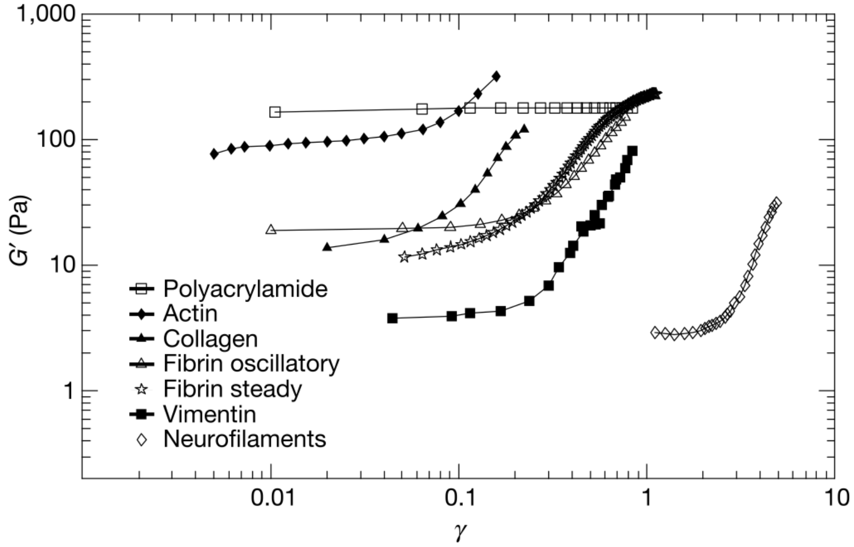

Figure 1.19: Shear-stress response for a variety of biopolymer networks. A shear strain γ is applied to a variety of different biopolymer networks and the storage modulus G' is calculated. A non-linear increase in stiffness with increasing strain, is seen in all but the synthetic hydrogel polyacrylamide, which is shown for comparison. Adapted with permission from [73].

While under very small strain, a network will respond in a primarily elastic manner (Hookean), but stiffen tremendously under great stress to maintain the integrity of tissues. As a contrast **Figure 1.19** also includes polyacrylamide, which shows constant elasticity over the range of strains tested. Besides being crucial for tissue integrity, it has also been shown that cells use these non-linear properties of the surrounding matrix to both communicate with each other and probe their surroundings [75,76]. In fact, *strain-stiffening* of the ECM in combination with the high resistance to stretch of individual filaments allows the cells to transmit mechanical signals up to 100s of micrometers into the network [77]. *Strain-stiffening* has been explained for the case of cross-linked actin networks as an entropic response [78], arising purely from the suppression of thermal fluctuations, which in the case of actin are expected to be on the order of 100s of nanometers.

In the case of collagen however, it is not entirely clear still today [47]. Modeling collagen networks is not trivial due to the hierarchy of many length scales involved. Molecular dynamics simulations are so far only possible for collagen molecules or individual microfilaments [79, 80], so inevitably one has to utilize simpler approaches. Popular models include 2- or 3-dimensional triangular lattices, or an assembly of rigid rods dubbed Mikado networks [81, 82]. Ensuing deformations can be treated as either affine or non-affine and collagen networks are usually assumed to be athermal (thermal fluctuations are assumed to be negligible). Affine deformations describe an equal stress distribution throughout the network, whereas non-affine denotes that different parts in the network experience varying degrees of strain. As we show later in this work, the stress distribution in a collagen network is highly heterogeneous (which points towards non-affine deformations), and the thermal fluctuations can be as large as 10s of nanometers, which might call the athermal assumption into question.

It is known that collagen networks are dominated by filament bending [81] and that the local network connectivity, which is described by the coordination number z can be used to quantitatively describe the network's behavior. z reports the number of filaments running away from a crossing point, e.g. at a crosslink of two filaments $z = 4$, and at a splitting of one filament (fork in the road) $z = 3$. For collagen $3 < z < 4$ on average, varying slightly with concentration and polymerization conditions. This in itself a curious fact, as for a network of purely elastic elements, the coordination number must be $z \geq 6$ in order for the network to be stable [83]. All in all, where the *strain-stiffening* response arises from in collagen on the microscopic level has been subject to much debate [68, 72, 73, 81, 82, 84], and may not be completely settled [47].

Chapter 2

Theory and Background

2.1 The Photonic Force Microscope

2.1.1 General Setup

The main instrument that facilitated our research is a custom-built Photonic Force Microscope (PFM), which has been carefully developed and improved over many years [18, 85, 86]. The current version was built and characterized in detail by two former Ph.D. students of Prof. Florin, Tobias Bartsch and Martin Kochanczyk [87, 88]. **Figure 2.1** shows a schematic drawing of the instrument setup.

2.1.1.1 The Laser

The main component of the instrument is an optical trap, which enables the manipulation of nanoparticles in solution. Optical traps have revolutionized many fields in the biosciences by allowing scientific studies on small length scales (see section 2.1.2 for a more detailed description of optical tweezers). As the main light source we use an infrared Ny:YAG laser (the Mephisto, wavelength $\lambda = 1064\,\mathrm{nm}$) developed by Innolight, Germany (now Coherent, USA), with a maximum power output of 500 mW. We chose an infrared laser to minimize the energy absorption of biological materials, and hence minimize potential photo damage to our substrates [89, 90]. The Mephisto is one of the most stable lasers on the market, as highlighted by its use at LIGO (Laser Interferometer Gravitational-Wave Observatory) [91], the large-scale experimental setup that recently detected gravitational waves for the first time. Laser stability encompasses a variety of different quantities, such as power stability on different time scales, pointing stability which describes beam wander, or beam divergence while propagating. For Thermal Noise Imaging and Activ-

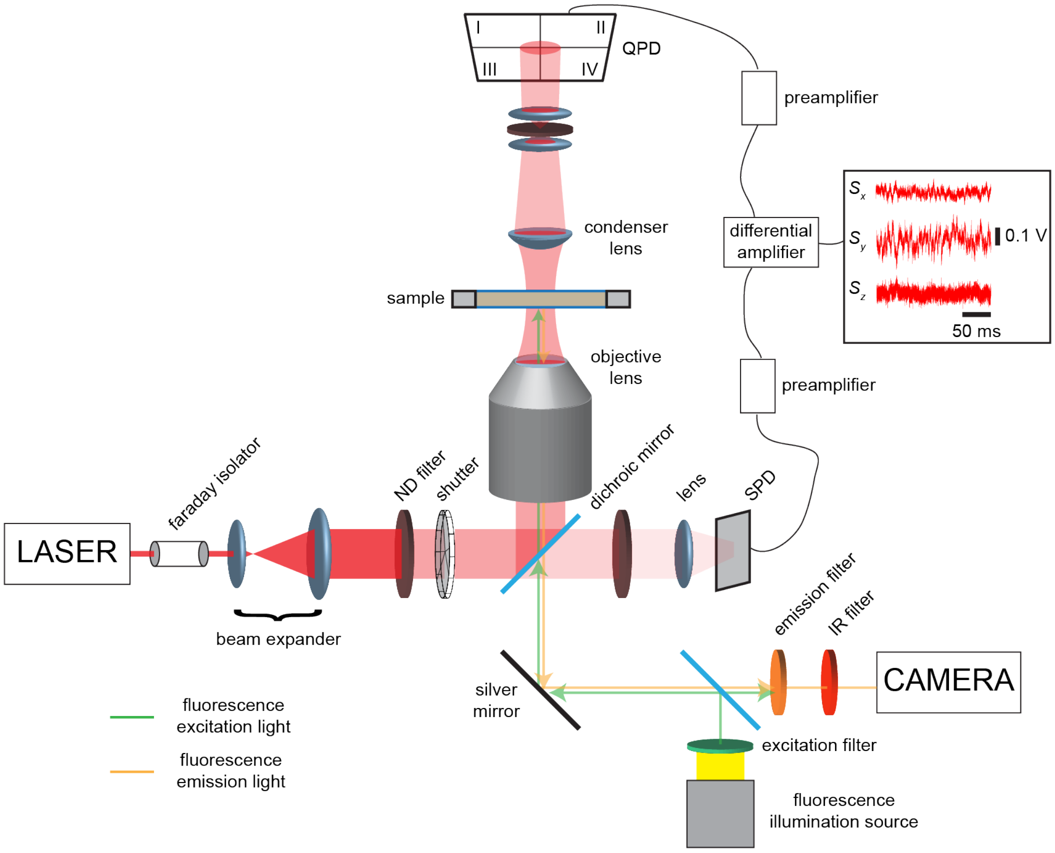

Figure 2.1: *Continued on the following page.*

Figure 2.1: The photonic force microscope. Left: an infrared Ny:YAG continuous wave laser ($\lambda = 1064\,\text{nm}$) is expanded via a beam expander, then passes a neutral density (ND) filter to attenuate $\sim 70\,\%$ of the power and an electric shutter. A dichroic mirror splits the beam: one part is travelling up towards the objective lens, is focused into the sample, collected again with a condenser lens and finally guided onto a quadrant-photo diode (QPD) via another pair of lenses and a ND-filter. The other part of the laser beam continues on horizontally, passing a ND-filter and a lens guiding it onto a single-photo diode (SPD). Both the QPD and SPD are amplified via respective pre-amplifiers and a differential amplifier, which then passes the signal onto the computer for digitization. Bottom: a white light fluorescence illumination source passes an excitation filter, which passes a narrow band around 560 nm. The fluorescence excitation light is guided upwards via a silver mirror, allowed to pass the dichroic mirror and focused into the sample via the objective lens. Emerging from the sample and travelling in the opposite direction, fluorescence emission light from fluorophores, which is Stoke's shifted to larger wavelengths will be reflected by the silver mirror, is allowed to pass the dichroic, emission filter and infrared (IR) filter into the camera. The latter two filters prevent possible back reflections of the fluorescence excitation light and laser light from entering the camera.

ity Microscopy we are primarily concerned with power stability, especially on short timescales. The performance of the laser in terms of power stability can be carefully characterized using power spectral density integration analysis [92]. To that end, the laser beam is guided onto a diode (see section 2.1.1.3) and the voltage signal is recorded with high bandwidth (1 MHz) and a high sampling rate $\geq 100\,\text{kHz}$ (**Fig. 2.2 a**). The resulting noisy signal time traces can then be Fourier transformed, and the distribution of the power over all relevant frequencies is plotted in a power spectral density (PSD) plot (**Fig. 2.2 b**). However, these plots are not easy to interpret, and deciphering which frequencies contribute most strongly to the noise can be difficult. The PSD is therefore integrated and displayed as the cumulative power spectrum (**Fig. 2.2 c**). Significant frequency contributions can now be easily identified by their corresponding steps in the cumulative plot.

2.1.1.2 The Beam Path

Let us return to **Figure 2.1**. After exiting the laser, the beam first travels through a Faraday isolator, which prevents back-reflections into the laser cavity and thereby resulting instabilities. It works by first sending the beam through a polarizer, rotating it by 45° and again passing a second polarizer which is aligned at 45° with respect to the first one. Any back reflection will be rotated by an additional 45°, and therefore be aligned perpendicular to the initial polarizer, effectively blocking it. The beam is then expanded from its initial $\sim 0.5\,\mathrm{mm}$ beam diameter to several centimeters, using the beam expander, a telescope of two lenses with differing focal lengths, after which we place a neutral density (ND) filter to attenuate $\sim 70\,\%$ of the power, together with an electronically regulated mechanical shutter. The beam continues hitting a beam splitter, which sends the majority of the light upwards into the objective lens. A small portion is allowed a to continue towards a single photo diode (SPD), with the passage of another ND-filter and a spherical lens. The SPD monitors the laser's long-time scale fluctuations (on the order of seconds and minutes) and via a feed-back loop is able to correct the injection current into the laser to stabilize it. The part of the laser beam travelling upwards,

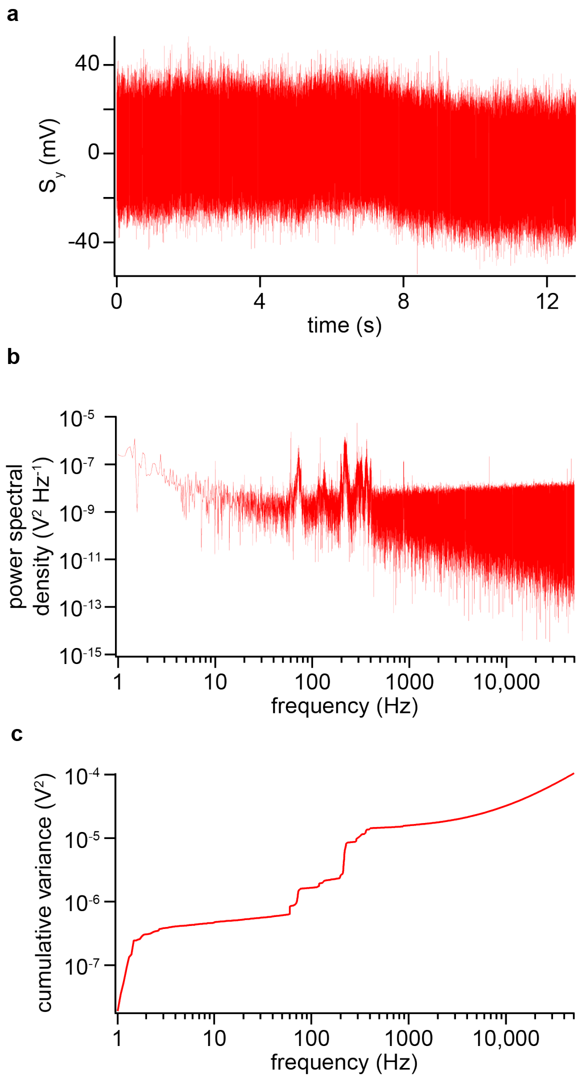

Figure 2.2: Quantifying laser stability. a shows the fluctuating voltage signal as read out by the quadrant photo diode, for a laser beam focused in sample only containing water. As such the noise is dominated by laser power instabilities and beam jitter and wander, but also mechanical vibrations of optical components. The noisy time trace is Fourier transformed and the power spectrum plotted in **b**. The power spectrum is integrated and displayed in **c**. The cumulative power spectrum helps to identify significant frequencies via steps in the graph.

overfills the back aperture of our objective lens, which focuses the light into the sample chamber. The objective lens is a water immersion, high numerical aperture ($60\times; \mathrm{NA} = 1.2$) lens used to achieve stable trapping and designed to take into account the thickness of the lower glass coverslip of the sample. The reason for choosing a water immersion lens instead of oil immersion is to avoid an index of refraction mismatch with the sample solution. Such a mismatch can cause undesirable aberrations. In practice, instead of water we use an immersion oil with the same index of refraction as water, but with a much lower vapor pressure, resulting in negligible evaporation over the course of many hours. After passing through the focal spot and sample area the light is gathered again by a condenser lens and finally guided towards the detector stage via a dichroic mirror and a $1:1$ telescope including another ND-filter.

2.1.1.3 The Detector

The detector's main component is the quadrant-photo diode (QPD) (G6849, Hamamatsu Corporation, NJ, USA). The QPD is a circular diode that has four distinct, independent sections (**Fig. 2.3**) and can therefore produce three unique signals which are described as:

$$S_x = (S_I + S_{III}) - (S_{II} + S_{IV}), \tag{2.1}$$

$$S_y = (S_I + S_{II}) - (S_{III} + S_{IV}), \tag{2.2}$$

$$S_z = S_I + S_{II} + S_{III} + S_{IV}. \tag{2.3}$$

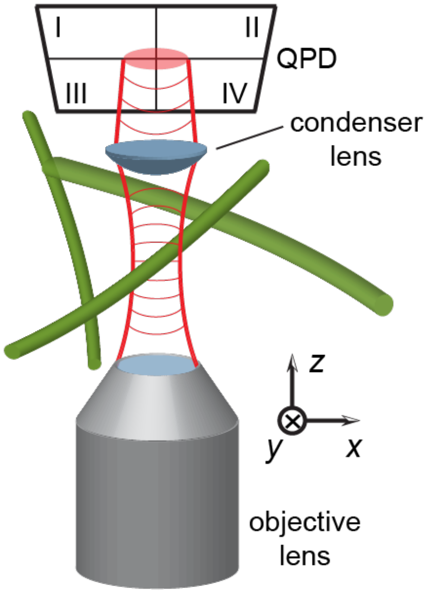

Figure 2.3: The detector setup. A near infrared laser beam is focused into the sample, then collected by a condenser lens and guided onto a quadrant-photo diode (QPD).

The signals are pre-amplified, sent to a custom built differential amplifier (SA500, Oeffner MSR, Plankstadt, Germany) and finally recorded and digitized via a data-acquisition board (DAQ) from National Instruments (National Instruments, Austin TX, USA). The DAQ has a 16-bit resolution analogue-to-digital converter and an electronic bandwidth of 1 MHz. The latter roughly describes the maximum input signal variation frequency that the detector will pick up, i.e. even when working with a sampling frequency $< 1\,MHz$ the detector will at most average over $1\,\mu$s per data point. This is crucial when tracking freely diffusing particles (**Fig. 2.7**), in order to minimize the position error obtained through motion blur.

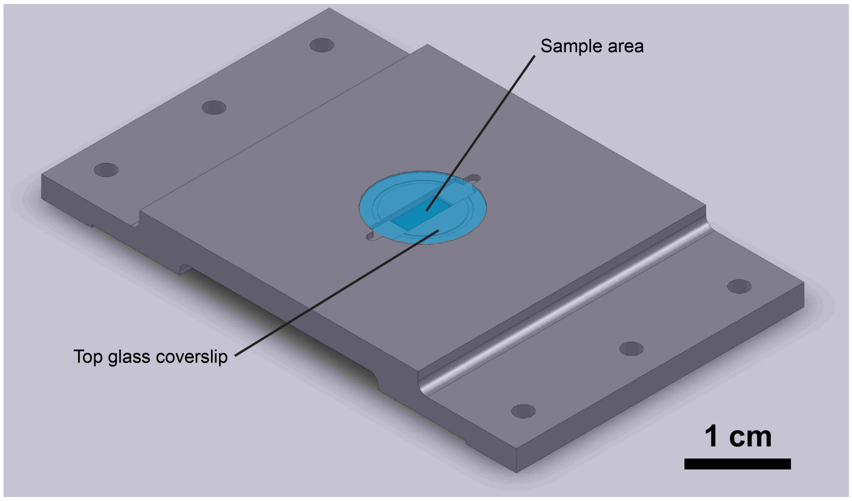

Figure 2.4: Sample chamber. A render of the sample chamber used is shown. The sample is contained within the center rectangular volume between the top and bottom coverslip (blue).

2.1.1.4 Sample Positioning

The sample is held inside a single piece sample chamber (**Fig. 2.4**) manufactured either out of titanium (for its biocompatibility), or aluminum. The center cut-out is covered with two round glass coverslips, roughly 170 μm in thickness, and has a total sample volume of $\approx 60\,\mu$l. The sample chamber is fastened onto a three-dimensional nanopositioning piezostage (Nano-View/M375HS, Mad City Labs, WI, USA). The stage can travel 75 μm laterally and 50 μm axially with a high resolution stepsize. When tested under experimental conditions ~ 1 nm steps could be resolved. It has also a fast response time (< 10 ms) and high resonant frequency in the kHz-range, which makes it resistant to excitation in the low acoustic range, and therefore maximizes mechanical stability. The entire stage assembly is mounted additionally on a translational stage which can travel laterally via the use of micrometer screws. Thus the entire sample area can be explored.

2.1.1.5 The Camera - Brightfield and Fluorescence Microscopy

In addition to the main optical path of the laser, we integrate fluorescence microscopy into the PFM. The light of a fluorescence excitation source is guided towards the setup using an optical fiber, decoupled out of the fiber using an array of lenses and sent towards a filter cube. The filter cube contains an excitation filter (passing a narrow band around $\sim 560\,\mathrm{nm}$), emission filter (blocking wavelengths below $\sim 600\,\mathrm{nm}$ but passing longer wavelengths) and dichroic mirror. The excitation light is sent up into the sample chamber by a silver mirror. Likewise, any emitted light from a fluorophore is collected again by the objective lens, guided back downwards and reflected back towards the filter-cube via the silver mirror. This time however, due to the Stoke's shifted wavelength the light will pass the dichroic mirror in the filter cube and move towards a CCD camera. Overall, the addition of fluorescence microscopy allows for the straightforward viewing of fluorescently labelled nanoparticles or biological structures, that would otherwise be too small to be visible due to the diffraction limit. Likewise a brightfield illumination source on the other side of the condenser lens allows for brightfield microscopy (not shown in **Fig. 2.1**).

2.1.1.6 Mechanical Stability

Overall the PFM setup was designed and built with an emphasis on mechanical stability. All components are fixed to an optical table which is suspended pneumatically to decouple the table from any building vibrations. Furthermore, most optical components are mounted using the Owis (Owis GmbH, Staufen, Germany) rail and rider system allowing for ease in installation and switching out components, as well as a high degree of stability. Before every experiment the instrument's vibrations over a wide frequency spectrum ($1\,\mathrm{Hz} - 50\,\mathrm{kHz}$) are tested via a baked bead assay (see section 2.1.7). Further details about the PFM design can be found in Martin Kochanczyk's Ph.D. thesis [88].

2.1.2 Optical Tweezers

The concept of a stand-alone single beam optical trap was first realized by Arthur Ashkin in 1986 [94] who was most recently honored with the Nobel Prize in Physics in 2018 [95]. Within the thirty years after their development, optical tweezers have rapidly become an indispensable tool in many parts of Physics, Biotechnology, and other disciplines. They are used to either hold small objects in place, track their motion or apply piconewton forces to single molecules [19, 96, 97]. Optical tweezers are most commonly used to trap dielectric nanoparticles in solution, e.g. polystyrene or silica beads of a variety of sizes from $10\,\mu\mathrm{m}$ down to $25\,\mathrm{nm}$. These are not fixed limits however. More complicated beam architectures can be devised to trap objects $< 10\,\mathrm{nm}$ [98],

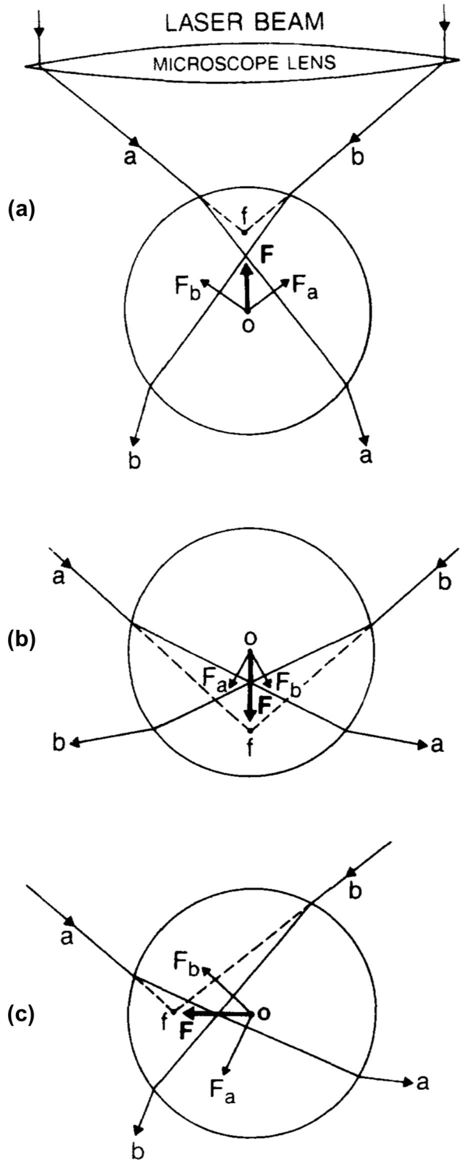

Figure 2.5: Geometrical optics for a sphere held in an optical trap. A microscope lens (top) focuses a laser beam (here represented by two rays a and b converging at focal point f). Upon entering the spheres, the light rays are refracted and momentum is transferred to the sphere, resulting in forces F_a and F_b, with net force **F** pulling the sphere towards the focal point f. This is true for vertical (**a**,**b**), as well horizontal displacements (**c**). Adapted with permission from [93].

or counter propagating beams can be used to trap entire cells [99] several tens of micrometers in size. They can even be utilized to apply stretching forces to trapped cells [100]. For our purposes, we focus on a single beam trap for nanoparticles in solution. For trapping to occur, the index of refraction of the bead's material n_{particle} must be higher than that of the surrounding medium n_{medium}. To understand how a freely diffusing particle can be held in place it is helpful to distinguish between different size regimes. If the particle's radius r is significantly larger than the laser's wavelength $r \gg \lambda$, geometrical optics arguments are appropriate to apply [101], as shown in **Figure 2.5**. Consider **Figure 2.5 a**: a high NA lens focuses a beam of light, two light rays a and b, which travel towards their focal point f. Along the way they encounter the microsphere and are refracted both upon entering and existing the sphere. The propagation direction of the light changes and transfers momentum to the sphere. If the sphere is centered horizontally there will be a net force F pointing upwards as indicated, pulling it towards the focal point f. If we neglect scattering forces for now, the focal point represents a stable point of equilibrium. Remember that the sphere is located in solution and is subject to random thermal forces. **Figure 2.5 b** and **c**, show two cases of vertical and horizontal displacement that can result from such thermal kicks. It can be seen that there will always be a net force pulling the sphere back towards its equilibrium point. If we now also consider scattering forces F_{scat}, we will see that the true equilibrium point is located slightly below the focal point, which does not change the rest of our argument however.

Particles that are much smaller in radius than the wavelength of light $r \ll \lambda$, fall into the Rayleigh regime. Here, one can treat the particle as a point dipole in the varying electromagnetic field of the light beam. Ashkin derived the following expressions for the scattering and gradient forces for that case: [94]:

$$F_{\text{scat}} = \frac{I_0}{c}\frac{128\pi^5 r^6}{3\lambda^4}\left(\frac{m^2-1}{m^2+2}\right) n_{\text{med}}, \tag{2.4}$$

$$F_{\text{grad}} = -\frac{n_{\text{med}}}{2}\alpha\nabla E^2 = -\frac{n_{\text{med}}^3 r^3}{2}\left(\frac{m^2-1}{m^2-2}\right)\nabla E^2, \tag{2.5}$$

where I_0 is the intensity, r the radius of the particle, and λ the wavelength of light. n_{med} is the refractive index of the solution, whereas the ratio with the refractive index of the sphere is defined as $m = n_{\text{sphere}}/n_{\text{med}}$ and called the effective index of refraction. Finally, α represents the polarizability which relates the dipole moment with the electric field $\vec{p} = \alpha\vec{E}$. As mentioned above F_{scat} actually pushes the particle slightly beyond the focal point. It is therefore a necessary condition for stable trapping that:

$$R = \frac{F_{\text{grad}}}{F_{\text{scat}}} \geq 1, \tag{2.6}$$

which imposes a constraint on the materials, wavelength of light and power that can be used.

2.1.3 Nanoparticle Optically Trapped in Solution

2.1.3.1 Brownian Motion

A nanoparticle in an aqueous solution will undergo a process of random movements called Brownian motion. Brownian motion arises due to the thermal energy of both the particle and the surrounding water molecules and their random collisions. The particle receives roughly $\sim 10^{14}$ kicks per second, each time changing its direction [102]. The resulting random walk is a peculiar kind of motion and hard to describe exactly. In between successive collisions, the particle undergoes ballistic motion which is not easy to observe due to its very fast time scale. Only recently it was observed and measured using a very fast detector [103]. On longer time scales the particle's motion is diffusive and can be described using arguments from statistical mechanics. This was first worked out by Einstein in 1905 [104]. He concluded that while the average displacement over time for a free particle:

$$\langle \Delta x(t) \rangle = \langle (x(t) - x(0)) \rangle = 0, \tag{2.7}$$

the mean square displacement (MSD) in one dimension grows proportional with time:

$$\left\langle (\Delta x)^2 \right\rangle = 2Dt = 2\frac{k_B T}{\gamma} t. \tag{2.8}$$

The diffusion constant D relates the thermal energy $k_B T$, given by the Boltzmann constant k_B and the temperature T, and the Stoke's drag coefficient $\gamma = 6\pi\eta r$, where η is the viscosity of the fluid, and r the radius of the particle.

2.1.3.2 The Langevin Equation

More generally, the above result can be derived by using a force balance equation with a random force term first introduced by Paul Langevin in 1908 [105, 106]:

$$m\ddot{x}(t) = -\gamma \dot{x}(t) + \delta F_{th}(t). \tag{2.9}$$

The first term on the right is the friction force caused by viscous drag, which is proportional to the bead's velocity and the Stoke's drag coefficient. The last term describes a random thermal force, best expressed via delta functions. Since it is a random quantity, the true expression for this force is not known, however, one can describe statistical quantities such as its moments:

$$\langle \delta F_{th}(t) \rangle = 0, \tag{2.10}$$

$$\langle \delta F_{th}(t) \delta F_{th}(t+\tau) \rangle = 2 k_B T \gamma \delta(t-\tau). \tag{2.11}$$

The prefactor for the second moment in **equation 2.11** comes from the fluctuation dissipation theorem. With some mathematical tricks and manipulation a general expression for the MSD of a freely diffusing particle can be derived:

$$\left\langle x^2 \right\rangle = \frac{2k_B T}{\gamma} \left[t + \frac{m}{\gamma} \left(\exp\left[-\frac{\gamma t}{m} \right] - 1 \right) \right]. \tag{2.12}$$

Here, a relevant time scale is $\tau_r = m/\gamma$ describing a relaxation time for the particle ($\tau_r \approx 2.6\,\text{ns}$ for a 200 nm diamterer polystyrene sphere in water).
If $t \gg \tau_r$ we recover Einstein's expression (see **equation 2.8**). For shorter times $t \ll \tau_r$ we are in the ballistic regime in between random kicks that the particle receives from surrounding fluid particles, and the motion will be proportional to time:

$$\left\langle x^2 \right\rangle \approx \frac{k_B T}{m} t^2. \tag{2.13}$$

2.1.4 Confined Brownian Motion

The energy landscape of an optical trap can approximately be described by a harmonic three-dimensional potential:

$$U = \frac{1}{2}(k_x x^2 + k_y y^2 + k_z z^2), \tag{2.14}$$

where k_i's are the spring constants of the trap in all three spatial dimensions $i = x, y, z$. When considering confined Brownian motion, one can add a restoring force term $F = -k_x x$ to the Langevin equation, here considered in one dimension for simplicity:

$$m\ddot{x}(t) = -\gamma\dot{x}(t) - k_x x + \delta F_{th}(t). \tag{2.15}$$

For the case of trapped nanoparticles we are usually operating in a low Reynold's number regime, i.e. inertial forces are negligible when compared to viscous drag forces. The left-hand side of the Langevin equation can therefore be set to zero:

$$\dot{x}(t) = -\frac{k_x}{\gamma}x(t) + \frac{1}{\gamma}\delta F_{th}(t). \tag{2.16}$$

To recover an expression for the MSD it is helpful to consider the position autocorrelation function of the particle. It describes the time scale over which the particle 'feels' the restoring force of the trap. The associated autocorrelation time constant should therefore be inversely proportional to the trap's stiffness. The autocorrelation function is related to the MSD by:

$$\left\langle (\Delta x(t))^2 \right\rangle = \left\langle (x(t) - x(0))^2 \right\rangle = 2\left\langle x^2 \right\rangle - 2\left\langle x(t)x(t+t') \right\rangle . \tag{2.17}$$

We can find an expression for the autocorrelation function, as well as make use of the equipartition theorem:

$$\langle x(t)x(t+t')\rangle = \frac{k_BT}{k_x}\exp\left[-\frac{k_x}{\gamma}t'\right], \tag{2.18}$$

$$\left\langle x^2\right\rangle = \frac{k_BT}{k_x}. \tag{2.19}$$

This finally leads to an expression for the MSD of confined Brownian motion:

$$\left\langle(\Delta x(t'))^2\right\rangle = 2\frac{k_BT}{k_x}\left(1-\exp\left[-\frac{t'}{\tau_x}\right]\right). \tag{2.20}$$

Note, that while the MSD for a freely diffusing particle grows proportional to time, in the confined case it reaches a maximum within a particular time τ_x. This is called the autocorrelation time and is related to the drag coefficient as well as the trap's stiffness:

$$\tau_x = \frac{\gamma}{k_x}. \tag{2.21}$$

2.1.5 Distribution of Particle Positions

As the trapped nanoparticle explores the entire trapping potential, it will eventually reach thermal equilibrium. We expect for the particle to spend the majority of its time in the center of the trap. What the probability is to find the particle in a particular part of the trap is shown in the following. Let us assume a volume element of side length dl. The probability of finding the particle in the small voxel $(d\mathrm{l})^3$ is:

$$P = p(d\mathrm{l})^3, \tag{2.22}$$

where the probability density p is given by the Boltzmann distribution:

$$p(\vec{r}) = C \exp\left[-\frac{E(\vec{r})}{k_B T}\right]. \tag{2.23}$$

The constant C can be found by normalizing the distribution $\iiint p(\vec{r}d\vec{r} \overset{!}{=} 1)$ and comes out to be $C = \frac{\sqrt{k_x k_y k_z}}{(2\pi k_B T)^{3/2}}$. The distribution resembles a three-dimensional Gaussian distribution and is visualized in **Figure 3.3 b**.

Suppose now we are tracking the particle in its exploration of the trap and sampling the particle's positions via measuring a certain amount of data points N over a certain amount of measurement time T. We can then calculate the expected number of times that the particle will visit each voxel, the voxel occupancy count:

$$n(x, y, z) = N(d\mathrm{l})^3 \frac{\sqrt{k_x k_y k_z}}{(2\pi k_B T)^{3/2}} \exp\left[-\frac{E(x, y, z)}{k_B T}\right]. \tag{2.24}$$

Using the above equation, one can extract the true underlying energy landscape by solving for E:

$$E(x, y, z) = -k_B T \ln\left[n(x, y, z)\right] + C', \tag{2.25}$$

where we can ignore the additive constant C' as it solely represents an offset in the potential energy. The above expression can be used to determine the trap's stiffness when it is fitted with a harmonic potential curve [107]. In practice however, **equation 2.21** for the autocorrelation time is used. Given that we know the dimensions of the bead and viscosity of the solution, we can determine the drag coefficient γ. We then calculate the autocorrelation function and fit it with an exponentially decaying function to determine the autocorrelation time τ.

2.1.6 Thermal Noise Imaging

Thermal Noise Imaging (TNI) was first introduced in 2001 [86] as a scanning probe technique for the imaging of biological matter, like filaments or networks, but has remained a formidable challenge to realize quantitatively until recently. It uses a combination of a nanoparticle (the scanning probe) together with an optical trap as a three dimensional scanner. The continuous position fluctuations of the probe within the trapping volume are tracked and monitored via a three-dimensional position detector (see section 2.1). The system of optical trap and bead is then moved close enough to an object of interest to overlap with it. The object will then sterically hinder the probe from fully exploring the previously available volume. In this way TNI generates a negative image of the objects in space. Even though the probe interacts with the object of interest, it does so with the minimal force possible, namely thermal forces. TNI works in solution, which is a strong advantage as usually biological samples are in their most natural state when in aqueous solution. TNI relies on a very precise and fast position detector to track the fluctuating probe particle, which is outlined in detail in the following sections.

2.1.7 Three-dimensional Position Detection

Tracking the three-dimensional position of the probe particle while it explores the entire trapping potential is achieved via back-focal plane interferometry. Gittes *et al.* [108] (for one dimension) and later Pralle *et al.* [109] (for three dimensions) showed for Rayleigh spheres ($r \ll \lambda$), that the bead's position can be monitored by reading out intensity fluctuations in the back-focal plane of the condenser lens using a QPD. Within the trapping volume, the part of the laser light that hits the particle is scattered and interferes with the unscattered portion of the light. This forms an interference pattern of changed intensity on the QPD. Recall **equations 2.3** from above restated here, indicating three signal outputs from the QPD:

$$S_x = (S_I + S_{III}) - (S_{II} + S_{IV}), \tag{2.26}$$

$$S_y = (S_I + S_{II}) - (S_{III} + S_{IV}), \tag{2.27}$$

$$S_z = S_I + S_{II} + S_{III} + S_{IV}. \tag{2.28}$$

In the lateral directions, x and y, the signals S_x and S_y represent the difference between left and right half, and top and bottom half of the QPD respectively. The detector response to a lateral position shift of the particle is most easily studied by deliberately moving a nanoparticle fixed to the bottom glass coverslip through the focus of our trap. **Figure 2.6 a** and **b** show the respective signal outcomes when the bead is moved in the x- and y-direction and are somewhat intuitive. When the bead is moved in the axial direction however, the signal S_z (**Fig. 2.6 c**), which represents the sum of all four QPD quadrants, looks strikingly similar to the previous case and it is not obvious why that is the case. To understand this response, one has to consider the Gouy phase shift. A Gaussian beam of light will undergo a gradual phase shift of π when passing through the focal area. Thereby, when the particle is located below the focus, the scattered and unscattered portions of the light interfere

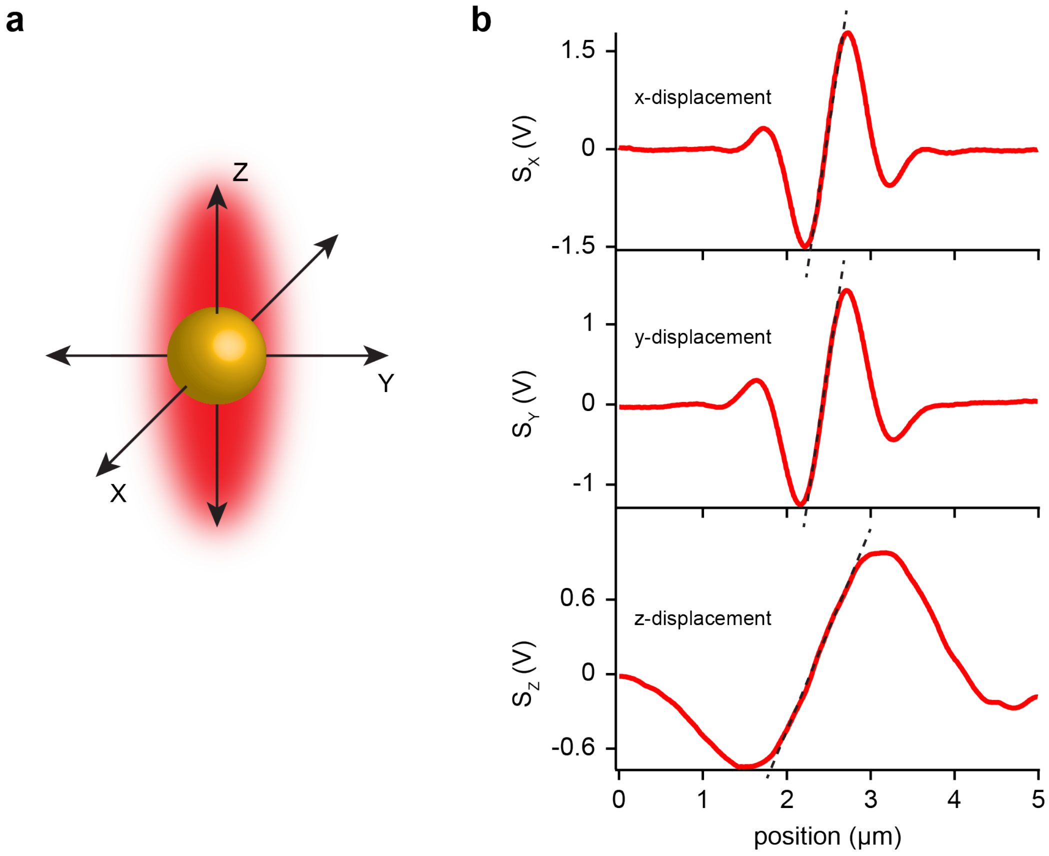

Figure 2.6: Detector response of a spherical particle. (**a**) A nanosphere (gold) is moved through an optical trap (red shading) in all three spatial directions. The respective detector response curves for the signals S_x for a x-displacement, S_y for a y-displacement and S_z for z-displacement are shown in **b**.

destructively due to a phase difference of π between them. The closer the particle moves towards the focus the more the phase difference will decrease, until it reaches zero and the two portions of light interfere constructively. Therefore, the signal S_z increases when the particle moves up, along the propagation direction of light. Note, that all three detector response curves have a prominent linear range (marked by black dashed lines), which relates the position change to the voltage read out and can be used to calibrate the detector for our fixed bead example: the position change is known given by the motion of the stage and the resulting voltage response of the detector is measured. The slope of the linear range is therefore referred to as the detector sensitivity.

2.1.8 Calibration and Correction of Nonlinearities of the Detector

In order to record thermal noise images, we desire to calibrate the detector for a freely diffusing particle without fixing it in place and moving it through the trap. As the detector response relies on detecting the interference pattern between scattered and unscattered light, it is heavily influenced by slight variations in bead size: for Rayleigh scatterers the scattering intensity $\propto r^6$, and bead diameters for commercially available nanoparticles tend to vary ±10 %. Another issue with the detector sensitivity can be recognized when closely observing the response curves in **Figure 2.6**. The width of a truly linear dependence is comparatively narrow, and outside of it the sensitivity rapidly starts to deviate from linear behavior. We can conclude that the sensitivity is dependent on the position of the particle in the trap. This complicates the matter, but a solution was introduced by Tischer *et al.* in 2004 [110] to calibrate, and linearize the detector locally with a freely diffusing particle at or near the location in the sample where the measurement is to be made. Recall **equations 2.8** and **2.20** from above, that describe the mean squared displacement of a freely diffusing particle and a confined Brownian particle, respectively. Let us suppose we trap a 200 nm diameter particle in aqueous solution in an optical trap with stiffness constants typical in TNI experiments $k_x = 1.5\,\mathrm{pN}\,\mu\mathrm{m}^{-1}$, $k_y = 1.0\,\mathrm{pN}\,\mu\mathrm{m}^{-1}$ and $k_z = 0.15\,\mathrm{pN}\,\mu\mathrm{m}^{-1}$. Given the viscosity of water $\eta = 8.9 \times 10^{-4}\,\mathrm{Pa\ s}$ we can use the Stoke's drag coefficient to calculate the autocorrelation times, which were $\tau_x = 1.1\,\mathrm{ms}$, $\tau_y = 1.7\,\mathrm{ms}$ and $\tau_z = 11\,\mathrm{ms}$.

Figure 2.7 a plots the MSD for confined Brownian motion (red) of the particle and for the case of the same particle freely diffusing (blue) in the x-direction. In the former case, one can see the expected plateau in the MSD, as well as the linear dependence on time in the latter case. **Figure 2.7 b** plots the actual displacement of the particle which is simply the square root of the MSD. If inspecting shorter time-scales of $t < \tau_x$ (see inset) both overlap, we can see that even in the confined case the MSD is unchanged from the free case.

This observation can be used to calibrate the detector locally throughout the trapping volume (note that most equations are described only for the x-direction for simplicity, but translate to the other two spatial dimensions as well). After tracking the thermal motion of our trapped particle for some time and recording time traces $S_x(t)$, $S_y(t)$ and $S_z(t)$, suppose we pick out a small volume element in the trapping volume, a voxel, centered around (x_0, y_0, z_0). Then we study the portion of the trajectory relating to the time it spent occupying the voxel of interest. We can express the local, uncalibrated MSD

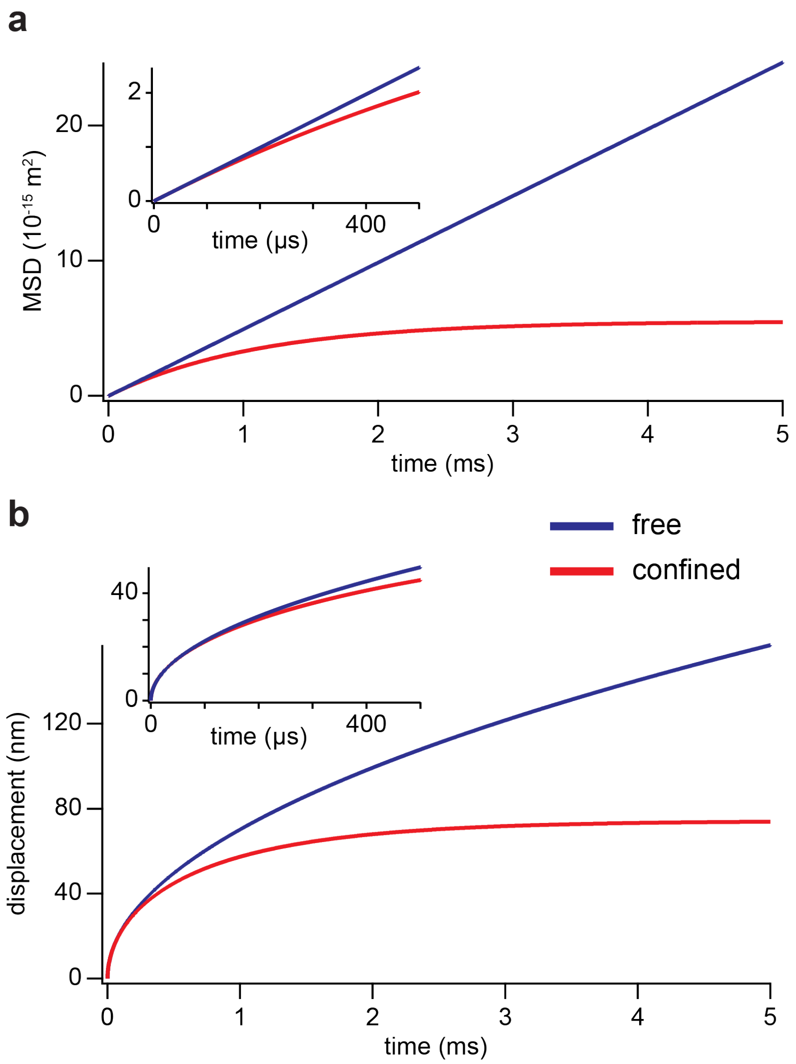

Figure 2.7: Mean squared displacement in one dimension of a freely diffusing nanosphere in solution, versus trapped in a harmonic potential. (**a**) A nanosphere of 200 nm in diameter is freely diffusing in water at room temperature (blue), or trapped in a harmonic potential with stiffness constant $k = 1.5\,\mathrm{pN}\,\mu\mathrm{m}^{-1}$ over a time scale of 5 ms. Inset shows the first 500 μs. **b** plots the true displacement. The inset shows that up to ~ 20 nm the displacement of a freely diffusing particle and a trapped one are almost indistinguishable.

as:

$$\mathrm{MSD}_L^*(S_{x_0}, t) = \frac{1}{N} \sum_{S_{x_0}-\delta S_x < S_x(t) < S_{x_0}+\delta S_x} \left[S_x(t'+t) - S_x(t')\right]^2 \tag{2.29}$$

$$= \left(\frac{\partial S_{x_0}}{\partial x}\right)^2 2Dt, \tag{2.30}$$

where the first term in the second line is the local detector sensitivity:

$$\frac{\partial S_{x_0}}{\partial x} = \sqrt{\frac{\mathrm{MSD}_L^*(S_{x_0}, t)}{2Dt}}. \tag{2.31}$$

Once we know the local detector sensitivity for all voxels in the trapping volume we can reconstruct the true particle positions by realizing that the sensitivity relates the detector output with the particle position and integrating:

$$\frac{\partial S_x}{\partial x} = \frac{dS_x}{x}, \tag{2.32}$$

$$x(S_x) = \int \frac{1}{\partial x / \partial S_x'} dS_x'. \tag{2.33}$$

2.2 Activity Microscopy

Two-dimensional Activity Microscopy (aMic) is first introduced in this work as a direct consequence of TNI. The link will become more apparent in later chapters. However, in this section we will briefly introduce the concept and idea behind our new method. aMic uses the same PFM as described above and relies on our focused laser beam as a scanner, albeit this time without a probe particle. aMic produces two important outputs: First, scanning Activity Microscopy is capable of finding the precise location of small objects with

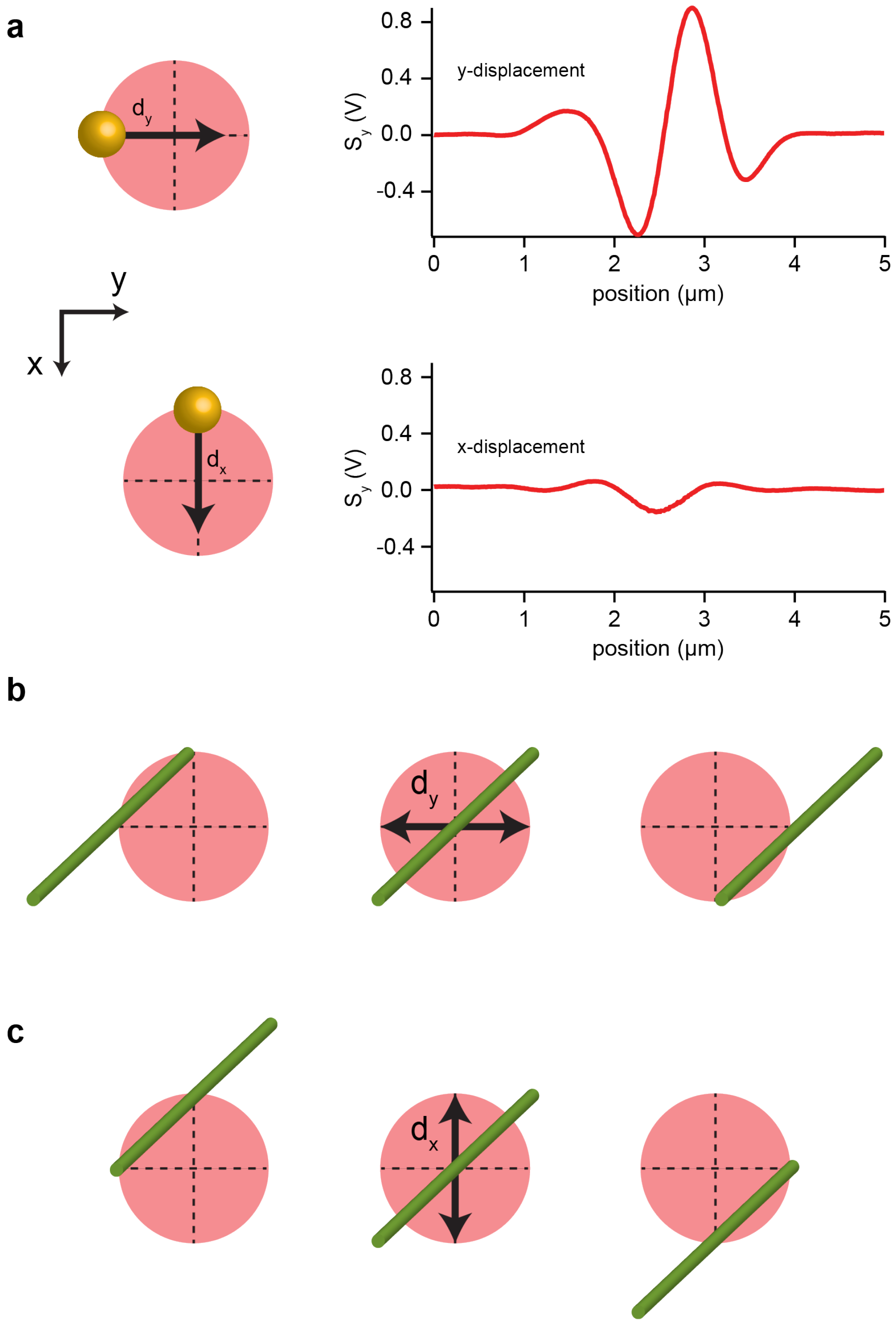

Figure 2.8: *Continued on the following page.*

Figure 2.8: Detector response of a spherical versus a cylindrical object. (**a**) The detector response signal S_y for a y displacement of a sphere is plotted (top, right) and compared to the same channel output for a x displacement (middle, right). The latter is insignificant to the former. Red circles (left, top and middle) represent the QPD and its four quadrants sectioned off by dashed lines. **b** shows the horizontal (y) displacement of an infinitely long cylinder (radius $<$ focal spot $\sim 300\,\text{nm}$ laterally). It can be seen, that while the detector response S_y, which represents the difference between the left and right half of the QPD, will be significant, so will be the response in S_x, which represents the difference between the top and bottom half. In fact, their response will be similar in magnitude. In **c** the cylinder is displaced along the vertical (x) direction starting from the same location. Since in the example displayed the cylinder is aligned at $\sim 45°$ with respect to both axes, the detector response is independent of direction of travel.

nanometer precision as long as the object is smaller than the extent of the focal spot ($\sim 300\,\text{nm}$ laterally). This is done with the help of the detector response function. Recall the response curves for a fixed spherical particle that is moved through the trap (**Fig. 2.6**). The detector sensitivity is given by the spatial derivative for the respective direction. It can be seen, that if the particle is located at the center of the trap, the detector sensitivity reaches a local maximum. This fact can be used to find the position of the object. Finding the local maximum can be done with little error via fitting a Gaussian to the derivative, which results in the high precision of the localization. Secondly, aMic can quantify the thermal fluctuations of an object in the trap. To outline this, let us continue with the above example of a spherical particle fixed to the lower coverslip of our sample chamber (see **Fig. 2.4**). After we have determined the exact location of the particle we can position it in the center of the laser focus. While the particle is fixed onto the lower coverslip of the sample, it will still undergo small scale thermal fluctuations, mainly dominated by sample and instrument instabilities. These fluctuations can be monitored by continuously reading out the detector signals in all three dimensions. The resulting time traces $S_i(t)$ ($i = x, y$, or z) display the change in voltage over time, but can be calibrated using the detector's sensitivity $\frac{\partial S_i}{\partial i}$. We can then take the standard deviation σ_{S_i} of the fluctuations and calculate the fluctuation amplitude:

$$u_i = \frac{\sigma_{S_i}}{\partial S_i / \partial i}, \tag{2.34}$$

or calculate the power spectrum to find well represented frequencies and their associated power. In fact, this very example was used on a regular basis to monitor mechanical instabilities in the instrument.

So far we are dealing with a spherical particle which has rotational symmetry. As a result, we could treat each spatial dimension separately, the respective signals are orthogonal to each other and there is very little cross-talk. This can be seen in **Fig. 2.8**. Panel **a** shows the case for a sphere. When it is moved through the focus in the y-direction, we see a significant signal response (and therefore a significant sensitivity) in S_y. When the sphere is moved into the x-direction the response is negligible. The same is true in reverse for the S_x channel. We can therefore treat S_x and S_y as orthogonal and write:

$$S_x = \lambda_{xx} d_x, \tag{2.35}$$

$$S_y = \lambda_{yy} d_y, \tag{2.36}$$

where $\lambda_{xx} = \frac{\partial S_x}{\partial x}$ and $\lambda_{yy} = \frac{\partial S_y}{\partial y}$ are the sensitivities and d_x and d_y the replacement in the respective dimension. A diagonal translation d of the particle through the focal spot can be decomposed into its x and y components and calculated as:

$$d = \left[\left(\frac{S_x}{\lambda_{xx}} \right)^2 + \left(\frac{S_y}{\lambda_{yy}} \right)^2 \right]^{\frac{1}{2}} . \tag{2.37}$$

We would like the above concept to be generalized to a more complicated structure however. As we will see in Chapter 4, we applied aMic to an *in vitro* collagen network. In this case, the dominant shape is a cylinder (the collagen fibril). Collagen fibrils were roughly $\sim 160\,\text{nm}$ in diameter and therefore fulfill our size condition above (it is smaller than the extend of the focal spot). Here, the assumption of orthogonality between S_x and S_y does not hold anymore [111]. This is best seen when studying the lower half of **Figure 2.8**. An infinitely long cylinder that is not aligned with any of the axes, and is translated through the focal spot along the y-direction (**Fig. 2.8 b**) causes a signal in both S_x and S_y. This is also true when the cylinder is translated in the x-direction (**Fig. 2.8 c**). In fact for the special case of a 45° alignment as displayed in **Figure 2.8**, the detector responses will be independent of translation direction. This means that **equations 2.35** and **2.36** need to be amended:

$$S_x = \lambda_{xx} d_x + \lambda_{xy} d_y, \tag{2.38}$$

$$S_y = \lambda_{yy} d_x + \lambda_{yx} d_y, \tag{2.39}$$

where $\lambda_{xy} = \frac{\partial S_x}{\partial y}$ and $\lambda_{yx} = \frac{\partial S_y}{\partial y}$ are the cross-talk sensitivities. We conclude that for the case of a cylinder the orthogonal combination in **equation 2.37** does not hold anymore.

Remember that our goal is to quantify thermal fluctuations. When a cylinder is subject to the thermal kicks from the solution molecules, it exhibits vibrational modes around the straight conformation. The position fluctuations will be in the transverse direction with respect to the long axis of the cylinder. In order to properly quantify this transverse motion of the cylinder, we need to know the detector sensitivity, let us call it Λ, also in the transverse direction. If we assume that we know the location of the cylinder in the plane, which is outlined in detail in section 4.3.2, we are able to calculate the normal direction $\hat{n}$ to the cylinder (section 4.2.6). We can then move the cylinder through the focal spot along the normal direction for a displacement l and calculate both sensitivities from the x channel, y channel:

$$\Lambda_x = \frac{\Delta S_x}{l}, \tag{2.40}$$

$$\Lambda_y = \frac{\Delta S_y}{l}, \tag{2.41}$$

where ΔS_x and ΔS_y are the change in detector response signals. We use the simple difference ΔS_i because in practice the distance $l = 200\,\text{nm}$. If compared to the width of the linear range of a typical response curve (**Fig. 2.8 a**), and note that the cylinder will be at the center of that linear range, it is a fair assumption that the sensitivity is constant over l.

Both channels, when calibrated, will return the same value for fluctuation magnitude. We choose the channel with the larger sensitivity however, in order to minimize the associated error (see **Fig. 4.8**).

For the case that either the normal direction of the cylinder is not known, or no scan across the cylinder in the normal direction was done, we are still able to calibrate our fluctuations signal by using the scans across the cylinder that were done in the x- and y-direction during the fibril finding process (section 4.3.2). We calculate the gradient field for one of the channels and map it onto the cylinder's normal direction using the dot product:

$$\Lambda_x = \vec{\nabla} S_x \cdot \hat{n} = \begin{pmatrix} \frac{\partial S_x}{\partial x} \\ \frac{\partial S_y}{\partial y} \end{pmatrix} \cdot \hat{n} = \left[\left(\frac{\partial S_x}{\partial x} \right)^2 + \left(\frac{\partial S_y}{\partial y} \right)^2 \right]^{\frac{1}{2}} \hat{s} \cdot \hat{n}, \tag{2.42}$$

where $\hat{s}$ is the unit vector of the signal's gradient. The above equation is equivalent for the y-direction, but once again we use the channel with the larger sensitivity to minimize error.

Finally, we can show that both ways of calibrating the measurement of transverse cylinder fluctuations are equivalent and return the same sensitivity:

$$\Lambda_y = \frac{\Delta S_y}{l} = \frac{\partial S_y}{\partial y} \frac{l_y}{l} + \frac{\partial S_y}{\partial x} \frac{l_x}{l} = \vec{\nabla} S_y \begin{pmatrix} l_x \\ l_y \end{pmatrix} \frac{1}{l} = \vec{\nabla} S_y \cdot \hat{n}. \tag{2.43}$$

Chapter 3

Nanoscopic Imaging of Thick Heterogenous Soft-Matter Structures in Aqueous Solutions

In the following sections, we will turn our attention to three-dimensional Thermal Noise Imaging to detail the method, and show results of its application the collagen fibrils and microtubules. The text was adapted and modified from reference [112]. The work was done in collaboration with Tobias Bartsch, Martin Kochanczyk, and Janina Lange. The author performed the experiments which quantified fibril fluctuations and analyzed their data; wrote scripts to show low-pass filtering effects on TNI data of microtubules, and contributed in writing the manuscript.

3.1 Introduction

For decades, resolving the three-dimensional ultrastructure and organization of cells, or soft matter in general, has been limited to electron microscopy, which requires special preparation of samples and is typically not compatible with live-cell observation. However, recently the diffraction barrier has been overcome by super-resolution fluorescence microscopes such as stimulated emission depletion microscopy (STED) [113], photoactivated localization microscopy (PALM) [114] or stochastic optical reconstruction microscopy (STORM) [115], which provide specific molecular contrast on fixed samples in aqueous solution. The focus is now shifting to the observation of dynamics in living cells, and surprising progress has been made, for instance vesicle motion in Drosophila larvae and the uptake of viral particles has recently been resolved by ultrafast STED nanoscopy with $5 - 10\,\mathrm{ms}$ temporal resolution [116]. The resolution in lens-based super-resolution microscopes is limited by the number of photons detected from fluorophores and by the density of the fluorescent labels. For the observation of dynamics, however, the photon rate is the limiting factor, since the precision in localizing a fluorophore depends on the number of photons that can be collected as well as on the motion of the labelled structure, which limits the time available to collect the photons. However, the current discussion in literature concerning the requirements for molecular resolution imaging of live cells or, more generally speaking, of soft-matter structures, does not address the fundamental aspect of thermal motion in soft and porous media. High precision in label localization and consequently high resolution of soft structures can be achieved only with sufficiently short detector integration times. Even for the fastest reported camera integration times of $2\,\mathrm{ms}$ in STORM [117] and $1\,\mathrm{ms}$ in STED [116], a $10\,\mathrm{nm}$ fluorescent particle in water at room temperature will diffuse on average about 0.8 and $0.5\,\mu\mathrm{m}$, respectively. Although one can precisely calculate the center position of the motion-blurred broad spot on the camera, the true position of the particle is not measured with high precision unless it is immobilized on a very rigid structure. This problem is often solved by fixation of the sample by chemical crosslinkers, which increases the sample's rigidity, and by subsequent labelling of the sample with fluorescent antibodies. In this case, fluorescent probes are rigidly coupled to stiff structures, enabling fluorescence-based super-resolution imaging. However, such fixation necessarily prevents the measurement of mechanical properties of the observed matter due to crosslinking and dense antibody loading, and rules out imaging of living cells. In unfixed samples, both immobilized and freely diffusing probe particles are special cases, since most molecules in a living cell are restricted in their motion either by soft fluctuating structures that surround them or by being part of such structures. The resulting complicated three-dimensional thermal motion of objects, including fluorescent labels, reduces the localization precision in super-resolution microscopy. Furthermore, image distortions due to optical inhomogeneities are mostly ignored in super-resolution microscopy or minimized by working with extremely thin samples [118]. Such optical inhomegeneities are known to seriously degrade imaging performance under all but the most ideal conditions [119]. Here we focus on the motion blur that occurs when probes are freely diffusing and/or are bound to rapidly diffusing structures in complex three-dimensional confinements. Fluorescence-based super-resolution methods are unable to precisely localize such rapidly moving probes unless they are confined or slowed down by a viscous medium. We show that rather than limiting precision, thermal motion of such rapidly diffusing probe particles can be used to gain structural information provided that the restriction to fluorescent labels is dropped, and instead highly scattering nanospheres are used, which can be tracked in three dimensions with short integration times and hence with negligible motion blur. We also gain insights into the mechanics of the imaged structures and into their interaction with the probe particle. Equally important, our approach allows studying and correcting for distortions in the local geometries of the imaged structures due to optical inhomogeneities. Our thermal noise imaging method uses a single diffusing nanoparticle to image soft porous nanostructures. The probe's three-dimensional motion reveals the local geometry with a precision of a few nanometers. As a true three-dimensional imaging technique, our method does not directly compete with atomic force microscopy, which is able to achieve atomic resolution but can only image the topology of surfaces well oriented with respect to the probe. The same limitation applies to other novel forms of scanning probe microscopy, for example, surface imaging by cigar-shaped probes held in holographic optical tweezers [120] or near-field scanning optical microscopy (NSOM/SNOM) by light emitting rod-shaped probes [121]. We apply our method to microtubules and to a network of thick and optically dense collagen fibrils and demonstrate how to correct for image distortions caused by light-fibril interaction. Finally, we find that even these thick filaments, which are usually considered to be rigid, fluctuate on a length scale of 10 nm within a frequency band of up to 1 kHz, underlining the need for fast position measurements for reliable imaging of soft nanostructures.

3.2 Materials and Methods

3.2.1 Passivation of Probe Particles

Fluorescent polystyrene microspheres (sun coast yellow, diameter 190 ± 30 nm, Bangs Laboratories, IN, USA) were passivated against adhesion to collagen fibrils by coating with poloxamer 407 (16758, Sigma Aldrich, MO, USA), a block co-polymer consisting of a central hydrophobic block of polypropylene glycol (PPG, 67 repeat units), flanked on each side by a hydrophilic polyethylene glycol block (PEG, 98 repeat units) [122]. Tracer particles were incubated at room temperature at least overnight in a solution of $2\,\mathrm{mg\,ml^{-1}}$ poloxamer 407 in PBS. From this stock solution the particles were further diluted into PBS for each experiment. Poloxamer 407 self assembles as a brush on the surface of the polystyrene beads [122], with the hydrophobic PPG block adhering to the particle, while the hydrophilic PEG blocks form coils pointing radially outwards.

3.2.2 High Bandwidth and High Precision Trapping and Tracking

All data were acquired using a custom-built photonic force microscope (PFM) featuring an ultra-stable optical trap coupled to a three-dimensional, high-precision and high-bandwidth position detector. Our PFM is capable of tracking the position of a 190 nm diameter polystyrene probe particle with a precision of 1.5 nm laterally and 7 nm along the optical axis at a bandwidth of 1 MHz. The beam of a 1064 nm laser (Mephisto 500 mW, Coherent, CA, USA) was expanded and focused through a water immersion objective lens

(UPlanSApo 60 × W, Olympus, Tokyo, Japan), forming an optical trap at its focus. The sample was mounted on a three- dimensional nano-positioning stage (Nano-View/M375HS, Mad City Labs, WI, USA), which allowed its motion relative to the stationary optical trap. Forward scattered light from a trapped probe particle together with unscattered light of the trapping beam was collected by a condenser lens and projected onto a quadrant photodiode (G6849, Hamamatsu Corporation, NJ, USA), where the two waves interfered. The voltage outputs of the diode's quadrants were amplified by custom-built low noise differential amplifiers (SA500, Oeffner MSR, Plankstadt, Germany) and can be related to the x-, y- and z-position of the particle relative to the center of the optical trap [109, 110]. Typical spring constants of the potential confining the tracer particle were $k_x = 1.5\,\mathrm{pN}\,\mu\mathrm{m}^{-1}$, $k_y = 1.0\,\mathrm{pN}\,\mu\mathrm{m}^{-1}$ and $k_z = 0.15\,\mathrm{pN}\,\mu\mathrm{m}^{-1}$. The corresponding autocorrelation times of the tracer particle's diffusion were $\tau_x = 1.1\,\mathrm{ms}$, $\tau_y = 1.7\,\mathrm{ms}$ and $\tau_z = 11\,\mathrm{ms}$.

3.2.3 Background Correction for Probe Position Signal

In absence of optically heterogeneous material, the position of the probe is determined by reading out the interference of light forward scattered by the probe with light of the trapping beam on the PFM's quadrant photodiode. If the probe as well as the collagen fibril are close to the focus, both light scattered by the probe and by the fibril will strike the detector. The output signal therefore no longer correctly reflects the probe's position and must be corrected for the fibril contributions. It can be shown [87, 123] that to first order approximation the total detector signals along the x-, y- and z-directions $S_\alpha(\mathbf{b}_p, \mathbf{b}_f)$, are the sum of the signals on the detector caused by the fibril in absence of the probe $S_{\alpha,\text{fibril}}(\mathbf{b}_f)$, and the signal caused by the particle in absence of the fibril $S_{\alpha,\text{probe}}(\mathbf{b}_p)$ ($\alpha = x, y, z$ and $\mathbf{b}_p$ and $\mathbf{b}_f$ are the position vectors of the particle and fibril with respect to the focus, **Figure 3.7**)

$$S_\alpha(\mathbf{b}_p, \mathbf{b}_f) = S_{\alpha,\text{fibril}}(\mathbf{b}_f) + S_{\alpha,\text{probe}}(\mathbf{b}_p). \tag{3.1}$$

As shown in this work, collagen networks are athermal to good approximation, and we may assume that the positions of the fibrils $\mathbf{b}_f$ and their signals $S_{\alpha,\text{fibril}}(\mathbf{b}_f)$ are constant. The signal S_α, excluding the constant offset, measured at a certain grid position (x_grid, y_grid, z_grid) is hence only a function of the probe's position $\mathbf{b}_p$ and equal to the probe's position signal $S_{\alpha,\text{probe}}(\mathbf{b}_p)$, plus a constant offset determined by the network's structure around the specific grid position at which the data are acquired. If the offsets are known for each grid position, the particle's position can be calculated from the measured signals as

$$S_{\alpha,\text{probe}}(\mathbf{b}_p)|_{(x_\text{grid},y_\text{grid},z_\text{grid})} = S_\alpha(\mathbf{b}_p) - \mathit{Offset}_\alpha|_{(x_\text{grid},y_\text{grid},z_\text{grid})}. \tag{3.2}$$

For all the data shown in this work, we first acquired the total signals $S_\alpha(\mathbf{b}_p)$ at each grid position of interest. Subsequently, we released the probe from the optical trap and revisited all scanned grid positions to acquire 200 ms long time traces of the offset signals $S_{\alpha,\text{fibril}}(\mathbf{b}_f)$, the mean of which give the offsets Offset_α at each grid position. We then computed the particle position signals $S_{\alpha,\text{probe}}(\mathbf{b}_p)$ as explained above. Collagen networks are only approximately athermal and the offset signals $S_{\alpha,\text{fibril}}(\mathbf{b}_f)$ are not truly constant but contain information on the fibril's transversal motion (see main text). The s.d. of $S_{\alpha,\mathrm{fibril}}(\mathbf{b}_f)$ calibrated with the probe position detector's sensitivity yields additional probe position uncertainty of 3, 4 and 9 nm along x, y, and z, respectively, caused by the fibril's fluctuation.

3.2.4 Calibration of the Position Detector

The three-dimensional detector's non-linear response $S_{\alpha,\mathrm{probe}}(\mathbf{b}_p)$ was linearized and calibrated *in situ* as described by Tischer *et al.* [110] (also see section 2.1.8). The linear order coefficient of the resulting polynomial function, relating signal to displacement, is commonly referred to as the detector's sensitivity.

3.2.5 Polymerization of Microtubules

Microtubules were grown by suspending 4 mg of unlabelled tubulin and 0.8 mg of rhodamine labelled tubulin (T240 and T590M, respectively, Cytoskeleton, CO, USA) in 25 ml BRB80 (80 mM PIPES, 1 mM EGTA, 2 mM $MgCl_2$, pH 6.8) supplemented with 1 mM guanosine triphosphate (GTP) and incubating at 37° C for $10 - 30$ min, depending on the desired microtubule length. After polymerization, microtubules were stabilized by resuspension in BRB80 supplemented with 20 μM taxol.

3.2.6 Single Microtubule Assay

Microtubules were spanned in random directions over a holey carbon film (hole width: 7 μm, hole periodicity: 9 μm) on a copper electron microscopy grid (spacing of the copper grid: 127 μm; S 7/2, Quantifoil, Electron Microscopy Sciences, PA, USA). The 20 μm thick copper grid was glued to a glass coverslip using a biochemically inert, solvent-free silicone glue (Elastosil N10, Wacker, Germany). The copper's thickness provides sufficient lift to avoid any hydrodynamic coupling between the glass coverslip and the microtubules or tracer particles. Microtubules must be grafted to the holey carbon film strongly so that both end points (static microtubule) or one end point (fluctuating microtubule) and the tangent of those points are fixed. This was achieved by exposing the grid for 2 s to an oxygen plasma and then coating the holey carbon film by 50 % poly-L-lysine (PLL) in deionized water. PLL has a strong non-specific interaction with microtubules and is commonly used to immobilize them on surfaces [124]. The coverslip with the glued, plasma cleaned grid was then quickly assembled to a sample chamber by adding a metal spacer, and after the next steps, a top coverslip. The carbon film was then immediately coated with 50 μl of PLL solution and incubated for 20 min at room temperature. In typical assays, the PLL solution is allowed to dry on the surface onto which the microtubules are to be adhered. This was not possible here, since the air-liquid interface of the drying PLL solution destroyed the carbon film on the grid by surface tension. Instead, the PLL solution was flushed off the grid with deionized water. At this point the top coverslip was added to the sample chamber. Fluid inside the chamber could be exchanged through small channels in the metal spacer: 200 μl of BRB80 buffer to displace the deionized water, and subsequently 200 μl of microtubules in BRB80 were flushed into the chamber. The microtubules were allowed to adhere to the PLL coated carbon film for several minutes. Unattached microtubules were then removed from the sample chamber by a flush with 200 μl of a solution containing probe particles and an oxygen scavenging system consisting of 50 U ml^{-1} glucose oxidase, 500 U ml^{-1} catalase and 12.5 mM glucose in BRB80 supplemented with 20 μM taxol.

3.2.7 Computing Radial LRO of a Thermal Noise Imaged Microtubule

To test the reproducibility of thermal noise imaging we imaged a double-confined microtubule 33 times in a row $\sim$ 2 μm away from the support. For the fluctuating microtubule, we acquired the data 2.8 μm from the solid support. A probe particle was held in a weak optical trap and was allowed to diffuse around the microtubule, which intersected the trapping volume and was supported on both of its ends. For each measurement, the particle's motion was recorded for 4 s with an electronic bandwidth of 1 MHz and a sampling rate of 100 kHz. Position histograms were calculated from the 400, 000 measured positions. We then projected the three-dimensional position histograms along the microtubule's axis into two- dimensional histograms, and computed the corresponding two-dimensional LROs (see main text and **Fig. 3.3 e,f,g**). Each two-dimensional LRO was fitted with a two-dimensional Gaussian function to find its center. We then computed the radial LRO from each two-dimensional LRO by averaging the data on concentric circles as described by Zhang *et al.* [125]. The LRO has values of positive infinity in the excluded volume. To account for rare events in which the particle visited voxels close to the excluded volume only once (or very few times) values of infinity must be appropriately dealt with during the radial averaging, we empirically chose to set the value of the radial LRO for a certain radius to infinity if at least 30 % of the two-dimensional LRO's values at this radius were equal to infinity. Conversely, our threshold ensures that we only set the radial LRO to a numerical value if the particle could visit the corresponding radial extension at least 70 % of the time. The resulting radial LROs were then averaged and the s.d. of this average was computed for each radial position (**Fig. 3.3 h**).

3.2.8 Preparation of Collagen Networks

Collagen networks were polymerized without fluorescence labels following a procedure established by Mickel *et al.* [126]. In brief, acid-soluble rat-tail tendon collagen (type I, Collagen R, 354236, BD Biosciences, NJ, USA) and bovine-dermis collagen (type I, Collagen G, 354231, BD Biosciences, NJ, USA) were mixed at relative concentrations of 1 : 2. The mixture was then diluted to a total collagen concentration of $2.4\,\mathrm{mg\,ml^{-1}}$ by adding equal parts of $10\times$ DMEM (D2429, Sigma Aldrich, MO, USA) and $0.27\,\mathrm{M}\,\mathrm{NaHCO_3}$. To induce gel polymerization, the pH of the solution was raised to pH 10 using $1\,\mathrm{M}\,\mathrm{NaOH}$. All components were kept on ice during mixing. The mixture was then quickly pipetted into a preassembled sample chamber consisting of a glass coverslip attached by vacuum grease to a metal washer (**Fig. 3.1**), and left to polymerize for > 45 min at 37° C in a 5 % CO_2 atmosphere. Polymerizing the network inside the sample chamber ensures its attachment to the coverslip, which is a prerequisite for a mechanically stable assay. Networks were between 500 μm and 1 mm thick. After polymerization, the gel was gently rinsed with 1 ml of 1 × PBS. Care was taken to never let the network dry out.

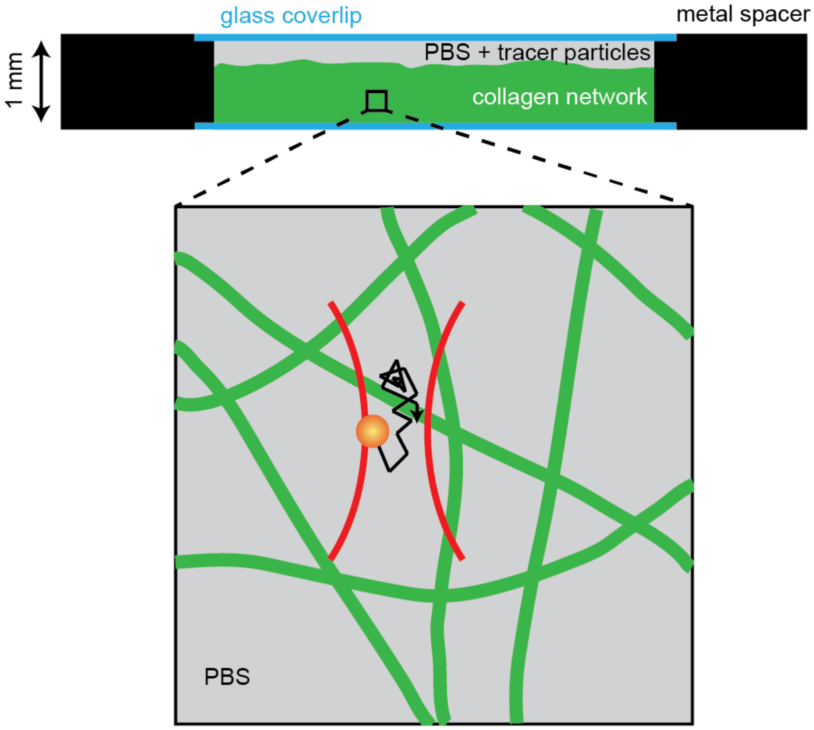

Figure 3.1: Collagen network assay. A collagen network is polymerized inside a sample chamber, after which probe particles in PBS solution are added. Probe particles (orange) in the network (green) can be optically trapped (red beam) and thermal noise images can be acquired.

3.2.9 Collagen Sample Assembly

After polymerization of the collagen network, the sample chamber was closed by attachment of a top coverslip (**Fig. 3.1**). Passivated tracer particles in PBS were flushed into the chamber through channels in the metal spacer. The laminar flow of this flush deposits particles predominantly above, but not inside, the collagen network. The sample was then incubated for at least 2 h to allow the tracer particles to diffuse deep into the gel. At this point, the sample chamber was mounted onto the PFM.

3.2.10 Scanning Strategy for Long-Range Thermal Noise Images

The exploration of an individual trapping volume by the probe particle is driven by thermal forces and is thus limited by diffusion. To ensure that voxels displaced from the center of the trap as far as 150 nm laterally and 450 nm axially were reliably visited by the probe particle the probe's position was tracked for 4 s for each individual trapping volume, which is the integration time of each individual thermal noise image. A volume of approximately $1\,\mu\text{m} \times 1\,\mu\text{m} \times 1\,\mu\text{m}$ can be imaged by acquiring an individual position histogram measurement at each grid point on a $10 \times 10 \times 2$ grid (compare red dots in **Figure 3.5 a** spaced 100 nm laterally and 300 nm axially). Much of the imaged space is empty and its exploration by the particle does not yield information on the network's filaments. As long as no filaments are present at a certain grid point, it is not necessary to acquire a position histogram at its position. Acquiring images only at grid positions close to filaments reduces the total imaging time significantly. Thus, a more sophisticated scanning strategy was implemented to reduce the total acquisition time. To find the positions close to filaments a predefined grid size was chosen and the probe particle was rapidly raster scanned through the sample volume along the grid. At each position, 100 ms long time traces of raw, uncalibrated position signals were acquired. Using the detector's sensitivity, this signal was related to the probe's position (albeit not yet corrected for nonlinearities in the detector response), plus an unknown position offset since the detector has not yet been corrected for the signal offsets introduced by the light scattered by the network. From these time series the s.d., σ_α, were estimated and compared to the reference s.d. of diffusion in an empty trapping volume, given by $\sigma_{\alpha,\mathrm{ref}} = (k_B T/k_\alpha)$, where $\alpha = x, y, z$; k_α are the spring constants of the optical potential, k_B is the Boltzmann constant and T is the temperature. If a filament is present in the trapping volume, the particle can no longer explore the entire volume, and the s.d. of the particle's motion along at least one axis is expected to decrease (**Fig. 3.2**). A decrease of at least one of the s.d. to $\sigma_\alpha < 0.4\,\sigma_{\alpha,\mathrm{ref}}$ was empirically found to be a reliable measure to determine whether fibrils were close to a given grid position. Position histograms were acquired at all grid positions that fulfilled this condition, and at their nearest neighbours. The described strategy is a feedback mechanism on the dwell time at a certain grid position: if no filament is present, the grid position is not revisited for the acquisition of a position histogram, and the full dwell time spent at it is 100 ms. If the probe interacts with a filament, the position histogram is measured by acquiring a

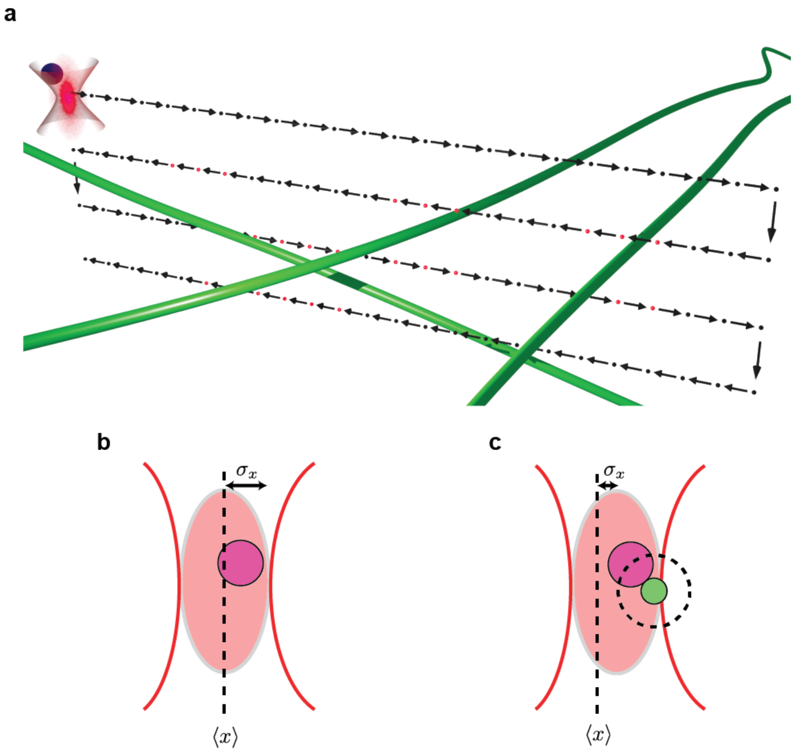

Figure 3.2: Raster scanning strategy with feedback. a - Collagen fibrils are detected by a rapid scan of the trapped particle through the network. The presence of fibrils is detected by the change of the standard deviation of the tracer particle's thermal motion when a fibril is present (compare **b** and **c**). Probe-position histograms are only acquired at positions close to the filaments (red grid points in **a**), eliminating thermal noise imaging of empty space.

4 s long time trace of the particle's diffusion, and the total dwell time at the grid position is 4.1 s. This approach can significantly decrease total acquisition times depending on the amount of empty space in the imaging volume. For example, for the image shown in **Figure 3.10** the total data acquisition time was reduced from 7.3 min to 4.4 min.

3.2.11 Calculation of the Band-Limited Position Noise

The band-limited position noise of the collagen fibril fluctuations (**Fig. 3.10**) was calculated by computing the power spectral density (PSD) of a 1 min long time trace of fibril positions sampled at 100 kHz at an electronic bandwidth of 1 MHz. The PSD was then integrated from 1 Hz to the cutoff frequency as described by Kochanczyk *et al.* [92], yielding the variance of the position noise in the corresponding frequency band. We then computed the band-limited s.d. from this variance. To determine the background noise contributed by out of focus filaments, we positioned the focus of the trapping beam in a pore of the network, $\sim 1.3\,\mu$m from the fibril discussed above, and recorded the beam's signal for 1 min at 100 kHz at an electronic bandwidth of 1 MHz. We calibrated this signal with the fibril's sensitivity and computed its band-limited s.d. The noise floor of the instrument was determined by immobilizing a probe particle onto a glass slide and sampling its position for 1 min at 100 kHz with 1 ms integration time for each data point. The band-limited s.d. of the immobilized bead was computed as explained above, and gives the limit of our instrument's precision.

3.3 Results

3.3.1 Principle of the Experiment

Thermal noise imaging was introduced more than a decade ago [86], but it has until now remained challenging to turn it into a quantitative method for three-dimensional imaging of soft nanostructures. Thermal noise imaging exploits the thermal motion of a nanoparticle as a natural scanner, similar to a protein searching for a binding site. However, in contrast to a freely diffusing protein, the probe particle is confined by an optical trapping potential that forces it to revisit the same volume over and over until its local surroundings have been sufficiently sampled. The laser light that generates the optical trap serves simultaneously as an illumination source for the position detection; hence the position measurement precision is no longer limited by photon statistics. With current detectors, a single position can be measured in three dimensions with a megahertz bandwidth [97, 127]. Within this microsecond integration time the particle can only diffuse a few nanometers (thus avoiding motion blur) and up to a million of positions per second can be measured continuously. This allows dense sampling of the accessible space in which objects are represented by the excluded volume they cause (**Fig. 3.3**).

3.3.2 The Precision of Thermal Noise Imaging

To demonstrate the precision with which structures can be localized using thermal noise imaging, we imaged a 25 nm diameter microtubule supported on both ends by a carbon grid. The tube is formed by protofilaments that are held together by weak lateral interactions. They are the stiffest member of the cytoskeleton; the persistence length is typically a millimeter [32]. For our experiment, as long as they are confined on both ends and are no longer than a few micrometers, we can consider them as rigid rods with a well-defined diameter. In a typical thermal noise imaging experiment, the probe particle is held by optical tweezers next to a structure of interest and its position is recorded with high bandwidth for multiple seconds. A three-dimensional position histogram is then calculated from the millions of position measurements and displayed as an isosurface (**Fig. 3.3**). Without any object nearby, the particle explores the entire trapping potential and the isosurface has a cigar-like shape, as expected for a three-dimensional harmonic trapping potential [128]. The slice through the histogram shows that positions at the center of the trapping potential are most populated, in agreement with Boltzmann statistics. But when the center of the trapping potential is moved to the microtubule axis,

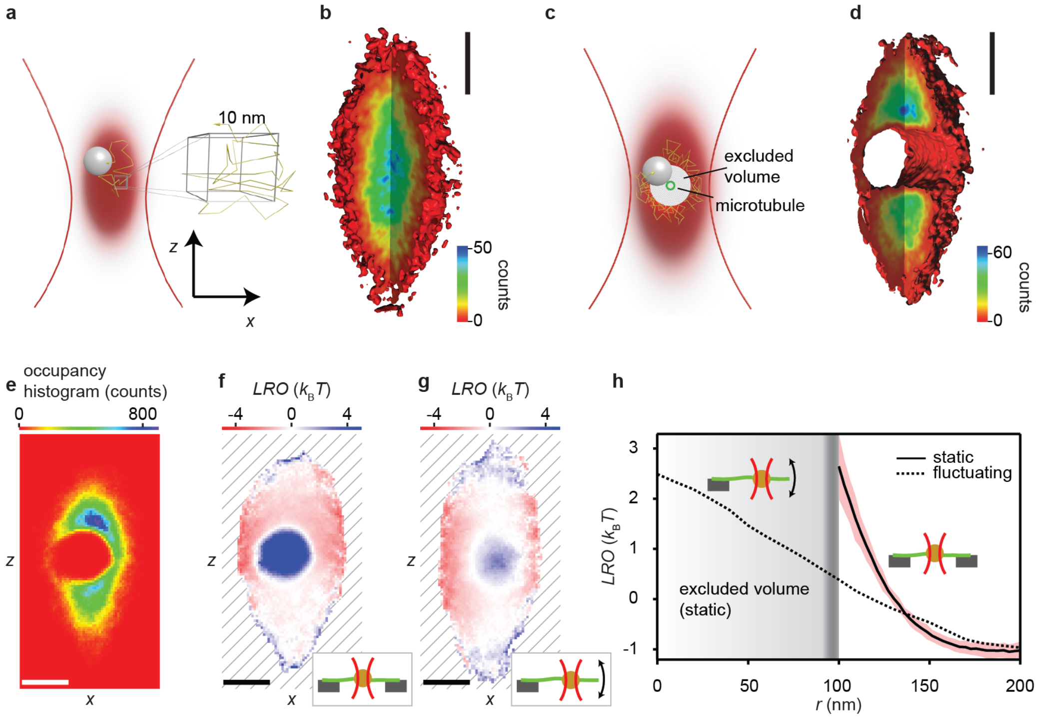

Figure 3.3: *Continued on the following page.*

Figure 3.3: Principle of thermal noise imaging. (**a**) The trapping volume is subdivided into voxels (10 nm side length) to calculate the position histogram. (**b**) Isosurface (red) of equal voxel occupancy. The heat map of the cut-open section indicates the occupancy of each voxel. (**c**) If a filament (green circle) is introduced into the optical trap, parts of the trap become inaccessible. The excluded volume depends on the filament and particle radius. (**d**) Isosurface of equal voxel occupancy for an optical trap intersected by a microtubule confined by rigid supports on both ends (see inset in **f**). Both isosurfaces are drawn for an occupancy of 2 counts. (**e**) Two-dimensional projection of the position histogram along the filament axis. (**f**) Two-dimensional logarithmic relative occupancy (LRO, see main text) calculated from the position histogram shown in **e**. The LRO is a measure for the interaction energy between the probe and the imaged filament. Voxels that the probe can never visit (excluded volume) have an interaction energy of infinity (dark blue). The hatched area indicates the space inaccessible to the particle due to the confinement by the optical trap. The inset indicates our assay: a microtubule (green) is spanned over a carbon grid (grey) and is imaged by a probe particle (orange) confined by weak optical tweezers (red). (**g**) Two-dimensional LRO for a probe particle interacting with a microtubule immobilized on one end, while the other end is free to laterally fluctuate driven by thermal forces (see inset). The LRO shown was acquired $\sim 2.8\,\mu$m from the microtubule's fixed end. The filament's thermal motion allows the probe to visit voxels that were previously inaccessible (**e**,**f**), and the excluded volume disappears. (**h**) The radial profile (see section 3.2.7) of the static microtubule's LRO (solid line) reveals the extent of the excluded volume, which is made up of all voxels that were inaccessible to the diffusion of the probe. The increase in interaction energy between probe and filament for separations shorter than 150 nm is due to an interplay of electrostatic and steric forces and the thermal motion of the filament. The region of uncertainty indicates the standard deviation of 33 independent recordings of the same filament. The radial LRO for the fluctuating microtubule (dashed line) penetrates into the previously excluded volume. Its diminished slope is a result of the much broader spatial probability density of the fluctuating microtubule. Scale bars, 200 nm.

the probe particle has to diffuse around it, leaving a cylinder shaped excluded volume with a diameter that is approximately the sum of the diameter of the probe particle plus the filament. Finding the cylinder axis from a thermal noise image is more involved because the position of the isosurface depends on the position histogram, which in turn not only depends on the geometry of the filament, but also on the shape of the trapping potential and its relative position to the filament. This leads to distortions of the geometry as shown in **Figure 3.3 e**. To correct for the influence of the trapping potential, we introduce the logarithmic relative occupancy (LRO)

$$\mathrm{LRO}(x, y, z) = -\ln \frac{n_{\mathrm{measured}}(x, y, z)}{n_{\mathrm{trap}}(x, y, z)}, \tag{3.3}$$

where n_{measured} is the measured position distribution of the tracer particle and n_{trap} the distribution expected for the trap without an object. The LRO is essentially a measure of how the presence of an object modifies the histogram of a trapped particle. A voxel that is unperturbed by the presence of an object will have a LRO value of zero, excluded volumes will have a value of positive infinity, and voxels with increased probability will have negative values. However, the LRO is more than that: the LRO reflects the interaction potential of the particle with the scanned structure measured in units of the thermal energy $k_B T$ under the condition that the entire volume was sampled long enough so the histogram approaches the equilibrium distribution. **Figure 3.3 f** shows the LRO for the histogram in **Figure 3.3 e**. The presence of the microtubule causes a circular excluded volume (infinite LRO) and forces the particle to explore the voxels around the microtubule with increased probability, resulting in a negative LRO for the filament's surroundings. The projection is now radially symmetric and we find the position of the axis by fitting a Gaussian distribution to the center of the LRO. The resultant uncertainty for the center position by the fit is less than a nanometer. The very small uncertainty is a result of the large number ($n = 400,000$) of local position measurements around the filament. The position of the cylinder axis was determined from 33 histograms recorded at the same position of a microtubule. After correcting for a small instrument drift, the uncertainty of the cylinder axis was 7 nm in the $x-$ and $y-$direction and 15 nm in the $z-$direction, which shows that a filament can be localized with $< 10\,\mathrm{nm}$ uncertainty in the lateral plane. The increased uncertainty along the optical axis was a result of the wider axial trapping potential and the consequently lower number of position measurements near the filament.

3.3.3 Imaging Immobile and Fluctuating Structures

Next, to model a soft, fluctuating structure, we immobilized a microtubule on one of its ends, while leaving its other end free to thermally fluctuate (**Fig. 3.3 g**). As the filament fluctuates transverse to its long axis, the probe can now visit voxels that were previously inaccessible, and the excluded volume disappears. The particle now probes the filament's spatial probability density: the LRO has its maximum at the microtubule's most likely position and slowly decays with increasing radial extension (**Fig. 3.3 h**, dashed line). We analyzed the radial behavior of the immobile double- confined microtubule's LRO as a function of the distance from the filament axis. **Figure 3.3 h** shows the average radial LRO (solid line) calculated around the cylinder axis position for 33 consecutive measurements of the same microtubule at the same position. The red shading represents the s.d. for each point on the curve (see section 3.2.7). The radial LRO represents the interaction potential of microtubule and probe particle; this potential depends on the radius of the microtubule, its thermal fluctuations, the radius of the probe particle, and the thickness of the passivation layer around the particle (see section 3.2.1). From the maximum of the LRO, we find a radius of the excluded volume of 100 ± 15 nm (error defined in 3.2.7). The expected radius of the excluded volume is the sum of the bead radius (95 ± 15 nm), the radius of the microtubule (12.5 nm), and ~ 5 nm thickness of the passivation layer around the particle, which consisted of a poloxamer coating. The resulting radius of 112 nm agrees within the uncertainties with the 100 nm radius from the LRO analysis. The uncertainty in the estimate of the excluded volume is dominated by the uncertainty of the probe radius, but it should be possible to reduce this uncertainty to a few nanometers using an *in situ* measurement method for the particle radius [87].

3.3.4 Imaging Thick Filaments in Heterogeneous Media

The high- bandwidth detection of the probe particle's position by forward scattered laser light relies on the probe's higher index of refraction relative to its environment and scales with the radius of the probe, to the 6^{th}

power for a Rayleigh scatterer.

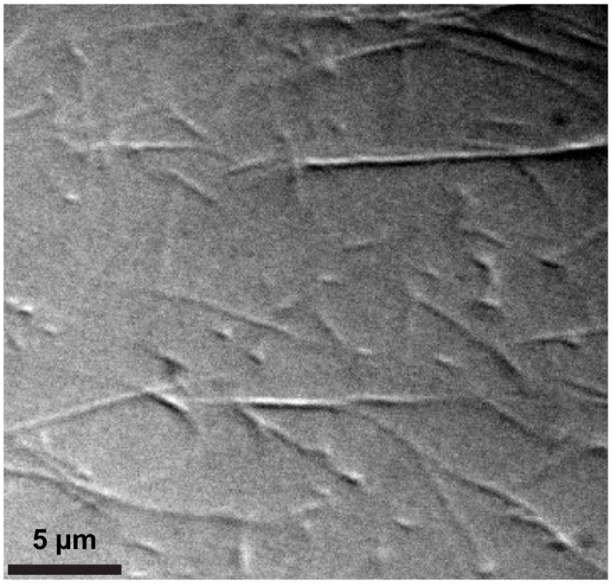

Figure 3.4: Differential-interference contrast image of a collagen network. The large contrast of the fibrils indicates their high optical density compared to the surrounding medium. Fibrils with varying diameters can be seen forming a network with a mesh size of a few micrometers. Experimental conditions were as described in section 3.2.8.

For optically dense filaments (**Fig. 3.4**) with diameters on the order of the diameter of the probe particle, one expects major distortions of the detector signal because the filament scatters light in addition to the light scattered by the probe. A second problem is that thicker filaments cannot be imaged with a single-position histogram of the probe's confined motion because the corresponding excluded volume exceeds the size of the trapping volume and thermal diffusion is not sufficient to drive the probe around the filament. To test whether thermal noise imaging can be used in thick heterogeneous media, we studied collagen I networks as a model system. Collagen I networks under our conditions (see section 3.2.8) are built of fibrils with mesh sizes of $2.6 \pm 0.1\,\mu$m [126].

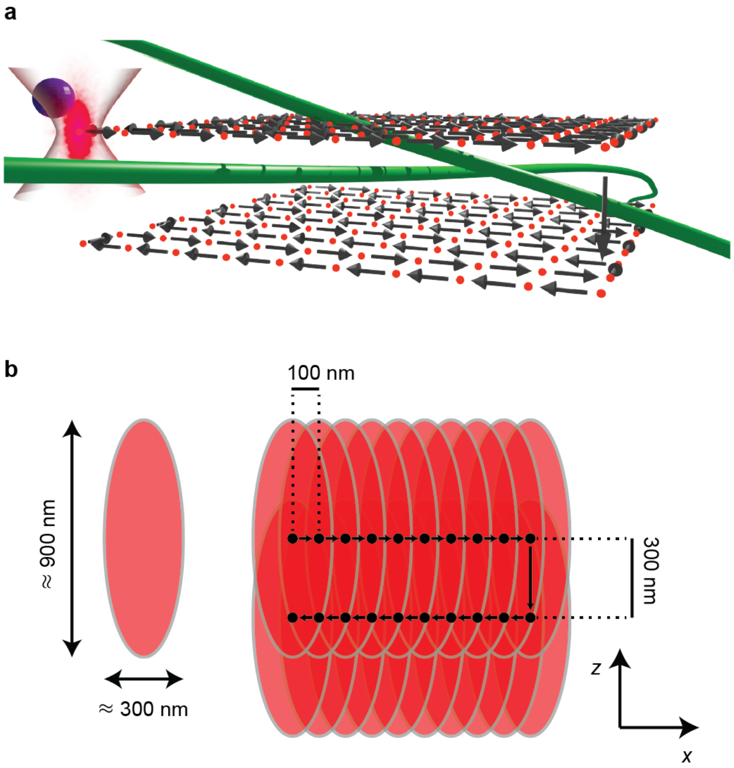

Figure 3.5: Long-range thermal noise imaging in a polymer network. (**a**) Position histograms of the confined particle's motion are acquired centered around positions spaced by 100 nm laterally and 300 nm axially. Two collagen fibrils (green) are drawn to indicate the network. (**b**) Illustration of the overlap of individual occupancy measurements. A position histogram for the entire grid is populated from the individual occupancies by summing up counts of overlapping voxels. This cumulative occupancy, or global thermal noise image, that spans the entire grid is typically displayed by occupancy isosurfaces.

Fibrils have an estimated persistence length of several meters [66] and thus can be considered for our purposes to behave as rigid rods, much like the microtubules in the previous example. Scanning of larger volumes can be achieved by displacing the optical trap along a three-dimensional grid that fills a region of interest while recording a thermal noise image at each grid point (**Fig. 3.5**). Adjacent points are spaced so that their thermal noise images overlap. Local thermal noise images are then combined into a single global position histogram. As expected, however, without correcting for the light scattered by the collagen fibrils, the geometry of the long-range imaged collagen filament is distorted (**Fig. 3.6**). To correct for the light scattered by the fibrils we considered the detected intensity to be the sum of the signal caused by the network alone plus the position signal of the particle in absence of the network (see section 3.2.3 and **Fig. 3.7**). Then if the detector signal caused by fibrils alone is known, the true position of the probe particle can be calculated by subtracting the network signal from the total signal. The network thus gives rise to a time-independent offset signal, which has to be removed from the total signal on the detector. In the following we call this 'offset correction'. The offset signal can be recorded by scanning the focused laser beam through the network without a trapped probe particle. **Figure 3.6 c** shows a thermal noise image after correcting for the network signal. In contrast to the raw thermal noise image (**Fig. 3.6 b**), the filament appears now as a uniform cylinder, indicating that the simple correction algorithm accounts for most of the image distortions. The most challenging situation

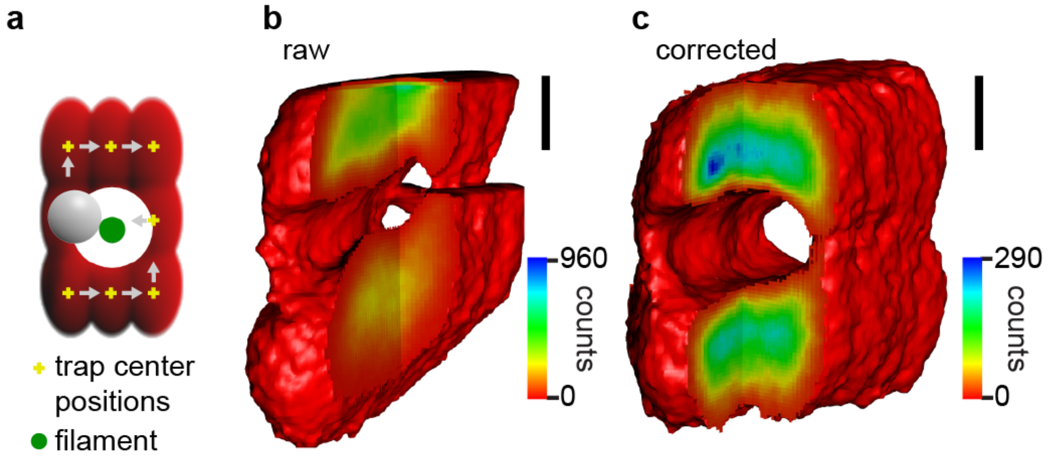

Figure 3.6: Thermal noise imaging of a thick and optically dense filament. (**a**) Since thick filaments cannot be imaged by individual trapping volumes, the center position of the optical trap is instead moved on a grid and individual thermal noise images at each grid position are acquired and subsequently combined to yield a single large image. (**b**) Combined thermal noise image of a collagen fibril that has not yet been corrected for light scattered by the optically dense filament. (**c**) Same data as **b**, but corrected for light scattered by the imaged fibril (see section 3.2.3). Isosurfaces are shown at 10 counts. Scale bars, 200 nm.

for the correction algorithm is the crossing of two or more filaments. **Figure 3.8** shows that such a crossing can be imaged with negligible distortion. The filaments are locally straight and round, indicating that the offset correction works even under these extreme conditions. The filament crossing also allows for a probe particle independent consistency check of the filament diameters. **Figure 3.8 b** shows a slice through the thermal noise image in **Figure 3.8 a** along fibril 1 and perpendicular to fibril 2. The histogram has a small indentation where the probe has to roll around fibril 2. The depth of this indentation

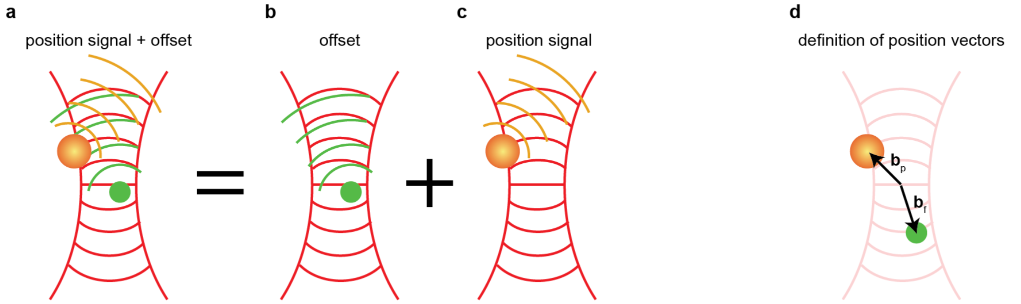

Figure 3.7: Correcting the position signal for network scattered contributions. To first order approximation, the intensity striking the detector (**a**) may be approximated as the sum of the signal caused by the network alone (**b**), plus the position signal of the particle in absence of the network (**c**). a is acquired by reading out the detector while the particle is trapped. b can be independently measured after releasing the particle from the trap. The actual position signal (**c**) can then be computed [87] **d** - Definition of the particle and filament position vectors.

is independent of the probe diameter (**Fig. 3.8 c**), and we estimate that fibril 2 has a diameter of 160 nm. We demonstrate in the previous paragraph that the offset correction results in local geometries with negligible distortion even under difficult conditions. This is only possible if the material above and below the focal plane has a negligible influence on the detector signal. In addition, if any other filaments were located nearby, they would result in additional excluded volumes in the thermal noise image. Thus, we can assume that the detector offset signal originates solely from the imaged fibril. Hence our method opens a new opportunity to study the dynamics of individual collagen fibrils in a network. When the laser is focused on a fibril, any fluctuation measured corresponds to the transverse motion of the filament. The signal can be

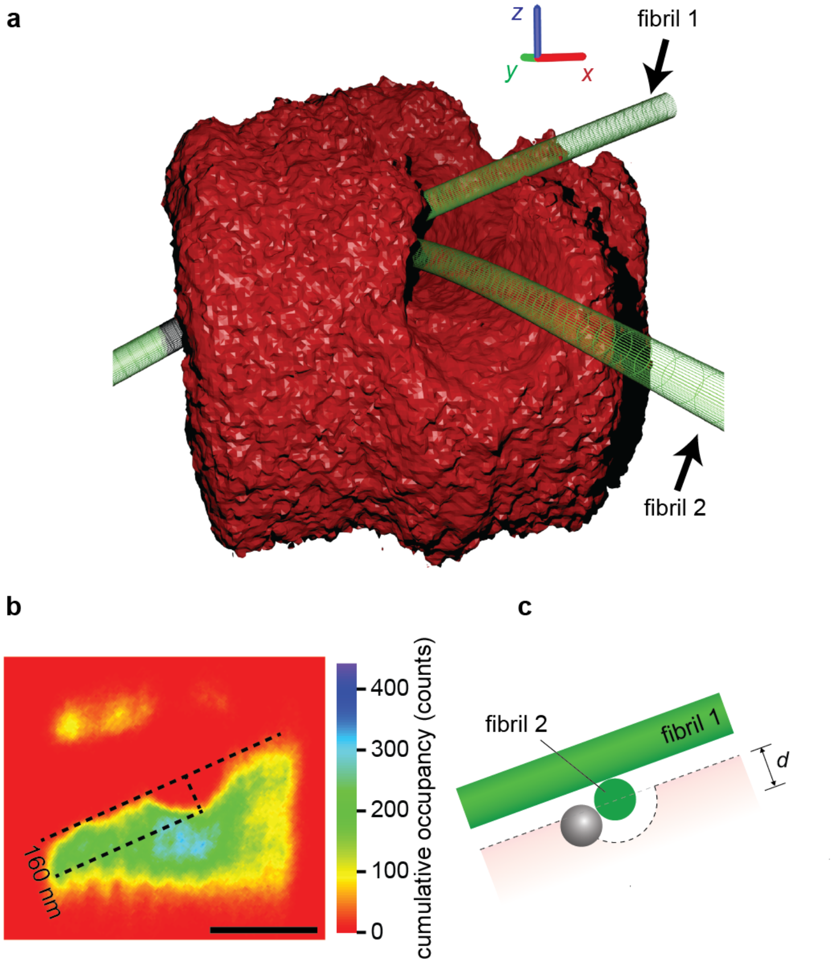

Figure 3.8: Submicroscopic structure of a junction of collagen fibrils. (**a**) Thermal Noise image of a junction of two collagen fibrils, which are sketched in green to guide the eye. Axis cues are 200 nm in length. (**b**) Slice through the cumulative occupancy perpendicular to fibril 2 at the position of fibril 1. The channel formed by fibril 1 is ∼ 160 nm above the channel formed by fibril 2 (Scale bar, 500 nm). This indicates that fibril 2 had a diameter of about 160 nm if the two fibrils lie on top of each other (**c**).

calibrated using the detector response measured in the offset scan (**Fig. 3.9**). **Figure 3.10** shows the s.d. of the transverse fluctuations for the fibril shown

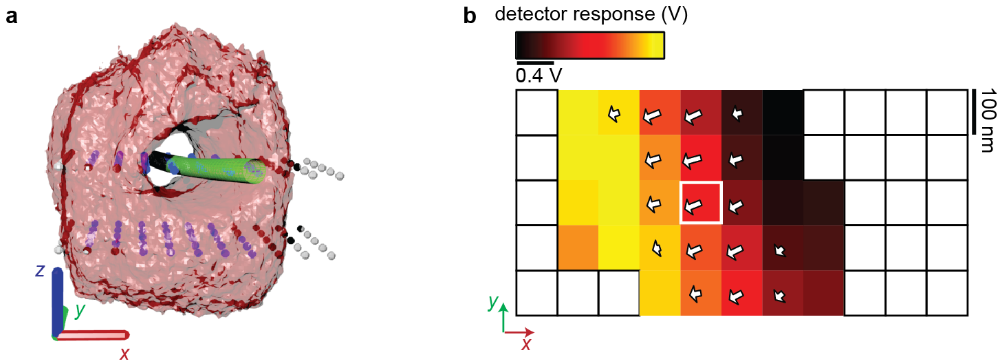

Figure 3.9: Calibration of the position sensor for lateral fibril fluctuations. (**a**) Thermal noise image of a collagen fibril in a network. Spheres mark the grid positions of the scan, spaced as described in **Fig. 3.5**. Data was only acquired at grid positions in close proximity to the collagen fibril (blue spheres). The collagen fibril wireframe is shown to guide the eye. Axis cues are 200 nm in length and the isosurface is plotted at 10 counts. (**b**) Average detector response (squares) along the x-direction in the absence of the probe, for each grid position at which data was acquired on the upper $x-y$ plane of the grid shown in **a**. Isoresponse lines form an angle of approximately 105 degrees with the x-axis. The same angle was independently found for the orientation of the fibril from the thermal noise image in a, a strong indication that the observed response is due to light scattered by the fibril. The gradient of the detector response (arrows) is the detector's sensitivity for displacements of the fibril. The arrow in the white-outlined pixel corresponds to a sensitivity of $4.6\,\mathrm{mV\,nm^{-1}}$ for transversal motion.

in **Figure 3.9**. The main contribution to the signal stems from the frequency interval from 1 Hz to 1 kHz. The slight increase at higher frequencies is caused by a combination of background (green line) and instrument noise (blue line). The s.d. of the fluctuations in the relevant frequency range is clearly above the instrument noise but below 10 nm. The average value of the transverse fibril fluctuations was 7 ± 2 nm for N random positions along fibrils in the network ($N = 11$). This value is interesting for several reasons: it justifies the assumption we made for our offset correction, namely that the fibrils are rigid and do not significantly contribute to the fluctuations of the signal (see section 3.2.3). Further, it is the first quantitative measurement of transverse filament fluctuations for fibrils in a collagen network *in vitro*. This result supports the long-standing assumption that collagen networks are athermal, that is their transverse fluctuations are negligible for the elastic response of the network. In contrast, the mechanical response of actin filament networks is dominated by transverse thermal fluctuations [78]. Finally, this result underlines that even very rigid filaments confined in a network show transverse fluctuations on the order of 10 nm, which can be detected only with high precision and high-bandwidth methods.

3.4 Discussion

We have demonstrated that thermal noise imaging can yield quantitative nanoscale images of soft-matter structures, and we have used the technique to quantify the dynamics of single fibrils in a network. Our method achieves a resolution better than 10 nm in localizing the axis of filaments, and an offset correction makes possible the determination of local geometry even in heterogeneous media. Our probe particles are larger than fluorescent probes and are not specifically attached to a target, but we gain bandwidth and precision,

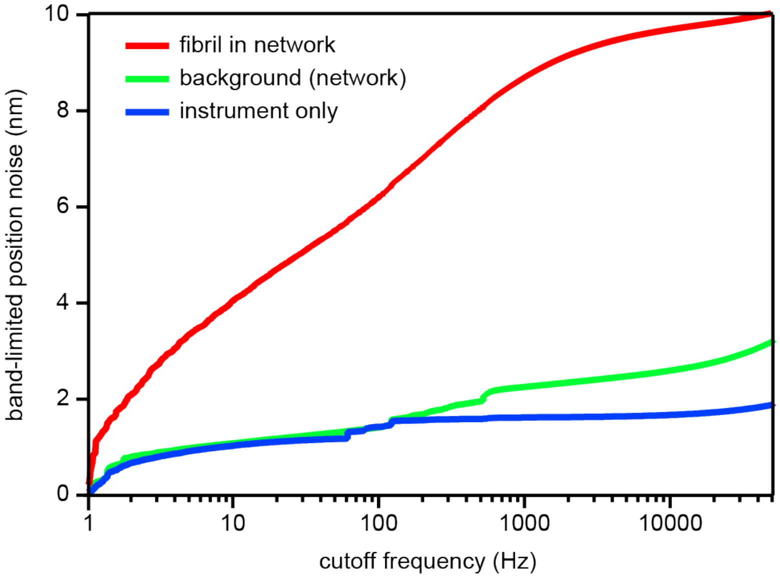

Figure 3.10: Magnitude of lateral fluctuations of a collagen fibril in a network. Most of the power of the fibril's lateral fluctuations is distributed over the acoustic frequency regime; the curve plateaus at high frequencies, as expected (red curve). The motion of the fibril can be easily separated from the background noise caused by the out-of-focus rest of the network (green curve) and from position noise of the instrument (blue curve). The position fluctuations were recorded with a sampling rate of 100 kHz at 1 MHz electronic bandwidth.

which are essential when investigating soft fluctuating structures. Because thermal noise imaging is not limited by labelling density or photobleaching, higher resolution can be achieved simply by recording more probe positions while confining the probe's diffusion to the same trapping volume. Recently, it has been shown that integrating fluorescent probes into intracellular biopolymer networks can change the adhesion dynamics of cells [129], and may alter the force-induced rearrangement dynamics of their cytoskeletons [130]. In contrast to fluorescence-based super-resolution techniques, thermal noise imaging avoids such labels, reducing the risk that the structure, mechanics and dynamics of the imaged soft matter are altered. Probe particles for thermal noise imaging have to be added to the sample before imaging. This is also true for fluorescence microscopy, unless genetically expressed fluorescence labels are used. As with fluorescent probes, our probe particles can only reach volumes accessible by diffusion. Improvements in thermal noise imaging may narrow the gap in size between fluorescent probes and probe particles. The resolution in thermal noise imaging depends on the bin width (typically 10 nm), the number of points in the position histogram (here $400,000$), and the softness of the interaction potential between probe and structure. The probe's radius sets the smallest feature size that can be imaged (**Fig. 3.11**). Reducing the diameter of the probe particle (here 190 nm) would increase both the spatial resolution and the imaging speed; however, smaller probe particles generate a smaller position signal, increase the relative background signal from other structures, and have a weaker trapping potential. The latter is required to force the probe particle to revisit the same volume repeatedly until it is sufficiently sampled. Small metallic nanoparticles have approximately sevenfold the trapping efficiency of equally sized polystyrene beads [131] and feature an order of magnitude higher scattering cross-section [132]. Metallic particles as small as 10 nm have been stably trapped and tracked in a near-aberration free beam [131]. Small silicon particles feature trap stiffnesses comparable to metallic particles without the associated heating of the surrounding fluid and could

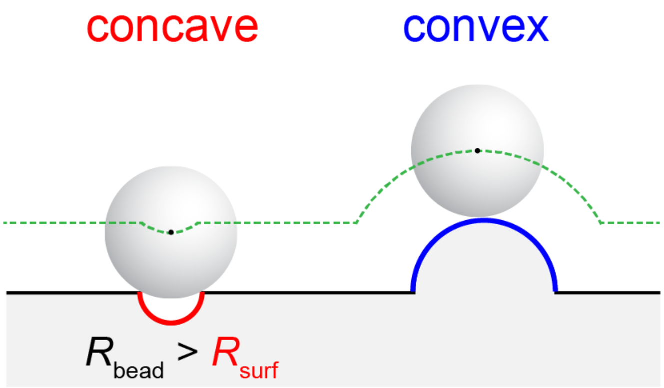

Figure 3.11: Thermal noise imaging of concave and convex features. Concave features can only be accurately imaged if the probe particle can fully penetrate into the feature, that is concave structures with $R_{\text{surf}} > R_{\text{bead}}$ can be imaged without loss of information. No such restriction exists for convex features.

also be a viable candidate for thermal noise imaging [133]. We have begun to evaluate the use of metallic particles as probes in thermal noise imaging and have stably trapped and tracked 100 nm diameter beads in biopolymer networks (data not shown). Despite the optical aberrations, that is, deformations of the wave-fronts of the trapping beam introduced by the network, we believe that the probe diameter can be further reduced to about 50 nm. Collagen, in addition to being the most prominent protein in humans, constitutes an extreme example for a heterogeneous network of thick refractive filaments, which are most difficult to image without distortions. Here we recorded their three-dimensional images with a negligible amount of distortions by recording the offset signal that they cause and correcting the probe's position signal for this offset. In contrast, no such corrections were necessary for thermal noise images of microtubules, because we found the offset signal from the microtubule filament to be negligible compared with the signal caused by the probe. We also expect this to be true for most filament networks with filament thickness in between that of collagen fibrils and microtubules. As filaments get thinner, their effect on the position detection of the probe particle decreases rapidly despite an expected increase in transverse fluctuations. Thus, the results described here should be seen as evidence that thermal noise imaging is able to provide correct data even under extreme conditions (strong optical heterogeneity and thick sample) with most future applications being less demanding. At first glance, the ability of thermal noise imaging to follow dynamic changes in a sample seems to be limited by the time required to record a complete image of at least one trapping volume. This, however, is not the case because a thermal noise image contains quantitative information about structural dynamics faster than the probe position distribution's integration time. LRO profiles change with the fluctuation of the imaged structure (**Fig. 3.3 f-h**) and contain information on its thermal motion with a negligible amount of motion blur. Such LRO profiles can provide detailed information about the mechanics of the imaged structure when an adequate theoretical analysis is applied. In contrast, low-pass filtering distorts the structure's spatial probability distribution as measured by other super- resolution techniques, which results in a flawed extraction of the structure's mechanical properties (**Fig. 3.12**). LRO profiles also reflect the potential energy between filament and probe in units of

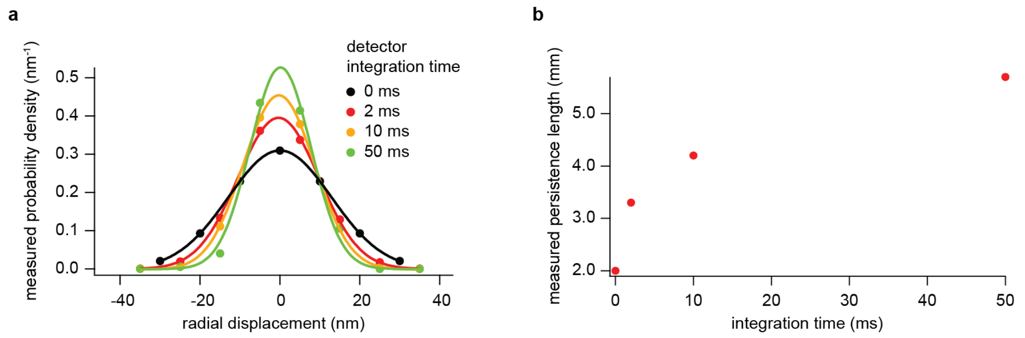

Figure 3.12: Simulation of the lateral fluctuations of a microtubule with different detector integration times. The lateral fluctuations of a 7.5 μm long microtubule (persistence length $l_p = 2\,\text{mm}$) supported on one end and free to fluctuate on the other end were simulated by Brownian Dynamics with 1 μs temporal resolution, taking the first four bending modes of the filament into account. Time traces of radial filament displacements were analyzed at a distance $s = 1\,\mu$m from the rigid support and low-pass filtered with integration times of 2 ms, 10 ms and 50 ms. (**a**) Spatial position histograms of radial displacements for the different extents of low-pass filtering. As the integration time increases the width of the measured distributions shrinks. The black curve shows the analytical Gaussian fluctuation distribution with a variance $var(r) = s^3/(3l_p)$ [64]. (**b**) Typical experiments measure the filament's lateral fluctuations and find its persistence length from the width of the position distribution. The larger the integration time, the smaller the measured width of the distribution and the longer the measured persistence length. In order to extract accurate mechanical properties from such measurements a detector with a short integration time must be used. Microtubules were treated as cantilevered beams whose shape fluctuations decompose into a set of bending modes [134]. We simulated each filament's shape fluctuations by considering its first four bending modes and letting the mode amplitudes undergo random walks in their confining harmonic potentials defined by their stiffness $k_i = \gamma/\tau_i$, where γ is the drag perpendicular to the microtubule and τ_i is the autocorrelation time of the i-th mode [134].

the thermal energy $k_B T$ if the filament can be considered rigid and the volume is visited sufficiently often. For a fluctuating filament the LRO is the potential of mean force felt by the probe. **Figure 3.13** shows low-pass filtered thermal noise images of a microtubule. It illustrates how long integration times lead to wrong interpretation of the imaged structure. The original image was recorded with an integration time of 1 ms. When it is increased to 100 ms, an increase in the radius of the excluded volume is observed (**Fig. 3.14**) and the number of position measurements decreases, accordingly making the isosurfaces noisier. This increase in radius is a result of low-pass filtering of the asymmetric radial position distribution of the probe: the particle cannot diffuse into the filament, so every collision with the filament leads to a displacement of the probe away from the microtubule. The motion-blurred position of the particle during the collisions is hence biased towards positions away from the filament, which in turn leads to an increased excluded volume. When the integration time τ_{int} is so long that the particle has sufficient time to diffuse around the filament, the radius starts to shrink ($\tau_{\text{int}} = 10\,\text{ms}$) and eventually the excluded volume completely disappears ($\tau_{\text{int}} = 40\,\text{ms}$). If our bandwidth were only on the order of tens of hertz, we would conclude that there is no filament and that the particle was located at the center of the optical trap, while it was actually excluded from this position. This effect gets stronger with decreasing particle radius underlining that high detector bandwidth is essential for high precision in localization of diffusing probes. But, even when the probe particle is not freely diffusing, our data show that structures that are considered very rigid fluctuate

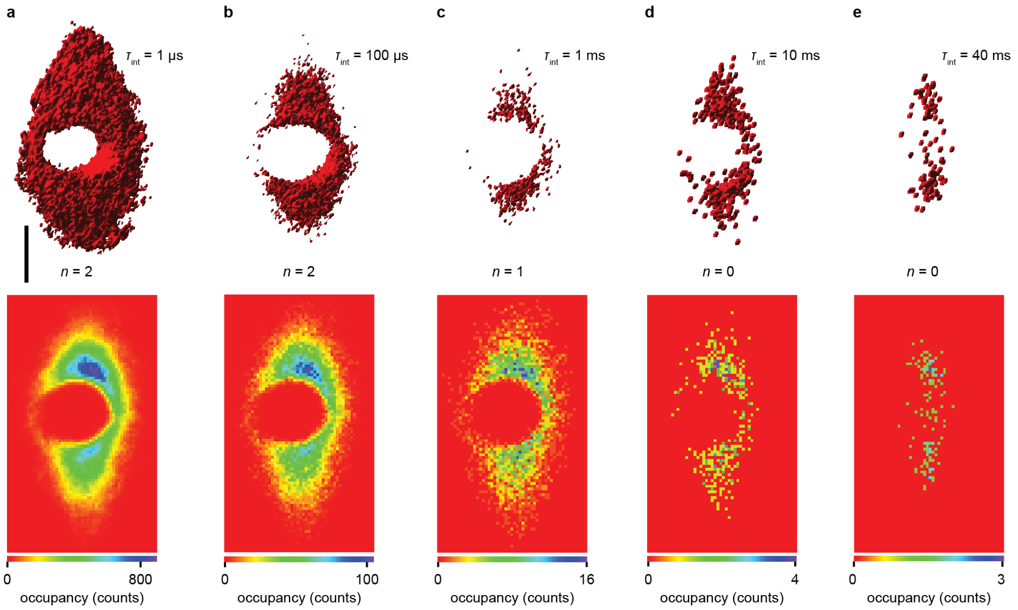

Figure 3.13: Distortion of the imaged local geometry as a result of low-pass filtered position data, here for the example of a thermal noise image of a microtubule. The upper row shows isosurfaces (red) of probe-position histograms, drawn at n counts for different position detector integration times. The data were calculated from the original experimental position data recorded with $1\,\mu$s integration time (shown in panel **a**). The longest integration time corresponds to a typical integration time in STORM or PALM. Below are respective two- dimensional projections of the probe-position histogram along the filament axis, depicting the occupancy as a heat map. (**a**) The original thermal noise image of a microtubule, as shown in **Figure 3.3**, recorded with $1\,\mu$s second integration time. The isosurface for occupancy count of 2 shows a cylindrical excluded volume. (**b**) The integration time is increased to $100\,\mu$s, which leads to a decrease in the number of position measurements. (**c**) An integration time of 1 ms leads to a further decrease in position measurements. The isosurface becomes noisier and the occupancy count had to be reduced to $n = 1$ to still result in a connected surface. (**d**) For the integration time set to 10 ms, the isosurface count had to be lowered to $n = 0$, which now encloses only individual data points in three dimensional space. (**e**) The excluded volume disappears completely at an integration time of 40 ms and one could conclude that the particle visited the middle of the trapping volume, which is not possible due to steric hindrance of the microtubule. Scale bar: 200 nm.

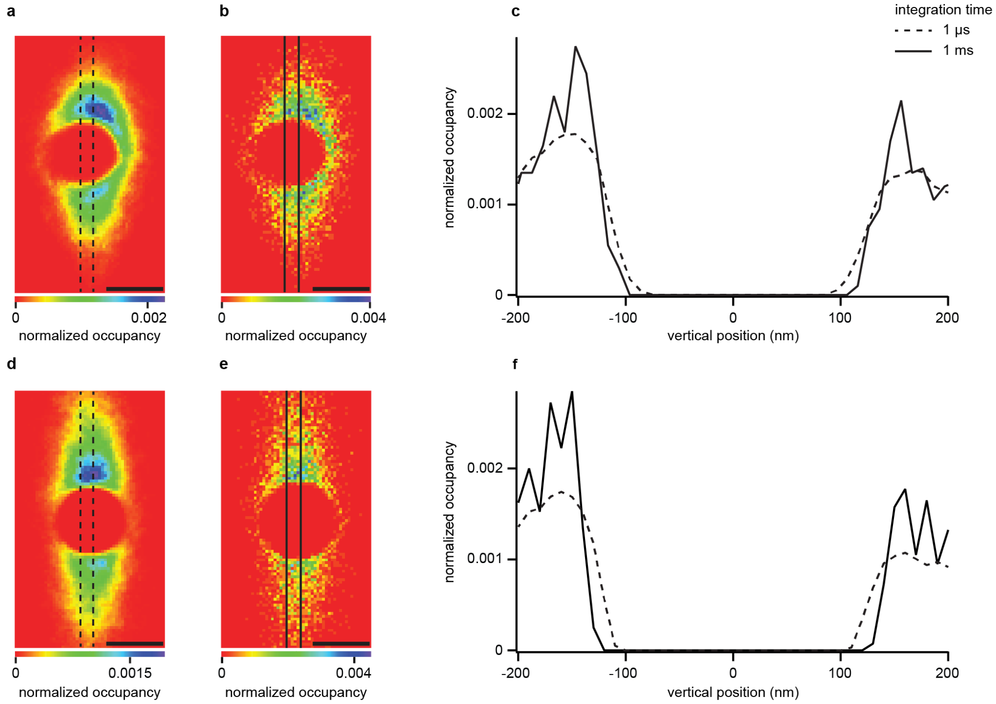

Figure 3.14: Low-pass filtering increases the diameter of excluded volumes in thermal noise imaging. As shown in **Figure 3.13** the local geometry of thermal noise images becomes distorted with increasing integration time. Here we compare the two- dimensional projections of the probe-position histogram along the filament axis normalized with the total position count. (**a**) Experimental realization at full bandwidth of 1 MHz (same data set as **Fig. 3.13 a**). (**b**) Same data as a but low-pass filtered to a bandwidth of 1 kHz (compare **Fig. 3.13 b**). (**c**) Vertical line-profiles in the full bandwidth case (averaged between dashed lines) and reduced bandwidth (averaged between solid lines) show a diameter increase of the excluded volume of approximately 71 nm. (**d**, **e**) Brownian dynamics simulations of the same scenarios as **a** and **b**. (**f**) The simulations show an increase of 60 nm in the diameter of the excluded volume, in good agreement with the experimental result. Scale bars: 200 nm.

on a 10 nm and longer length scale unless they are immobilized on a very rigid substrate such as a microscope slide. So far, thermal noise imaging uses one single probe particle for imaging. Multiple particles in parallel would significantly increase the imaging speed. In principle, this is possible if crosstalk in detecting different particles can be avoided or corrected for. Extension to two probe particles can be achieved by splitting laser polarization and forming two orthogonal optical traps [135]. Simultaneous imaging of more than two particles can be achieved by timeshared optical traps; however, true simultaneous multi-particle imaging requires not only the formation of multiple optical traps but also independent three-dimensional, high-resolution, and high-bandwidth detection that is currently achieved only for up to two probe particles. Both super-resolution microscopy techniques and thermal noise imaging aim at determining the position of an object relative to other structures with nanometer precision, whereas thermal noise imaging provides a wealth of additional information. The measured probability distribution reports on the size and flexibility of structures and on the interaction potential between particle and scanned surface. Forces transmitted through biopolymer networks change the lateral fluctuations of individual filaments in the network: filaments under high tension fluctuate less than those under low tension. Hence, by measuring the lateral fluctuations of filaments, thermal noise imaging also reports on the force transmitted through a structure. This information is essential for describing the mechanics of force transmission through networks which can no longer be considered homogenous on the length scale of interest, for example, a cell migrating through a collagen network. So far, forces are calculated from displacements of markers in the network assuming a linear force-displacement relationship, which does not account for the known highly non-linear force response of connective tissue. The non-linear response seems to arise from local non-affine deformations such as fiber buckling, straightening or stretching, which only recently have been taken into account in modelling [81, 136]. The novel type of microscopy described here will enable us to observe such local non-affine deformations and it will allow us to monitor their mechanical consequences with sub-diffraction limited resolution. This is a result of not only our ability to measure the mean position of fluctuating objects but also of being able to measure their fluctuations around the average correctly. In general, thermal noise imaging opens up new possibilities to study the relationship between structure and dynamics of soft matter, including cells, on a length and time scale that so far has not been accessible. In this regard, thermal noise imaging is complementary to current super-resolution microscopies and future instruments might use both imaging modes.

Chapter 4

Resolving Filament Level Mechanics in Collagen Networks using Activity Microscopy

In the following sections, we will introduce Activity Microscopy for the first time, and show results of its application the collagen fibrils in a network both by itself, and with embedded HeLa cells. The text was adapted and modified from reference [137]. The work was done in collaboration with Tobias Bartsch who contributed to the conception of the experiments, software development, data interpretation and writing of the manuscript. The author performed all experiments, analyzed and interpreted their data, and wrote the manuscript.

4.1 Introduction

Filamentous biopolymer networks fulfill a plethora of mechanical functions both inside and outside of cells. Intracellular networks impart motility and mechanical strength to cells [22], while the networks of the extracellular matrix (ECM) provide integrity to tissues and entire organs [138]. A particular biopolymer network can fulfill many distinct functions, often achieved by the same basic building blocks arranged in different architectures. For example, collagen, the most prominent component of the extracellular matrix, can be arranged into networks of fibers with wildly diverse densities and connectedness, from the loose and soft elastic networks that form the interstitial matrix of the skin to densely packed mineralized fibers in bones [50]. Many physiological processes are regulated by the stiffness of the ECM, such as cellular migration, differentiation or proliferation [6, 59, 62]. The stiffness also plays a role in the progression of skin cancer, as cancerous cells remodel the collagen network of the extracellular matrix to reach blood vessels [63]. Filamentous biopolymer networks are used by engineers as scaffolds to build artificial tissues that mimic true physiological mechanical properties. However, such approaches remain challenging without a better understanding of the complex interplay between individual filament properties, network architecture and mechanical function [139, 140]. Since the typical pore size of these networks is on the same order as the size of cells embedded in the network, cells interact mainly with the individual filaments that surround them, rather than with the global network. To migrate through the extracellular matrix, for example, cells must either squeeze through pores in the network or remodel fibers. Systematic progress in understanding such local cell-matrix interaction is hindered by a lack of techniques that can simultaneously resolve the local network architecture and the interaction forces between cells and filaments. Currently, the three-dimensional architecture of networks and their interaction with cells can be resolved by confocal microscopy, either in fluorescence or reflection mode, or by light sheet microscopy [4]. These imaging modes do not, however, directly measure the mechanics of the interaction. Forces generated by cells can be indirectly quantified from network deformation data by traction-force microscopy (TFM), provided that the mechanical properties of the filaments and their connectedness are known. Recently, Steinwachs *et al.* [136] computed for the first time [141] the forces that breast carcinoma cells apply to biopolymer networks designed to mimic the cells' physiological surroundings. Forces were calculated from network deformations around the cell using a finite-element approach based on a constitutive equation that captures the complexity of the surrounding network. A drawback of this method is that the measurement of network deformations requires knowledge of the force free state, which is achieved by disassembling the force generating filamentous actin network within the cells. The method then assumes that all deformations are elastic, which neglects plastic deformations that have been observed to occur in the ECM [142,143]. There currently exists no method capable of continuously quantifying cell-matrix interactions with single filament resolution and without the assumption of elastic deformations. Here we introduce Activity Microscopy, a method for measuring the precise location and the lateral thermal fluctuations of filaments in fibrous biopolymer networks with subnanometer precision and megahertz bandwidth. The magnitude of the lateral fluctuations is a function of filament tension, bending stiffness, network architecture, and, possibly, fluctuating active forces. Therefore, lateral fluctuations are a direct measure for cell-matrix interactions. For an *in vitro* collagen I network, we localize fibrils with nanometer precision and measure their fluctuations along their contour. We find that tension bearing fibrils with small fluctuations surround pockets of weakly loaded fibrils with larger fluctuations. To demonstrate the sensitivity of Activity Microscopy to changes in fibril stiffness, we observe the reduction of fibril fluctuations after cross-linking with glutaraldehyde. Finally, we seed collagen matrices with HeLa cells and measure the reduction in magnitude and the increase in asymmetry of fluctuations near cells.

4.2 Materials and Methods

4.2.1 High Bandwidth, High Precision Position Detection

Measurements were performed on a custom-built photonic force microscope (PFM) as described in detail by Bartsch *et al.* [97, 112]. In brief, the beam of a 1064 nm laser (Mephisto, 500 mW, Coherent, CA, USA) was expanded and focused through a water immersion objective lens (UPlanSApo, 60 ×W, Olympus, Tokyo, Japan) into the sample. The sample chamber was mounted on a three-dimensional nano-positioning stage (Nano-View/M375HS, Mad City Labs, WI, USA), which allowed for the sample to be moved relative to the stationary optical trap. Forward scattered light from a collagen fibril, together with unscattered light of the laser beam was collected by a condenser lens and projected onto a quadrant photodiode (G6849, Hamamatsu Corporation, NJ, USA), where the two waves interfered. The differential signal from the QPD were amplified by custom-built low noise differential amplifiers (SA500, Oeffner MSR, Plankstadt, Germany). This detection scheme has a megahertz electronic bandwidth.

4.2.2 In vitro Collagen I Networks - Polymerization Protocol I

Collagen networks were prepared and polymerized *in vitro* as described in Bartsch *et al.* [112]. In brief, acid-soluble rat-tail tendon collagen (Collagen I, rat tail, 354236, Corning, NY, USA) and bovine-dermis collagen (Collagen I, bovine, 354231, Corning, NY, USA) were mixed at relative concentrations of 1:2. The mixture was then diluted to a total collagen concentration of $2.4\,\mathrm{mg\,ml^{-1}}$ by adding equal parts of $10\times$ DMEM (D2429, Sigma Aldrich, MO, USA) and $0.27\,\mathrm{M\,NaHCO_3}$. To induce gel polymerization, the pH 10 of the solution was raised to pH using $1\,M$ NaOH. All components were kept on ice during mixing.

The mixture was then quickly pipetted into a preassembled sample chamber consisting of a glass coverslip attached by vacuum grease to a metal sample chamber (**Fig. 4.1**) and left to polymerize for $\sim 1\,\mathrm{h}$ at $37^\circ\,\mathrm{C}$ in a humidity-controlled incubator with $5\,\%\,\mathrm{CO_2}$ atmosphere. Polymerizing the network inside the sample chamber ensures its attachment to the coverslip, which is a prerequisite for a mechanically stable assay. Networks were between $500\,\mu\mathrm{m}$ and $1\,\mathrm{mm}$ thick. After polymerization, the gel was gently rinsed with $1\,ml$ of $1\times$ Phosphate-buffered saline (PBS). Care was taken to never let the network dry out. After polymerization of the collagen network, the sample chamber was closed by attachment of a top coverslip (**Fig. 4.1**) and the chamber was filled with $1\ \times$ PBS before being completely sealed off with

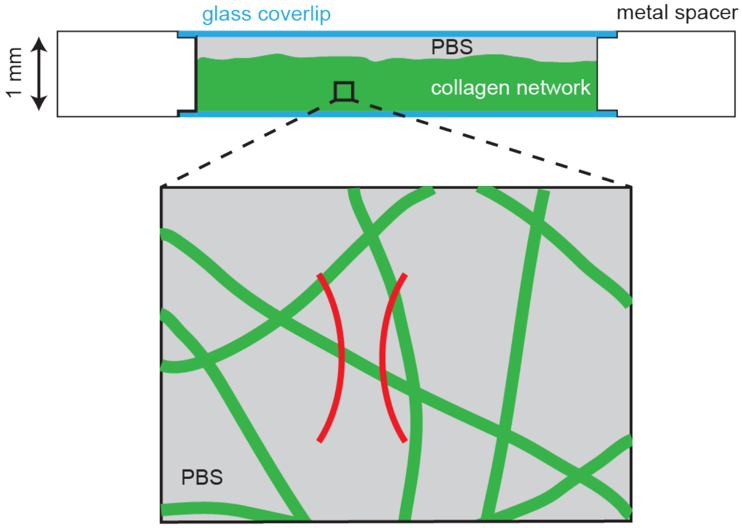

Figure 4.1: Sample chamber design. Cross-section of sample chamber, showing top and bottom coverslip attached to metal sample chamber, with a collagen network in 1 × PBS buffer in-between. Laser focus shown in inset (red). Adapted from Bartsch *et al.* [112].

vacuum grease.

4.2.3 Collagen Network Crosslinking

After polymerization of the collagen network as described above, approximately 100 μl of 4 % v/v glutaraldehyde (GA) in deionized water, was pipetted on top of the collagen and the sample was placed back into the incubator for $\sim$ 2 h. After incubation, the collagen was thoroughly rinsed with 1 × PBS and the sample chamber was assembled and mounted on the PFM.

4.2.4 Cell Culture

HeLa cells were kindly gifted to us by Prof. Aaron Baker (Biomedical Engineering Department, The University of Texas at Austin). HeLa cells were adapted to and cultured in CO_2 independent medium (Gibco, 18045088), which allows for cell culture under atmospheric conditions. The medium was supplemented with $10\,\%$ bovine calf serum (GE, HyClone, SH30072), $4\,\mathrm{mM}$ L-glutamine, $100\,\mathrm{IU\,ml^{-1}}$ penicillin and $100\,\mu\mathrm{g\,ml^{-1}}$ streptomycin at $37°$ C. Cells were passaged every three days. To detach cells from the culture flask, the disassociation agent TrypLE Express Enzyme $1\times$ (ThermoFisher Scientific, 12605036) was used.

4.2.5 Cell Seeding in Collagen Matrix - Polymerization Protocol II

To produce collagen networks with seeded HeLa cells, the collagen network protocol as described above had to be altered in order to incorporate the cell culture medium with a buffer system independent of CO_2 control as the sample is subject to atmospheric conditions while mounted on the PFM. Similarly to the above, acid-soluble rat-tail tendon collagen (Collagen I, rat tail, 354236, Corning, NY, USA) and bovine-dermis collagen (Collagen I, bovine, 354231, Corning, NY, USA) were mixed at relative concentrations of $1:2$ on ice. The mixture was then diluted with $10\,\%$ (vol/vol) $10\times$ PBS and the pH neutralized to $\mathrm{pH} = 7.2-7.4$ with $1\,M$ NaOH and kept on ice. HeLa cells in culture at $80-90\,\%$ confluency were detached from the culture flask using the disassociation agent TrypLE Express Enzyme 1× (ThermoFisher Scientific, 12605036) and spun down at 125 × g for 10 min. The cells were then resuspended in serum-free CO_2 independent medium (Gibco, 18045088) and supplemented with 4 mM L-glutamine at a concentration between $(40 - 80) \times 10^4 \,\text{cells}\,\text{ml}^{-1}$. Finally, the medium containing the cells was added to the neutralized collagen solution on ice at a relative concentration of 20 % (vol/vol) to yield a final cell concentration between $(7-15) \times 10^4 \,\text{cells}\,\text{ml}^{-1}$, and collagen concentration of $2.4 \,\text{mg}\,\text{ml}^{-1}$. The solution was carefully mixed, pipetted into the preassembled sample chamber and placed in a humidity controlled 37° C incubator for 1 h. The network was then topped with $\sim 100\,\mu$l of serum-free CO_2 independent cell media and allowed to incubate overnight.

4.2.6 Calculating the Angle of a Fibril's Axis

Having determined all locations belonging to the fibril axis, we assign an orientation angle value to each individual location, termed filament location in the following. Choosing one filament location after another as the center, we sweep a full circle of given radius r (here: $r = 4$ pixels) in discrete angle steps of $\pi/100$. For every step we calculate an alignment score corresponding to the number of filament locations that are aligned with the straight-line segment connecting $-r$ and r. The alignment score can take a value between 0 and $2r$ pixels. We then find the angle corresponding to the maximum by Gaussian fitting, which corresponds to the local fibril angle at this location. If a filament location is not connected to any others, therefore alone standing, it is discarded.

4.2.7 Calculation of Collagen Fibril Fluctuation, Background Correction and Thresholding

While performing Activity Microscopy measurements a small part of the signal can be attributed to background noise, which arises primarily from four different sources: electronic noise in the amplifier and stage control, laser power fluctuations, mechanical instabilities in the PFM setup, as well as background contributions by parts of the network out of focus. Those noise sources could be characterized individually, but it is simpler to estimate the sum background signal by positioning the laser focus inside of network pores in a collagen sample, far away from fibrils. We determined that on average the s.d. of the background signal is $\overline{\sigma}_{\mathrm{background},x} = 12.56 \pm 0.39\,\mathrm{mV}$ and $\overline{\sigma}_{\mathrm{background},y} = 12.33 \pm 0.92\,\mathrm{mV}$. Assuming all signals to be independent random variables we can subtract the variance of the background signal $\overline{\sigma}^2_{\mathrm{background},x}$ from the variance of the signal measured in volts $\overline{\sigma}^2_{\delta_x}(x,y)$ to get a fibril's true motion:

$$u_x(x,y) = \frac{\sqrt{\sigma^2_{\delta_x}(x,y) - \overline{\sigma}^2_{\mathrm{background},x}}}{\partial\overline{S}_x/\partial x(x,y)}, \tag{4.1}$$

where $\partial\overline{S}_x/\partial x\,(x,y)$ is the local detector sensitivity. An analogous expression is valid for the y-signal. In addition, we chose the smallest acceptable detector sensitivity as $20\,\mathrm{mV}\,\mathrm{pixel}^{-1}$ for pixels with side lengths of 100 nm. Any locations with local sensitivity values below our threshold were deleted. Around all measured scanning areas a two pixel-wide frame was deleted as the spatial derivate for finding fibril locations is ill defined at the edges. For larger scans that required the successive scanning of multiple subsections, a 1 μm overlap between the subsections prevented gaps in the data after deleting pixels at the edges.

4.2.8 Pore Size Distribution for Hot versus Cold Fibrils

An Activity Microscopy image displaying fibril fluctuations is first divided into equally sized sets of “hot” and “cold” fibrils by finding the median of the fluctuation amplitude distribution. We then perform a pore size analysis partially adapted from Mickel *et al.* [126], on three Activity Microscopy images, albeit in two dimensions. In brief, we first convert the image into a simple binary dataset, where all pixels that belong to a fibril are assigned an arbitrarily high value, and all pixel belonging to a network pore are assigned the value zero. We then determine for every pore pixel the largest disk to fit into a given network pore without intersecting any pixels belonging to a fibril. Each pore pixel in the image is then assigned the radius of the largest disk that incorporated said pixel as its value.

4.3 Results

4.3.1 Principle of Activity Microscopy

Activity microscopy aims to visualize the contribution of every filament to a network’s macroscopic mechanical response while simultaneously providing precise information about the network architecture. The filament bending stiffness, stretching and compression forces, and network connectivity affect transverse filament fluctuations, which can either be thermally driven or caused by active elements in the network. We recently demonstrated that thermally driven filament fluctuations can be quantified even in "athermal" collagen I networks [112] for which transverse fluctuations are not expected to contribute to the mechanical response [68]. Here, we develop this method further and introduce two-dimensional Activity Microscopy. We image areas that include many pore diameters and thus provide insight into how individual filaments contribute to the network's overall mechanical response. For Activity Microscopy imaging, a near infrared laser beam is focused into a sample chamber filled with a filament network.

The forward scattered and unscattered laser light is then collected and guided onto a quadrant photo diode (QPD) (**Fig. 4.2 a**). This detection scheme is commonly used in optical trapping experiments [109,144]. The QPD outputs two signals, which are calculated from the voltage differences between the quadrants, $S_x = (S_I + S_{III}) - (S_{II} + S_{IV})$ and $S_y = (S_I + S_{II}) - (S_{III} + S_{IV})$ (**Fig. 4.2 a,b**). In optical trapping experiments, S_x and S_y can be directly related to the x- and y-position of a trapped particle. [1]

However, in the case of filaments, the signals are not independent but depend on the orientation of the filament relative to the QPD (**Fig. 4.3**). For two-dimensional imaging, a plane of interest is selected (**Fig. 4.2 c**) and raster

---

[1] The signal along the optical axis S_z is ignored here, as it is not relevant for two-dimensional Activity Microscopy.

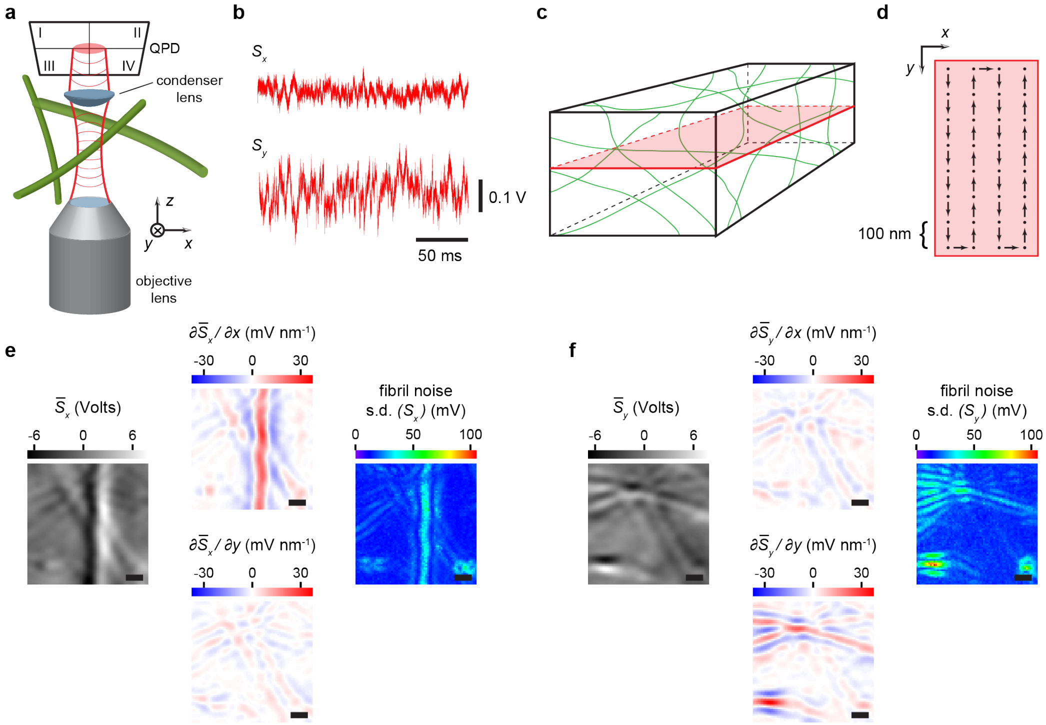

Figure 4.2: Activity Microscopy. (**a**) A near infrared laser beam is focused into the sample filled with a collagen I *in vitro* network (green: fibrils). The forward scattered light from a fibril is collected by a condenser lens and guided onto a quadrant-photo diode (QPD) where it interferes with the unscattered portion of the laser beam. A time series of lateral voltage signals $S_x = (S_I + S_{III}) - (S_{II} + S_{IV})$ and $S_y = (S_I + S_{II}) - (S_{III} + S_{IV})$, recorded at one position are shown in **b**. (**c**, **d**) For imaging, a plane of interest in the sample is selected and scanned line by line while recording time series at each position (black dots). The mean detector signal $\overline{S}_x$ is shown in the left panel of **e**. To find the fibrils' axes, the spatial derivatives $\partial\overline{S}_x/\partial x$ and $\partial\overline{S}_x/\partial y$ are calculated, termed detector sensitivity (middle panel). The raw transverse fibril noise is calculated from the time series of S_x and displayed as the standard deviation (s.d.) (right panel). **f** shows the averaged detector signal, derivatives and transverse fibril noise for the y-signal, which has its maximal sensitivity for fibrils oriented along the horizontal axis. Scale bars in **e** and **f** are 1 μm. The collagen network was polymerized according to protocol I (see section 4.2.2). Distance between scanning lines and dots in d is 100 nm. Time series at each location in **e** and **f** is 100 ms long.

scanned by translating the sample in steps (**Fig. 4.2 d**), which are chosen to be smaller than the diffraction limited spot diameter. **Figure 4.2 e** and **f** show the average detector signals, the calculated detector sensitivities and the raw noise signal for the example of an *in vitro* collagen I network. A total area of 7 μm $\times$ 7 μm was scanned with a step width of 100 nm. At each point, a time series of 100 ms was recorded at 100 kS s^{-1}. The left panel in **Figure 4.2 e** shows the averaged detector signal $\overline{S}_x$ along the x-axis from which the detector sensitivities $\partial\overline{S}_x/\partial x$ and $\partial\overline{S}_x/\partial y$ (mid panels) are calculated. Clearly, S_x is mainly sensitive to fibrils that are oriented vertically. The highest sensitivity is measured when the laser beam is centered on the fibril (broad vertical line).

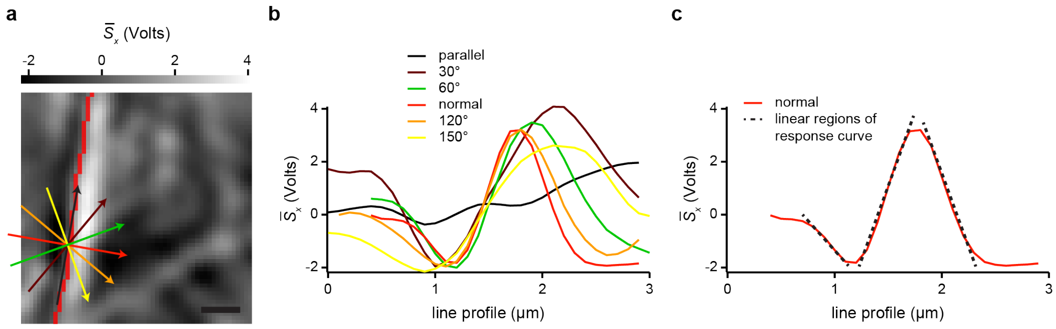

Figure 4.3: Detector response to a collagen fibril. (**a**) The mean of the raw voltage signal $\overline{S}_x$ for each position (pixel) in a 6 μm $\times$ 6 μm scan through a collagen I network. Pixels marked in red show the axis of one prominent fibril. The colored lines indicate the direction of the following line profiles: parallel direction (black), thirty degrees w.r.t. the fibril (brown), sixty degrees w.r.t the fibril (green), normal direction (red), one hundred and twenty degrees w.r.t. the fibril (orange), and one hundred and fifty degrees w.r.t. the fibril (yellow). The line profiles are plotted in **b**. (**c**) The perpendicular (w.r.t. the fibril) line profile is shown again. Three linear regions that are found in the detector response are indicated by black dashed lines.

This is expected from the detector response to a fibril, which has its maximal slope at the midpoint of the fibril (**Fig. 4.3**). Thus, the location of maximal sensitivity can in turn be used to determine the precise position of the fibril axis. The fibril's transverse position fluctuations can be calculated from the standard deviation s.d. of the times series of S_x and S_y. Since the highest detector sensitivity leads to the largest raw position noise for a given filament fluctuation amplitude, the maxima in the raw noise image (right panel) also indicate the positions along the fibril axis. The fibril noise images in **Figure 4.2 e** and **f** show "ghost filaments" that run next to the main fibril axis. They result from the characteristic detector response of a fibril. Besides the maximal detector sensitivity when the fibril is directly in focus, the detector also has significant sensitivities to the left and right of the center (**Fig. 4.3 c**, dashed lines). These regions of the detector response with negative slope are clearly visible in the detector sensitivity panels as blue lines, i.e. negative sensitivities, that follow the fibril on either side. Since negative sensitivities can be easily identified, this detection artifact can be corrected for by removing signals originating from locations in the sample with negative sensitivities (**Fig. 4.4**).

4.3.2 Finding Filament Axes and Orientations

Point-by-point Activity Microscopy imaging is time consuming because at each point in the region of interest a time series must be recorded for a sufficiently long time to characterize the local fluctuations of the filaments.

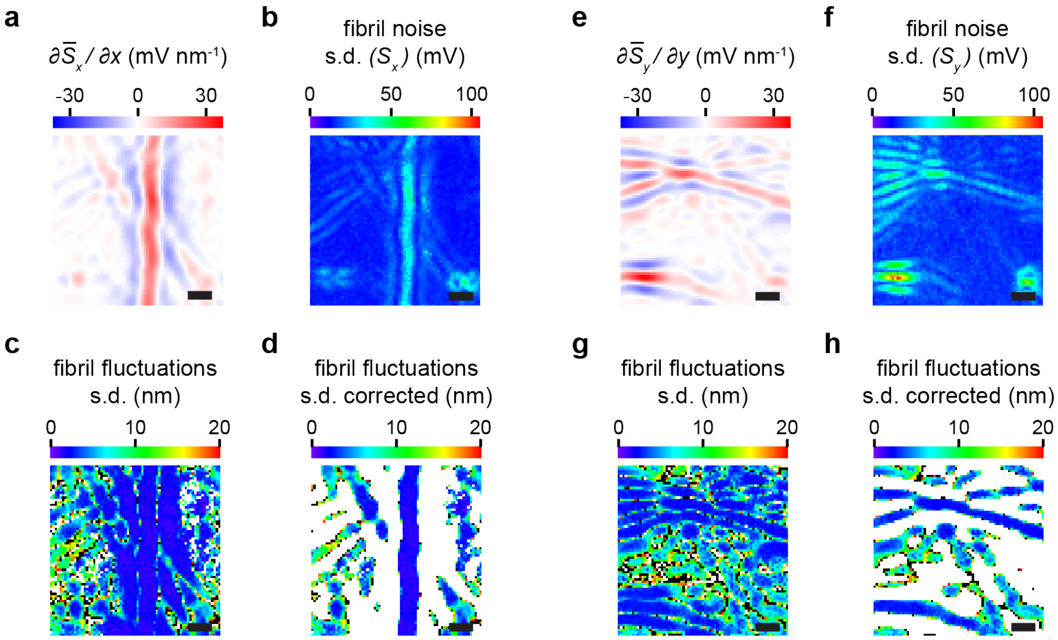

Figure 4.4: Correction for regions of negative sensitivities. a and **b** show the local detector sensitivities and uncalibrated fibril noise respectively, for the x-signal of a $7\,\mu$m $\times$ $7\,\mu$m Activity Microscopy scan through a collagen I network. The regions of negative sensitivities (blue areas in **a**) show up as ghost filaments in the calibrated fibril fluctuations (**c**) and can be corrected for (**d**) as described in section 4.2.7. **e** - **h** show the detector sensitivities and fibril noise, corrected and uncorrected fibril fluctuations for the y-signal. Scale bars are $1\,\mu$m.

Given an approximate pore size of $2 - 3\,\mu$m for the collagen concentration used here ($2.4\,\text{mg}\,\text{ml}^{-1}$) [126], most of the scanning time is spent inside pores. Additionally, fibril fluctuation amplitudes can only change along the contour of a filament, but not transversally to the contour.

Thus, data from the same position along the contour of the filament, but at different positions transversal to its axis, yield the same fluctuation am-

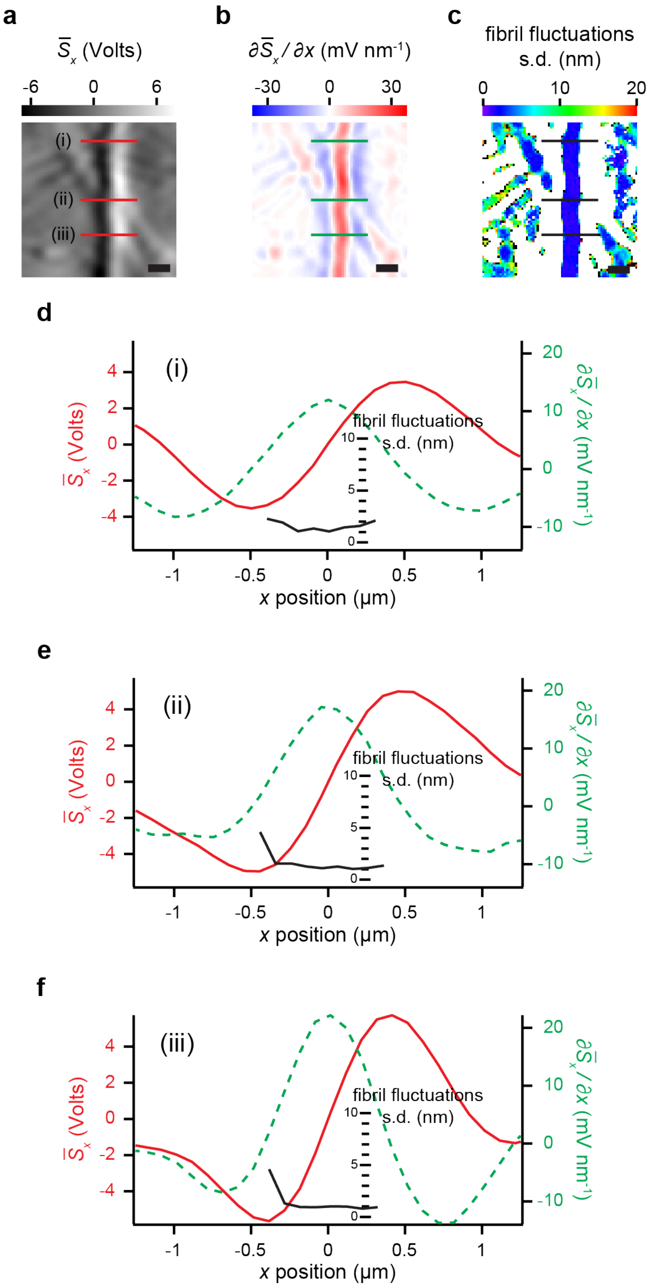

Figure 4.5: *Continued on the following page.*

Figure 4.5: Fluctuations measured within linear detector range are constant across filament width. **a**, **b**, and **c** show the mean detector signal $\overline{S}_x$, its spatial derivative $\partial\overline{S}_x/\partial x$, and the calibrated fibril fluctuations for regions of positive detector sensitivity, respectively. Three different lines profiles numbered (i), (ii), and (iii) across a prominent fibril are plotted in **d**, **e**, and **f** respectively. The detector signal is shown in red, its spatial derivative in green, and the calibrated fibril fluctuations in black. Across the linear region of the detector the fluctuation amplitudes vary within . Scale bars in **a** - **c** are 1 μm.

plitude as long as the filament remains within the linear range of the detector (**Fig. 4.5**). For characterizing the fluctuation of each fibril in the network, it is therefore sufficient to measure fibril fluctuations only at points along the fibril axis. To implement such an imaging algorithm, the locations and orientations of all fibrils in a network must be known. We achieve this by rapidly pre-scanning the network ("fast scan"), only recording time series sufficiently long to determine the average detector signals $\overline{S}_x$ and $\overline{S}_y$.

Figure 4.6 a and **c** show the results for a time series with a length of 5 ms. There is no obvious degradation in the $\overline{S}_x$ and $\overline{S}_y$ images in comparison to the images shown in **Figure 4.2 e** and **f**. The line profiles of the average detector signals are still smooth (**Fig. 4.6 b**) and the calculated detector sensitivities are essentially noise free (**Fig. 4.6 d,e**). Since the positions of maximal detector sensitivities colocalize with the fibrils' locations, we can use these images to localize the fibrils. To achieve this, horizontal and vertical line profiles of the $\overline{S}_x$ and $\overline{S}_y$ signals, respectively, are extracted and the locations of the maxima determined. In this way, the fibrils' axes are found with nanometer

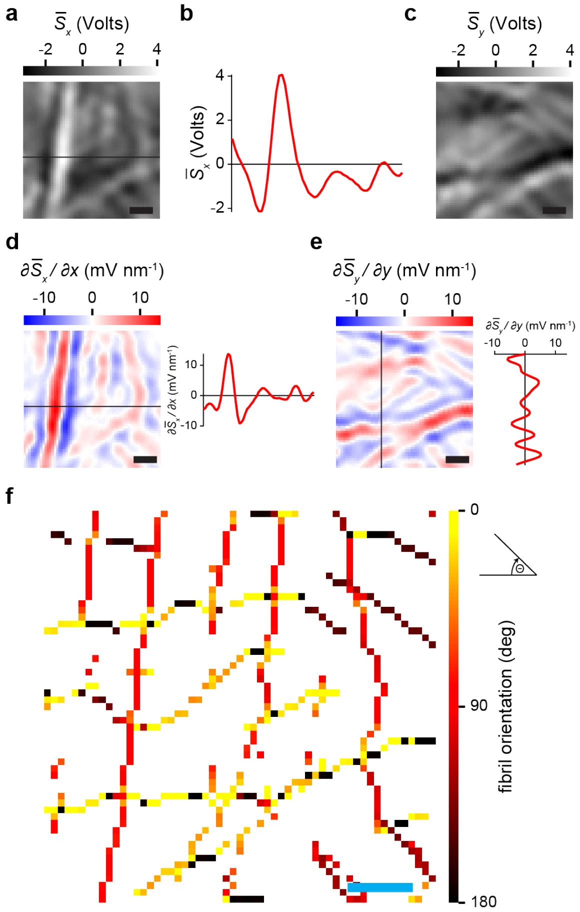

Figure 4.6: Localization of fibrils. Fibrils are located using the maximum sensitivity values either along the x- or y-direction depending on their orientation relative to the detector coordinate axes. A line profile of the mean signal $\overline{S}_x$ (black line in **a**) reveals the detector response to an individual fibril (**b**). (**c**) The mean signal $\overline{S}_y$ from the same scan as in **a**. The detector sensitivities $\partial\overline{S}_x/\partial x$ (**d**) and $\partial\overline{S}_y/\partial y$ (**e**) show maxima at the fibrils' locations (see also representative horizontal and vertical line profiles, respectively). $\partial\overline{S}_x/\partial x$ is used to identify fibrils oriented with an angle $\leq 45°$ w.r.t. the vertical direction, while $\partial\overline{S}_y/\partial y$ serves to find fibrils oriented with an angle $< 45°$ w.r.t. the horizontal direction. The locations of the fibrils are plotted in **f**. The color indicates the fibril orientation w.r.t. the horizontal direction (see section 4.2.6). Scale bars are 1 μm . The collagen network was polymerized according to protocol I (see section 4.2.2).

precision. [2] **Figure 4.6 f** shows the locations of the fibrils identified using this algorithm on a grid with a pixel size of 100 nm × 100 nm. Ghost filaments are excluded because they correspond to minima in the detector sensitivity. The orientation of filaments relative to the detector orientation is then determined (see section 4.2.6) and displayed color-coded for each filament position. This algorithm reliably finds fibril axes locations and orientation in a $5\,\mu$m × $5\,\mu$m image in approximately two minutes.

4.3.3 Long-range Imaging

For visualizing how individual filaments contribute to the overall mechanical response of a network, it is necessary to image areas that are large relative to the pore diameter. This is challenging because slow drift of the sample or instrument will lead to increasing discrepancies between the fibril's positions found by fast scanning, and the locations at which the fluctuations are recorded. To solve this problem, we subdivide the area of interest into smaller tiles of $5\,\mu$m × $5\,\mu$m and perform Activity Microscopy imaging tile by tile, thus avoiding significant relative drifts.

As shown in **Figure 4.7 a**, fibrils can be traced this way over long

---

[2] We chose a time series length of 5 ms to determine the average of detector signals $\overline{S}_x$ and $\overline{S}_y$. We then use the average of multiple locations to find the position of a fibril's axis. The short time interval effectively high-pass filters the time series with a lower frequency cut-off around 400 Hz. We have shown in the past, however, that frequencies below 400 Hz can contribute up to 70 % of the power in a fibril's transversal fluctuations [112]. Therefore, when determining a single fibril's position, we accept an inherent error of < 10 nm. This is not an issue when quantifying fluctuations however, as we show above that the fluctuation amplitude when measured within the linear range of the detector, is the same across the full width of the fibril (**Fig. 4.5**). This region is on the order of $100s$ of nanometers.

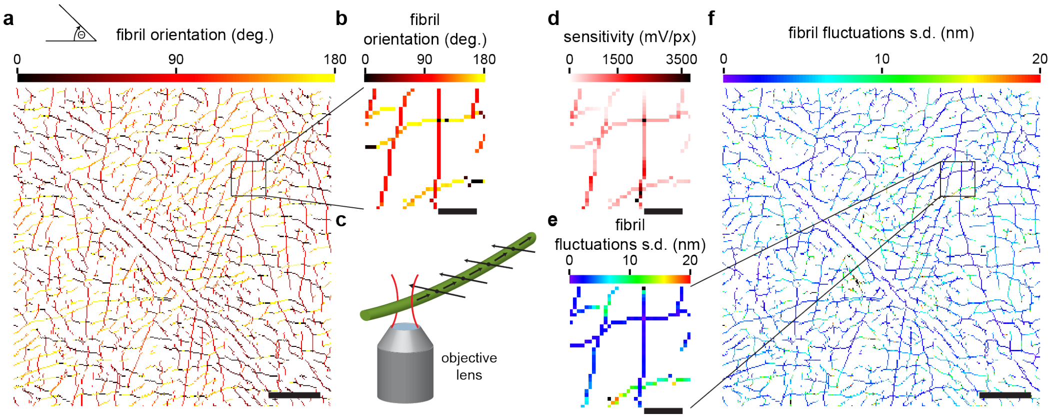

Figure 4.7: Quantitative imaging of fibril fluctuations. The map of fibril locations and orientations (**a**, **b**) are used to record fibril fluctuations only at selected points corresponding to fibrils' axes. In a first step, the detector signal is recalibrated by scanning the laser beam perpendicularly to a fibril axis (**c**). **d** shows the refined detector sensitivities for each fibril position. A 200 ms time series is then recorded, and the raw voltage signals are converted into calibrated transverse fibril fluctuations using the measured detector sensitivity. **e** and **f** show the final Activity Microscopy image. Each fibril position is shown color-coded with the magnitude of its transverse fluctuation. Scale bars are 5 μm in **a** and **f**, 1 μm in **b**, **d**, and **e**. The collagen network was polymerized according to protocol I (see section 4.2.2).

distances without discontinuities. In each tile, a sequence of four steps is performed. The fast scan with dwell time of 5 ms per pixel is recorded and the fibrils' axes and their orientations are determined (**Fig. 4.7 b**). The list of fibril positions is then used to record fluctuation data for 200 ms only directly on the fibrils' axes. To obtain an accurate detector calibration at the time that fluctuation data are recorded, the detector sensitivity is measured at each pixel of interest by scanning the fibril perpendicularly to its axis through the laser beam (**Fig. 4.7 c,d**). The scan is used to calibrate the raw voltage signals which then provide an accurate measure for the transverse fibril fluctuation at a given position on the filament axis (**Fig. 4.7 e,f**). At every position we chose either the x- or y-channel, depending on which one has the greater sensitivity. Both channels will pick up the same fluctuation amplitude except for fibrils that are perfectly aligned with one of the detector axes. This selection of channels minimizes the uncertainty in fluctuation measurements (**Fig. 4.8**).

Figure 4.7 f shows a $30\,\mu\text{m} \times 30\,\mu\text{m}$ Activity Microscopy large scale image of a collagen network, in which the amplitude of the transverse filament fluctuations is color-coded for the range $0 - 20\,\text{nm}$. The distribution of fluctuation amplitudes in the network is heterogeneous: a few fibrils with strongly suppressed fluctuations cross the entire network and in-between are pockets of strongly fluctuating fibrils.

4.3.4 Pore-size Distribution

Activity Microscopy images of collagen networks suggest a heterogeneous distribution of fibril fluctuations. A few fibrils with strongly suppressed fluctuations divide the field of view, while the regions between them are filled with fibrils with large fluctuations. To quantify this observation, we calculate the average pore size distribution for "hot" (strongly fluctuating) and "cold" (weakly fluctuating) fibrils. To calculate the pore size distribution, we adapted a robust method for calculating pore sizes from confocal images of collagen networks developed by Mickel *et al.* [126], which does not rely on spe-

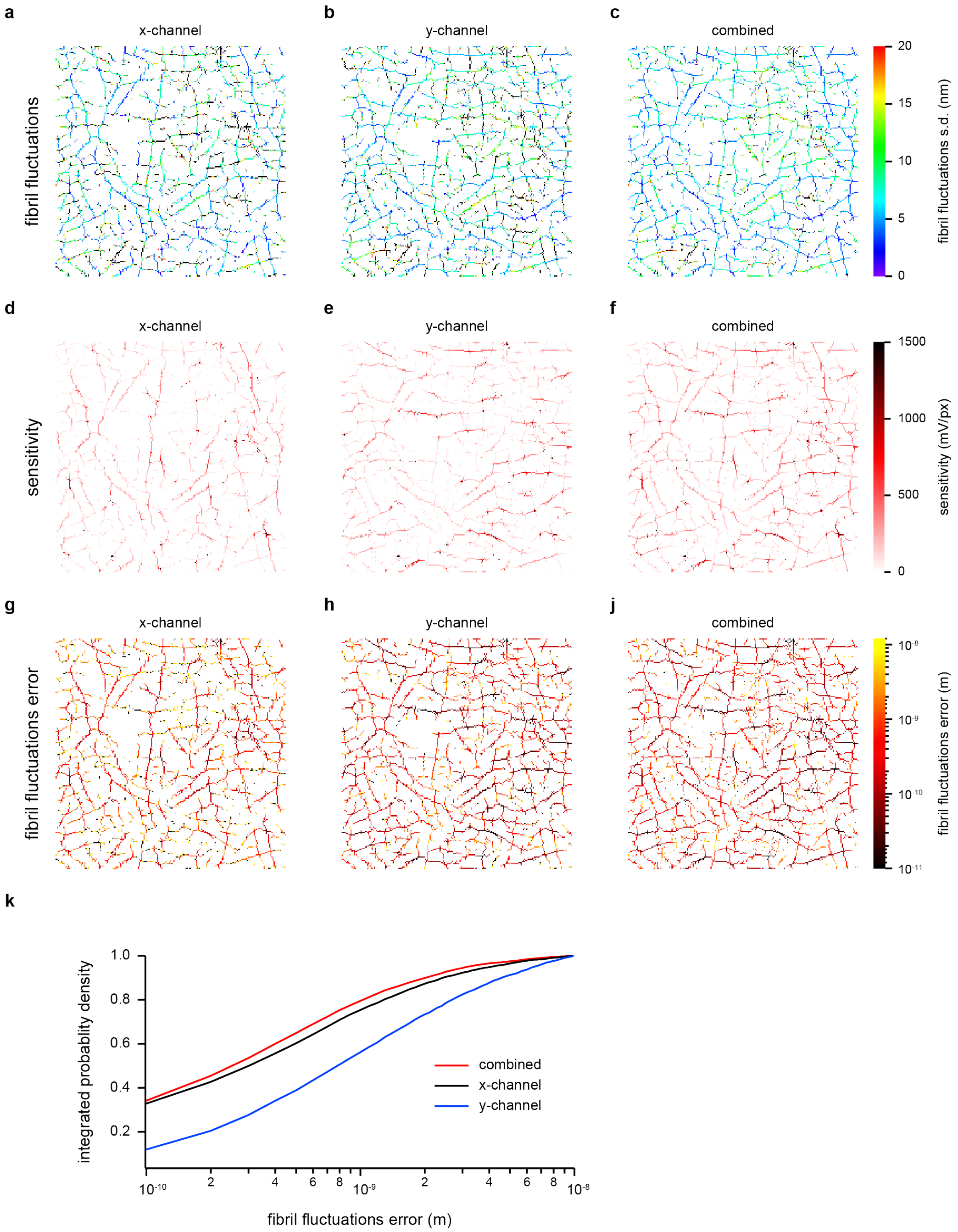

Figure 4.8: *Continued on the following page.*

Figure 4.8: Choosing the channel with the greatest sensitivity minimizes the uncertainty in fluctuation measurements. Activity Microscopy images calculated only from the x-channel (**a**), only from the y-channel (**b**), or choosing the channel with greater sensitivity for each pixel (**c**). **d**, and **e** show the sensitivities as obtained from perpendicular scans across the fibrils, for the x- and y-channel, respectively. The greater sensitivity between the two channels for each pixel is shown in **f**. Both channels pick up the same fluctuation amplitude within error (except for perfectly horizontally or vertically aligned fibrils) (**g**, **h**). Choosing the detector channel with greater sensitivity minimizes the uncertainty in fluctuation measurements (**j**, **k**).

cific assumptions or network models. Fibrils are represented by medial axes instead of their diffraction limited image. In our case, fibrils are represented by one-pixel wide lines corresponding to a width of 100 nm. For each pixel of the fluid phase, the radius of the largest disk that can be fitted into the pore while still including the pixel, is determined. For pixels within the center of a pore, the maximal disk size is given by the contact of the disk with the medial axes that form the pore. Pixels confined by fibrils in corners will have a smaller radius. The pore size distribution for a network can be summarized by a histogram of radii for all pixels of the fluid phase. The goal in our case is to show that cold and hot filaments have different pore sizes.

To achieve this, we divide all fibrils (**Fig. 4.9 a**) into an equal number of cold (blue) and hot (red) filaments based on the cumulative probability of fibril fluctuations (**Fig. 4.9 b**). An equal number of cold and hot fibrils is achieved at a fluctuation threshold of $\sim$ 5 nm. A binary image representing

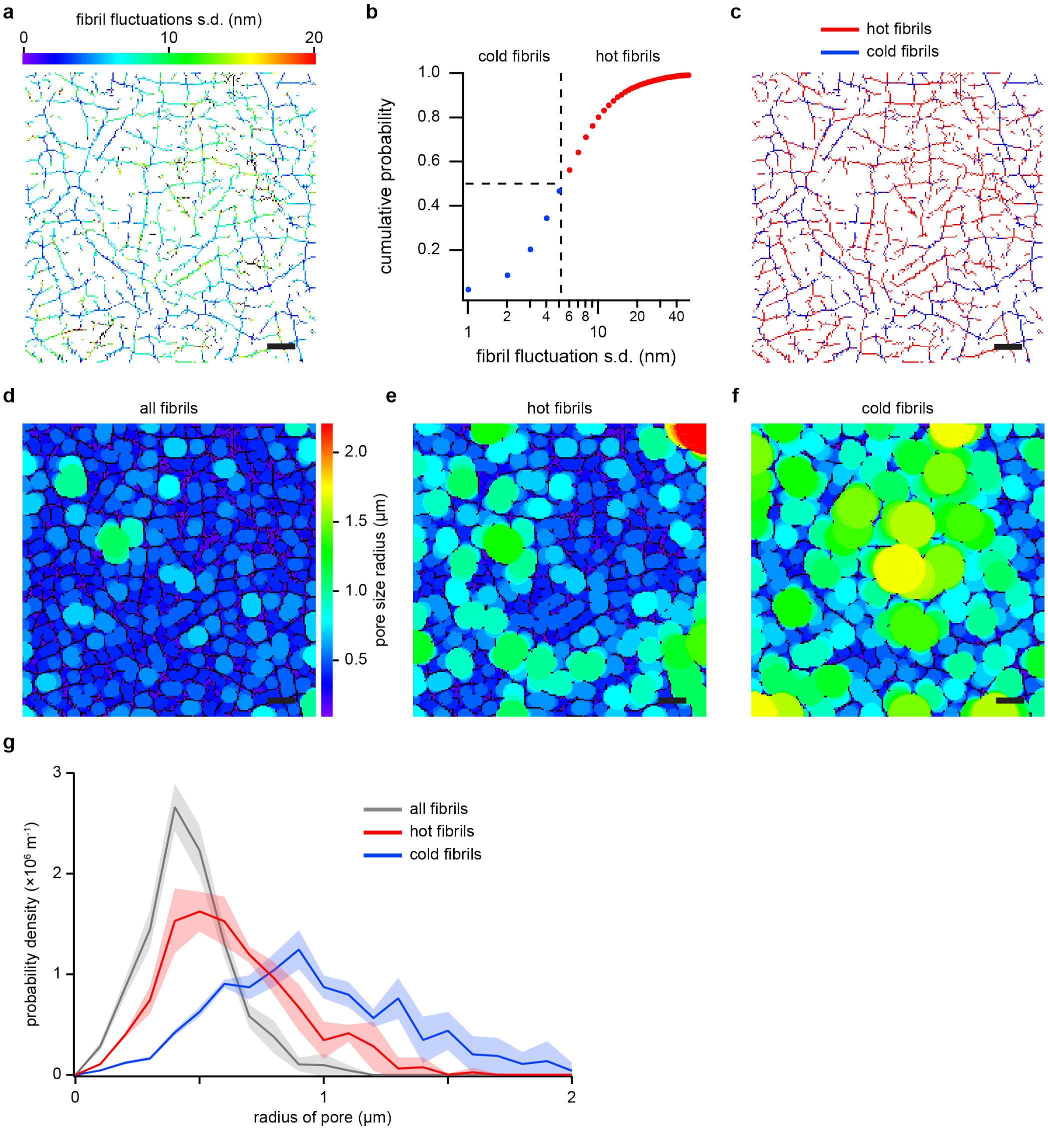

Figure 4.9: *Continued on the following page.*

Figure 4.9: Pore size distribution for strongly fluctuating (hot) versus weakly fluctuating (cold) fibrils. (**a**) Activity Microscopy image ($20\,\mu$m × $20\,\mu$m) of a network of native *in vitro* collagen I fibrils. The cumulative probability of fibril fluctuations for the image shown in **a** is used to divide fibrils equally into hot (red) and cold (blue) (**b**). The dashed lines indicate the median used to split the fibrils into hot and cold as also displayed in **c**. This image is used to calculate pore sizes between the network's fibrils (**d**) using a method described by Mickel *et al.* [126] (see section 4.2.8). The subset of hot fibrils forms smaller pores than the subset of cold fibrils (**e**, **f**). (**g**) The difference in pore sizes of networks of hot and cold fibrils can be quantified by the probability densities of their pore size radii. Cold fibrils form pores $\approx 1.6\times$ the size of the pores formed by hot fibrils (shaded region represents s.d. of four independent Activity Microscopy images of two different samples). Scale bars are $2\,\mu$m. Collagen was polymerized according to protocol II (see section 4.2.5).

the cold and hot fibrils shows again the large-scale pattern of cold filaments surrounding pockets of hot filaments (**Fig. 4.9 c**). To visualize the pore size distribution within an Activity Microscopy image, we plot the maximal pore size, color-coded for every pixel in the fluid phase either for all (**Fig. 4.9 d**), only hot (**Fig. 4.9 e**), or only cold fibrils (**Fig. 4.9 f**). The overall characteristics of the three cases is summarized in the probability density distribution of pore radii (**Fig. 4.9 g**). Except for a few pores, the pore radius for most pores is narrowly distributed around 435 nm. Hot filaments alone have a slightly higher peak pore radius of 567 nm. [3] In contrast, cold filaments have

---

[3] The average measured pore size is much smaller than measured by Mickel *et al.* [126] for similar collagen concentration and preparation. This is a result of the projection of all filaments within the focal depth into one plane. We calculate the projection depth to be $\pm 2.2\,\mu$m from the focal plane. Using an appropriate model for filament distribution and

clearly a much larger average pore radius indicated by the change in color and size of pores (**Fig. 4.9 f**) and the distribution of pore radii with a peak of 897 nm (**Fig. 4.9 g**). This confirms quantitatively the observation that cold filaments divide the network into pockets of hot filaments. Assuming that cold filaments are a result of tension along their axes, one could interpret the data as a few filaments carrying tension over long distances, while leaving pockets of relatively low-tension fibrils between them. To our knowledge, such a heterogeneous stress distribution has never been experimentally shown before.

4.3.5 Collagen Crosslinking

To demonstrate that Activity Microscopy imaging is sensitive to changes in the mechanics of collagen fibrils, we investigated networks crosslinked with glutaraldehyde, a molecular crosslinking agent commonly used for cell and tissue fixation. Glutaraldehyde crosslinks collagen fibrils internally by coupling individual collagen molecules and connecting the constituent proteins' surface lysines. It does not, however, change aspects of the network's structure, such as fiber width and length, or pore size [145]. Therefore, mainly a change in the stiffness of the fibrils and a corresponding reduction in transverse fluctuations are expected.

Figure 4.10 a and **c** show $30\,\mu\text{m} \times 30\,\mu\text{m}$ Activity Microscopy images of a native collagen network and a crosslinked network, respectively. Both networks were prepared in the same way except for the added crosslinking step

---

image formation, the two-dimensional can be linked to the three-dimensional pore size.

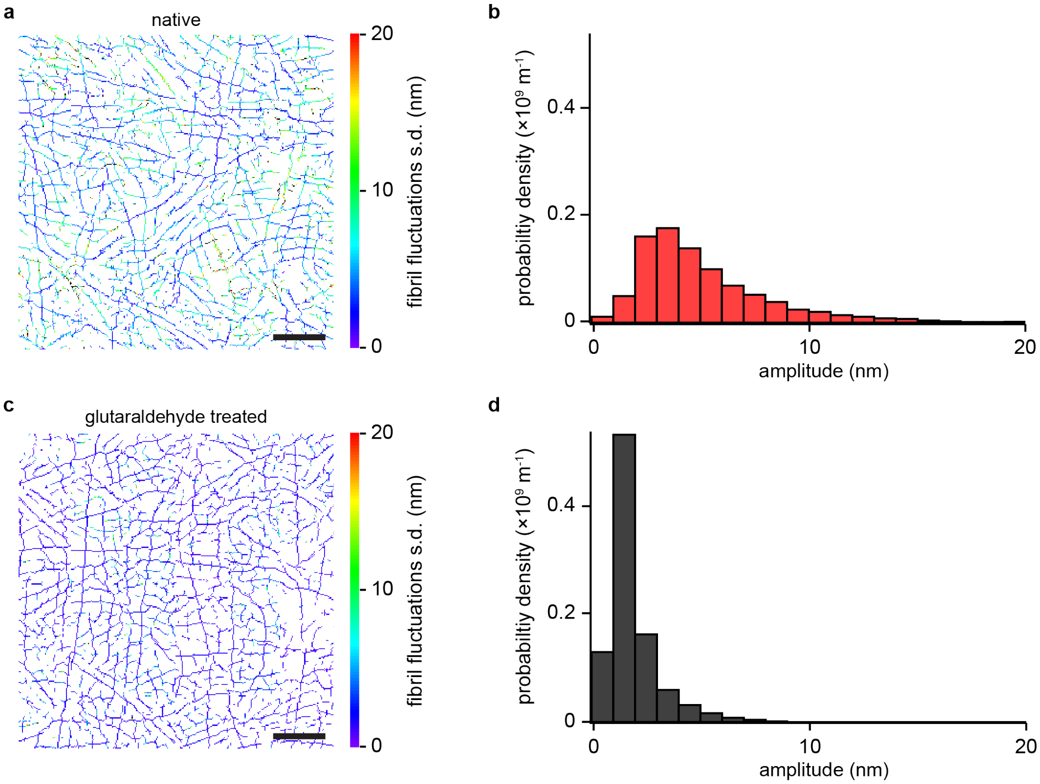

Figure 4.10: Reduction in collagen fibril fluctuations due to chemical crosslinking. (**a**) Activity Microscopy image of an *in vitro* network of native collagen I fibrils. (**b**) Probability density of fibril fluctuation amplitudes computed from all pixels shown in **a**. The peak of the distribution is located at 4.7 ± 0.7 nm (s.d. of five independent Activity Microscopy images of two different samples). (**c**) Activity Microscopy image of a collagen I network cross-linked with 4 % glutaraldehyde. (**d**) Probability density for the crosslinked network in **c**. Crosslinking leads to a reduction in fluctuation amplitudes with a new peak location around 1.6 ± 0.4 nm (s.d. of 4 independent Activity Microscopy images of 2 different samples). The bin width in **b** and **d** is 1 nm. Scale bars are 5 μm. The collagen networks were polymerized according to protocol I (see section 4.2.2).

(see section 4.2.3). The suppression of transverse fibril fluctuation through internal crosslinking of fibrils is immediately visible as a color shift corresponding to smaller fluctuations. To quantify the change in fibril fluctuations, we calculated the probability density distribution from the fluctuation amplitude for all fibrils shown in the Activity Microscopy images. **Figure 4.10 b** shows such a distribution for the native network. The distribution is asymmetric with a maximum around $3-4\,\mathrm{nm}$ and a long tail up to $20\,\mathrm{nm}$. After crosslinking, the distribution shows a strong shift towards smaller amplitudes with a maximum around $1\,\mathrm{nm}$ and a long tail up to $10\,\mathrm{nm}$ (**Fig. 4.10 d**). These data demonstrate the sensitivity of Activity Microscopy to subtle changes in filament mechanics.

4.3.6 HeLa Cells in a Collagen I Network: Active Forces

Cells growing and migrating in collagen matrices apply forces to individual fibrils that result in network deformations and remodeling [62]. To demonstrate that Activity Microscopy is able to quantify and visualize these changes, we seeded HeLa cells into collagen I matrices and measured fibril fluctuations at varying distance from the cells. HeLa cells, a standard immortal human cancer cell line, are known to proliferate but not migrate in collagen [146, 147], yet actively apply forces to the network. We expect fluctuations of fibrils under tension to be reduced, and the tension to fall off with the distance from the cell.

Figure 4.11 a shows the probability densities of fluctuations ampli-

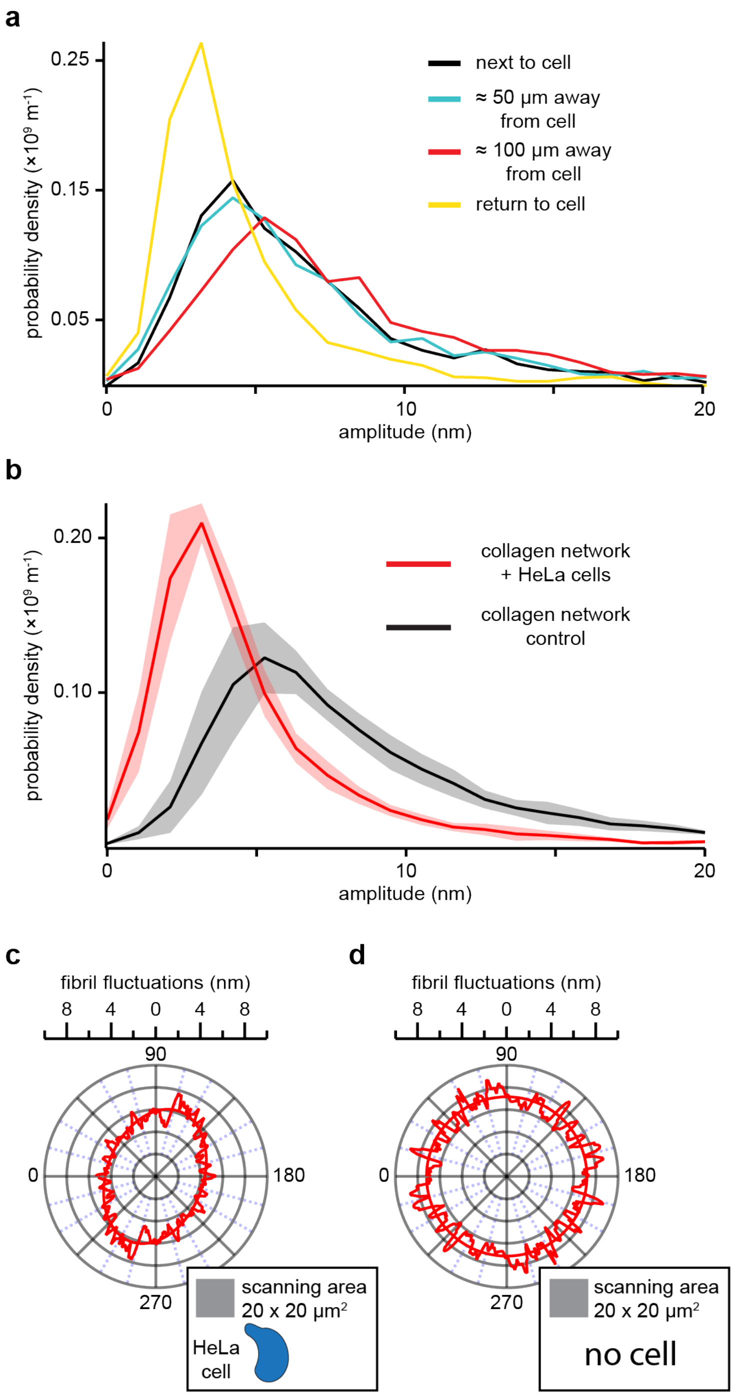

Figure 4.11: *Continued on the following page.*

Figure 4.11: Collagen I network response to embedded HeLa cells. (**a**) Probability density distributions of fibril fluctuation amplitudes at varying distances from a HeLa cell in an *in vitro* collagen I network. Each distribution was computed from a $10\,\mu\text{m} \times 10\,\mu\text{m}$ Activity Microscopy image. Each scan took $\approx 30\,\text{min}$ to complete. (**b**) Average probability density distribution (red) calculated from four different $20\,\mu\text{m}\times 20\,\mu\text{m}$ scans next to HeLa cells ($< 5\,\mu\text{m}$). The shaded region indicates the s.d.. For reference, an average probability distribution (black) calculated from four scans in a cell free network is shown. The presence of cells shifts the distribution towards smaller fluctuations, from 5.1 nm for cell free networks to 2.7 nm for networks with embedded HeLa cells. Fibrils analyzed for **b** can be sorted by their angle relative to the detector coordinate axes and the dependence of their fluctuations on this angle can be displayed in a polar graph (**c**). The fluctuation amplitudes reveal that radially oriented fibrils (w.r.t. the cell) display $\approx 37\,\%$ weaker fluctuations on average than tangentially oriented fibrils (see inset). No significant anisotropy is observed in cell free networks (**d**). Here, the data from one representative cell free network from **b** were used. All probability densities distributions have a bin width of 1 nm. The polar graphs show smoothed raw data (sliding box count = 4) and an elliptical fit. The collagen networks were polymerized according to protocol II (see section 4.2.5).

tudes measured in $10\,\mu\text{m} \times 10\,\mu\text{m}$ areas next to (black), $50\,\mu\text{m}$ (blue) and $100\,\mu\text{m}$ (red) away from a cell. While there is no significant difference between the distributions measured close to the cell (peak at 3.8 nm) and $50\,\mu\text{m}$ away (peak at 3.9 nm), the distribution shifts towards larger amplitudes at $100\,\mu\text{m}$ away (peak at 4.9 nm). Each measurement took $\approx 30\,\text{min}$ to complete which is sufficiently long to expect changes in the cell's state. We therefore recorded another distribution next to the cell (yellow). In contrast to the first recording, fluctuations are now strongly suppressed with a peak amplitude of 2.6 nm and a corresponding overall contraction of the distribution to smaller amplitudes. To confirm our observation, we repeated the experiments several times and increased the scan area to $20\,\mu\text{m} \times 20\,\mu\text{m}$ to increase the quality of the probability density distribution. For reference, we measured the distribution for cell free matrices prepared under the same conditions. The average of all measurements for matrices with cells (red) and without cells (black) are shown in **Figure 4.11 b**. The reduction in fluctuation amplitude relative to the cell free matrices confirms that the cells apply tension to the network. This tension seems to fall off within $100\,\mu\text{m}$ as the distribution measured $100\,\mu\text{m}$ away from the cell approaches the average distribution measured in cell free matrices. Anisotropy in tension is an additional signature expected for cells applying tension to the surrounding matrix. Cells pulling on the fibrils in their surroundings will deform the network. Fibrils radiating out will carry away and distribute the tension while concentric fibrils will experience reduced tension. To show this anisotropy, we analyzed the fluctuation amplitude dependent on their orientation to the detector coordinate axes. **Figure 4.11 c** shows a polar graph for fluctuations recorded around a point $20\,\mu\text{m}$ away from a cell. Fibrils radiating away from the cell show an $\approx 37\,\%$ reduction in fluctuation amplitude relative to fibrils oriented in perpendicular direction. The orientation of the ellipse agrees with the location of the cell relative to the scan area (inset). This can be independently confirmed by light microscopy imaging which allows us to determine the position of the cell relative to the scanned area. As a control, we applied the same analysis algorithm to data recorded on cell free collagen networks. In this case, as expected, fluctuation amplitudes are distributed isotropically (**Fig. 4.11 d**). In summary, these data demonstrate that the sensitivity range of Activity Microscopy imaging is well within the range of changes caused by cells to the matrix.

4.4 Discussion

Networks made of stiff biopolymers such as collagen I are usually modeled as athermal [81,143,148], i.e. the thermal undulations of their constituent filaments are assumed to play no significant role in their mechanical response. Here, we showed that thermally driven transverse filament fluctuations can nevertheless be measured, despite their ångstrøm to nanometer amplitudes. Finding the location of fibrils prior to fluctuation measurements allowed us to reduce two-dimensional imaging to effective one-dimensional fluctuation measurements along a fibril's contour. In this way, we were able to probe large areas of a network that include many pores, thus bridging the gap between single filament and overall network behavior. The observation of different pore sizes for cold and hot fibrils is one prominent result of this new ability. Further, we calculated probability density distributions of filament fluctuations representing the state of a network and its changes. We demonstrated that these changes can originate from increased stiffness of the individual fibrils in case of crosslinking or from tension applied to the fibrils in case of cells. Thus, Activity Microscopy imaging covers the relevant range of fluctuation amplitudes to characterize networks and their interaction with embedded HeLa cells. In both cases, the thickness of the sample ranged from $0.5 - 1.0\,\mathrm{mm}$, sufficiently large to treat the matrix as a three-dimensional network.

Recently, Steinwachs *et al.* [136] estimated the total force applied by a breast cancer cell to a collagen matrix to be on the order of 50 nN. As the pore size of the network is small relative to the cell's volume, the total force is expected to be distributed over many fibrils, with a maximum force per fibril in the nanonewton range or smaller. To estimate whether transverse fibril fluctuations are still within the range of Activity Microscopy, we calculated the transverse filament fluctuations based on a theory of semiflexible filaments under tension for fibril lengths of $10 - 40\,\mu$m and forces up to 10 nN (**Fig. 4.12**) [68, 72]. [4] Assuming a detection limit of 1 nm, all fluctuation amplitudes are within the range of Activity Microscopy. Only for the shortest collagen fibrils of length $10\,\mu$m and an applied tension of 10 nN, the detection threshold of 1 nm is reached. Very small forces do not significantly change

---

[4] The range of fluctuations that we observe in our images (¡ 1 nm up to 20 nm of fluctuation s.d.) agrees well with an analytical description of semiflexible filaments subject to thermal forces [68, 72]. Filament fluctuations can be decomposed into q modes of motion, each with a fluctuation amplitude u_q. The variance of the fluctuation amplitudes is then given by 1.11:

$$\langle |u_q|^2 \rangle = \frac{2k_B T}{l_c(\kappa q^4 + \tau q^2)}, \tag{4.2}$$

where l is the filament's contour length, k_B is the Boltzmann constant, T the temperature, τ is its tension, and $\kappa = \frac{\pi}{4} E a^4$ is the filament's bending stiffness, which includes the radius a and the Young's modulus E. Taking the wave vectors q as $q = n\pi/l$, with $n = 1, 2, 3,$ one can write the average fluctuation amplitude observed as (1.12):

$$\sqrt{\langle |u|^2 \rangle} = \sqrt{\int_{q_1}^{q_\infty} \langle |u_q^2| \rangle} \approx \left[\sum_{n=1}^{\infty} \frac{2k_B T}{\kappa n^4 \pi^4 / l^3 + \tau n^2 \pi^2 / l} \right]^{\frac{1}{2}}. \tag{4.3}$$

Our estimate shows that even for fibrils of $10\,\mu$m length and a tension of 10 nN applied to its ends, transverse filament fluctuations (≈ 1 nm) are still in the current sensitivity range of Activity Microscopy (**Fig. 4.12**).

the fluctuation amplitudes (see plateaus in **Fig. 4.12**). The minimal detectable tension depends on the fibril length. For example, for collagen fibrils of length $10\,\mu$m, only tensions larger than $100\,$pN significantly change fluctuations amplitudes. For $40\,\mu$m fibrils, this threshold is much lower, around tens of piconewtons. These estimates show that Activity Microscopy covers the relevant force range for studying cell-matrix interaction also for cells that are expected to show strong interactions with the surrounding matrix, such as migrating cancer cells [149].

Imaging speed is another factor required to follow cell-matrix interaction of motile cells. For our study, we chose HeLa cells that are known to interact with collagen matrix, but are unable to migrate [146, 147], leaving sufficient time to image the selected areas of the network around them. Migrating cancer cells, however, move with speeds on the order of micrometers per minute [150], a time scale on which one would like to monitor their interaction with all fibrils of the matrix. This poses a challenge for Activity Microscopy that can be met with current technology. Pre-scans of volumes around a cell, required for finding all fibrils in a network, can be sped up to less than a minute by using a fast scanning mode of the scanning stage instead of the step by step scanning mode used in this work. This will reduce the precision in localizing the fibrils, but as we pointed out above, the precise knowledge of fibril position is not required for the measurement of fibril fluctuations as long as the fibril remains in the linear range of the detector (**Fig.**

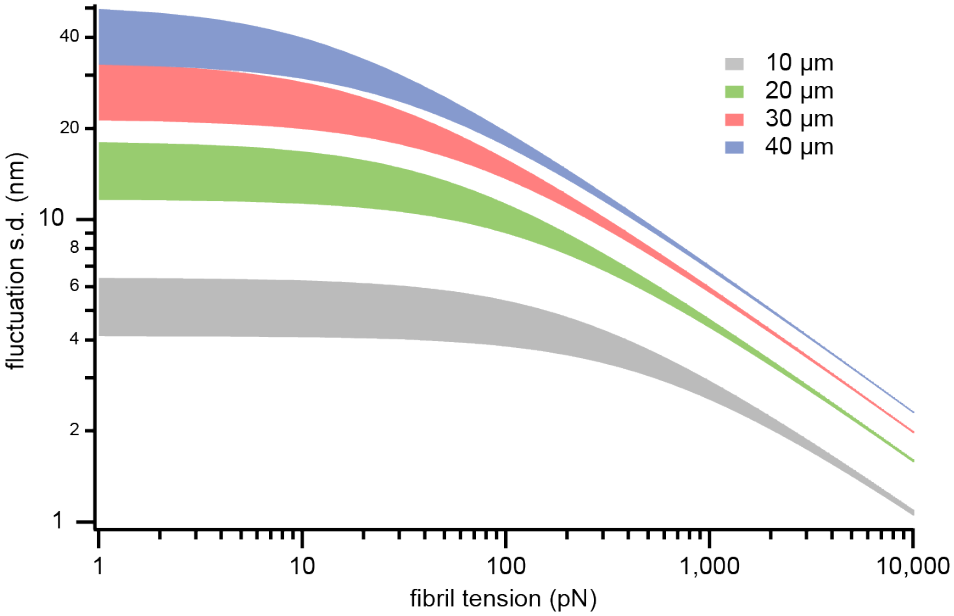

Figure 4.12: Transverse fibril fluctuation amplitude versus fibril tension. The graph shows the theoretical dependence of transversal fluctuations on tension applied to a semiflexible filament (Supplementary Note 3). Four traces are shown for fibrils of fixed diameter $d = 160\,\text{nm}$ and variable contour lengths, $10\,\mu\text{m}$, $20\,\mu\text{m}$, $30\,\mu\text{m}$ and $40\,\mu\text{m}$. This is a reasonable length regime as the typical fibril length is much longer than the pore size [46]. The vertical width of each trace shows the variability of fluctuation for a range in a collagen fibril's Young's modulus $E = 0.07\,\text{GPa} - 0.17\,\text{GPa}$ previously measured [66].

4.5). The characteristic length scale of the network is set by the pore size. The imaging speed can therefore be increased by measuring a fibril's fluctuations only at single points spaced by the network pore size. Assuming a pore diameter of $2.5\,\mu\text{m}$ [145], this will reduce the time required to measure fibril fluctuations by a factor of 25, compared to our current stepsize of 100 nm. These two improvements in imaging speed might be sufficient for studying the interaction between motile cells and their surrounding matrix.

Activity Microscopy also has broad applications in materials research, where networks are static and hence much easier to image. Collagen networks are extremely stable and therefore large volumes can be imaged. We expect to gain new insight into how single filament mechanics and network architecture lead to macroscopic mechanical properties. This allows for a systematic study of network preparation conditions and a rational design of networks with desired properties. The response to point and shear forces and other network manipulations such as enzymatic activity or chemical treatment by cross-linkers can also be studied.

Chapter 5

Summary and Future Work

5.1 Summary

In the previous chapters, we have introduced two novel forms of microscopy enabling unique ways of studying biological soft matter, in particular biopolymer networks. Thermal Noise Imaging utilizes the thermal fluctuations of a trapped nanoparticle as a soft scanning probe. If applied to filamentous structures such as microtubules, or collagen fibrils in a network, the data reports on location and diameter of the structure, but also encodes information about thermal fluctuations. Activity Microscopy on the other hand directly measures thermal fluctuations along the entirety of filaments in a network, and eliminates the requirement for a probe particle. The measured fluctuations serve as an indicator for stress applied to the filament as well as mechanical properties like the bending stiffness. There are many promising directions in which both techniques could be carried into the future, some of which were already discussed in the conclusions of Chapter 3 and 4. So in the following I would like to focus on two key future projects for Activity Microscopy which are in close reach, one technical improvement and one application.

5.2 Activity Microscopy - Three-dimensional Scanning and Imaging

As presented in this work Activity Microscopy is a two-dimensional scanning technique. It would be a natural progression to expand scanning capabilities into the third dimension. Since fibrils in a collagen network are not always necessarily aligned in parallel to the imaging plane rather represent an entangled network with random fibril orientation in three-dimensional space, we are actually recording a projection along the optical axis into the imaging plane. We calculate the projection depth to be $\pm 2.2\,\mu$m from the imaging plane. This is also the cause for the under estimate in collagen network pore size we show in **Figure 4.9**. In order to move towards three-dimensional scanning two major challenges have to be overcome: data interpretation and analysis, as well as scanning speed. Let us address the latter first. Activity Microscopy as presented in this work relies on step-wise point scanning, i.e. the stage is stepped from position to position, usually with a stepsize of 100 nm. The stage's response time to move from its current position to the next was measured to be $\sim$ 10 ms and independent of how big the step is. We can exploit this fact and "jump" over the entire range of the stage which is 50 μm laterally and 75 μm axially in one big step while recording continuously. According to the manufacturer the scanning speed can be ramped up to a maximum of 400 Hz, but taking the measured response time into consideration we expect a maximum speed of 100 Hz. As such we are able to scan the full range within 7 min, assuming a distance of 100 nm between the jumps, and a 1 μm distance between axial layers. This improvement will enable the detection of all fibrils in a network and speed up the process by a factor of 500. Nevertheless, the action of fluctuation recording remains slow, but can be improved by spacing out the measurements along the fibril as already alluded to in section 4.4. This is justifiable by observing that the fluctuation magnitude of a fibril does not change significantly on length scales below the network's pore size. In areas where more information is required, such as close to a cell which might be present, data points at a higher density can be acquired again. Of course, the former challenge needs to be addressed as well with an appropriate improvement in detection software. Efforts to this end were begun by the author, but will require more time investments.

5.3 Collagen Network underlying Heart Valves imaged by Activity Microscopy

One exciting possible application of the technique is to study the collagen mesh underlying heart valves, either from animal or human sources. Collagen networks are a main component of the heart and its valves, providing the necessary stability and elasticity [43]. Degradation and failure of the heart and heart valve tissue is closely related to the breakdown of the underlying collagen network either with age, or disease [44]. Activity Microscopy can deliver valuable insight into the changes in structure and stress distribution when comparing heart valves of varying loading conditions or different number of cycles. To study the underlying collagen network in isolation we have to remove cells present in the tissue. To that end appropriate decellularization protocols can be utilized, for example found here [151] or here [152]. In brief, a mixture of different detergents lyses the cells and their remains are washed out, while care is taken not to destroy the underlying network. Our studies would contribute to the further improvement of biophrosphetic heart valves which have been used for decades, but have a limited lifetime [153, 154].

Bibliography

[1] M. Knoll and E. Ruska. Das Elektronenmikroskop. *E. Z. Physik*, 78(318):318–339, 1932.

[2] P. Brzezinski. The Development of Cryo-Electron Microscopy. *The Royal Swedish Academy of Sciences*, 2017.

[3] J. W. Lichtman and J.-A. Conchello. Fluorescence Microscopy. *Nature Methods*, 2(12):910–919, 2005.

[4] B.-C. Chen, W. R. Legant, K. Wang, L. Shao, D. E. Milkie, M. W. Davidson, C. Janetopoulos, X. S. Wu, J. A. Hammer, Z. Liu, B. P. English, Y. Mimori-Kiyosue, D. P. Romero, A. T. Ritter, J. Lippincott-Schwartz, L. Fritz-Laylin, R. D. Mullins, D. M. Mitchell, J. N. Bembenek, A.-C. Reymann, R. Bohme, S. W. Grill, J. T. Wang, G. Seydoux, U. S. Tulu, D. P. Kiehart, and E. Betzig. Lattice light-sheet microscopy: Imaging molecules to embryos at high spatiotemporal resolution. *Science*, 346(6208):1257998–1–12, 2014.

[5] M. Ehrenberg. Super-Resolved Fluorescence Microscopy. *The Royal Swedish Academy of Sciences*, 2014.

[6] P. A. Janmey, J. P. Winer, M. E. Murray, and Q. Wen. The Hard Life of Soft Cells. *Cell Motility and the Cytoskeleton*, 66(8):597–605, 2009.

[7] A. W. Holle, J. L. Young, K. J. Van Vliet, R. D. Kamm, D. Discher, P. Janmey, J. P. Spatz, and T. Saif. Cell-Extracellular Matrix Mechanobiology: Forceful Tools and Emerging Needs for Basic and Translational Research. *Nano Letters*, 18:1–8, 2018.

[8] F. Grinnell, C.-C. Ho, E. Tamariz, D. J. Lee, and G. Skuta. Dendritic Fibroblasts in Three-dimensional Collagen Matrices. *Molecular Biology of the Cell*, 14:384–395, 2003.

[9] R. Hooke. *Micrographia, Or, Some Physiological Descriptions of Minute Bodies Made by Magnifying Glasses: with Observations and Inquiries Thereupon.* Royal Society, London, UK, 1665.

[10] E. Bianconi, A. Piovesan, F. Facchin, A. Beraudi, R. Casadei, F. Frabetti, L. Vitale, M. C. Pelleri, S. Tassani, F. Piva, S. Perez-Amodio, P. Strippoli, and S. Canaider. An estimation of the number of cells in the human body. *Annals of Human Biology*, 40(6):463–471, 2013.

[11] R. Sender, S. Fuchs, and R. Milo. Revised Estimates for the Number of Human and Bacteria Cells in the Body. *PLOS Biology*, 14(8):1–14, 2016.

[12] B. A. Webb, M. Chimenti, M. P. Jacobson, and D. L. Barber. Dysregulated pH: a perfect storm for cancer progression. *Nature Reviews Cancer*, 11(9):671–677, 2011.

[13] A. M. Anesio, S. Lutz, N. A. M. Chrismas, and L. G. Benning. The microbiome of glaciers and ice sheets. *npj Biofilms and Microbiomes*, 3(10):1–11, 2017.

[14] R. C. Lynch, A. J. King, M. E. Farias, P. Sowell, C. Vitry, and S. K. Schmidt. The potential for microbial life in the highest-elevation (>6000 m.a.s.l.) mineral soils of the Atacama region. *Journal of Geophysical Research: Biogeosciences*, 117(2):1–10, 2012.

[15] J. T. Nielsen, N. V. Kulminskaya, M. Bjerring, J. M. Linnanto, M. Rätsep, M. O. Pedersen, P. H. Lambrev, M. Dorogi, G. Garab, K. Thomsen, C. Jegerschöld, N. U. Frigaard, M. Lindahl, and N. C. Nielsen. In situ high-resolution structure of the baseplate antenna complex in Chlorobaculum tepidum. *Nature Communications*, 7(12454):1–12, 2016.

[16] S. Ornes. How nonequilibrium thermodynamics speaks to the mystery of life. *Proceedings of the National Academy of Sciences*, 114(3):423–424, 2017.

[17] C. Battle, C. P. Broedersz, N. Fakhri, V. F. Geyer, J. Howard, C. F. Schmidt, and F. C. MacKintosh. Broken detailed balance at mesoscopic scales in active biological systems. *Science*, 352(6285):604–607, 2016.

[18] A. Pralle, P. Keller, E.-L. Florin, K. Simons, and J. K.H. Hörber. Sphingolipid Cholesterol Rafts Diffuse as Small Entities in the Plasma Membrane of Mammalian Cells. *Journal of Cell Biology*, 148(5):997–1007, 2000.

[19] A. Keidel, T. F. Bartsch, and E.-L. Florin. Direct observation of intermediate states in model membrane fusion. *Scientific Reports*, 6(23691):1–11, 2016.

[20] K. Takata, T. Matsuzaki, and Y. Tajika. Aquaporins: Water channel proteins of the cell membrane. *Progress in Histochemistry and Cytochemistry*, 39:1–83, 2004.

[21] Y. Kurachi and A. North. Ion channels: their structure, function and control - an overview. *Journal of Physiology*, 554(2):245–247, 2004.

[22] B. Alberts, A. Johnson, J. Lewis, M. Raff, K. Roberts, and P. Walter. *Molecular Biology of the Cell, 4th edition.* Garland Science, New York, NY, 2002.

[23] R. J. Ellis. Macromolecular crowding: obvious but underappreciated. *TRENDS in Biochemical Sciences*, 26(10):597–604, 2001.

[24] https://imagej.nih.gov/ij/images/FluorescentCells.jpg.

[25] Ali Zifan. Diagram of a typical prokaryotic cell. *https://en.wikipedia.org/wiki/Prokaryote#/media/File:Prokaryote_cell.svg*.

[26] Mariana Ruiz. Structure of a typical animal cell. *https://en.wikipedia.org/wiki/Eukaryote#/media/File:Animal_cell_structure_en.svg*.

[27] M. Lynch and J. S. Conery. The Origins of Genome Complexity. *Science*, 302(5649):1401–1404, 2003.

[28] V. D. Gordon, M. Davis-Fields, K. Kovach, and C. A. Rodesney. Biofilms and mechanics: A review of experimental techniques and findings. *Journal of Physics D: Applied Physics*, 50(22), 2017.

[29] K. F. Jarrell and M. J. McBride. The surprisingly diverse ways that prokaryotes move. *Nature Reviews Microbiology*, 6:466–476, 2008.

[30] A. Be'er and R. M. Harshey. Collective Motion of Surfactant-Producing Bacteria Imparts Superdiffusivity to Their Upper Surface. *Biophysical Journal*, 101(5):1–8, 2011.

[31] F. Pampaloni and E.-L. Florin. Microtubule architecture: inspiration for novel carbon nanotube-based biomimetic materials. *Trends in Biotechnology*, 26(6):302–310, 2008.

[32] K. M. Taute, F. Pampaloni, E. Frey, and E.-L. Florin. Microtubule Dynamics Depart from the Wormlike Chain Model. *Physical Review Letters*, 100(2):028102–1–4, 2008.

[33] F. Gittes, B. Mickey, J. Nettleton, and J. Howard. Flexural rigidity of microtubules and actin filaments measured from thermal fluctuations in shape. *The Journal of Cell Biology*, 120(4):923–934, 1993.

[34] A. Nürnberg, T. Kitzing, and R. Grosse. Nucleating actin for invasion. *Nature Reviews Cancer*, 11:117–187, 2011.

[35] T. D. Pollard. Rate Constants for the Reactions of ATP- and ADP-Actin with the Ends of Actin Filaments. *The Journal of Cell Biology*, 103(6):2747–2754, 1986.

[36] From MOLECULAR BIOLOGY OF THE CELL, SIXTH EDITION by Bruce Alberts, et al. Copyright © 2015 by Bruce Alberts, Alexander Johnson, Julian Lewis, David Morgan, Martin Raff, Keith Roberts, and Peter Walter. Used by permission of W.W. Norton & Company, Inc.

[37] D Vavylonis, Q Yang, and B O'Shaughnessy. Actin polymerization kinetics, cap structure, and fluctuations. *Proceedings of the National Academy of Sciences*, 102(24):8543–8548, 2005.

[38] J. M. A. Farsi and J. E. Aubin. Microfilament Rearrangements During Fibroblast-Induced Contraction of Three-Dimensional Hydrated Collagen Gels. *Cell Motility*, 4:29–40, 1984.

[39] Y. Tambe. Actin cytoskeleton of mouse embryo fibroblasts, stained with Fluorescein isothiocyanate-phalloidin. *https://en.wikipedia.org/wiki/Microfilament#/media/File:MEF_microfilaments.jpg.*

[40] E. Fuchs and K. Weber. Intermediate Filaments: Structure, Dynamics, Function, and Disease. *Annu. Rev. Biochem.*, 63:345–382, 1994.

[41] C. Frantz, K. M. Stewart, and V. M. Weaver. The extracellular matrix at a glance. *Journal of Cell Science*, 123(24):4195–4200, 2010.

[42] T. Nishida, K. Yasumoto, T. Orori, and J. Desaki. The Network Structure of Corneal Fibroblasts in the Rat as Revealed by Scanning Electron Microscopy. *Investigative Ophthalmology & Visual Science*, 29(12):1887–1890, 1988.

[43] M. S. Sacks, W. D. Merryman, and D. E. Schmidt. On the biomechanics of heart valve function. *Journal of Biomechanics*, 42:1804–1824, 2009.

[44] M. A. Horn and A. W. Trafford. Aging and the cardiac collagen matrix: Novel mediators of fibrotic remodelling. *Journal of Molecular and Cellular Cardiology*, 93:175–185, 2016.

[45] G. C. Wood and M. K. Keech. The Formation of Fibrils from Collagen Solutions. *Biochemical Journal*, 75:588–598, 1960.

[46] K. E. Kadler, D. F. Holmes, J. A. Trotter, and J. A. Chapman. Collagen fibril formation. *Biochemical Journal*, 316:1–11, 1996.

[47] K. A. Jansen, A. J. Licup, A. Sharma, R. Rens, F. C. MacKintosh, and G. H. Koenderink. The Role of Network Architecture in Collagen Mechanics. *Biophysical Journal*, 114:2665–2678, 2018.

[48] J. Bella. Collagen structure: new tricks from a very old dog. *Biochemical Journal*, 473:1001–1025, 2016.

[49] M. J. Buehler. Nature designs tough collagen: Explaining the nanostructure of collagen fibrils. *Proceedings of the National Academy of Sciences*, 103(33):12285–12290, 2006.

[50] M. E. Nimni. *Collagen: Biochemistry, Volume 1.* Taylor & Francis Group, Boca Raton, FL 33487-2742, 2018.

[51] Y. I. Tarasevich. State and Structure of Water in Vicinity of Hydrophobic Surfaces. *Colloid Journal*, 73(2):257–266, 2011.

[52] M. Asgari, N. Latifi, H. K. Heris, H. Vali, and L. Mongeau. In vitro fibrillogenesis of tropocollagen type III in collagen type i affects its relative fibrillar topology and mechanics. *Scientific Reports*, 7:1–10, 2017.

[53] C. B. Raub, V. Suresh, T. Krasieva, J. Lyubovitsky, J. D. Mih, A. J. Putnam, B. J. Tromberg, and S. C. George. Noninvasive Assessment of Collagen Gel Microstructure and Mechanics Using Multiphoton Microscopy. *Biophysical Journal*, 92:2212–2222, 2007.

[54] J. Gross and D. Kirk. The heat precipitation of collagen from neutral salt solutions: some rate-regulating factors. *The Journal of Biological Chemistry*, 233(2):355–360, 1958.

[55] H. Clevers. Modeling Development and Disease with Organoids. *Cell*, 165:1586–1597, 2016.

[56] S. Bartfeld and H. Clevers. Stem cell-derived organoids and their application for medical research and patient treatment. *Journal of Molecular Medicine*, 95(7):729–738, 2017.

[57] E. Moeendarbary and A. R. Harris. Cell mechanics: Principles, practices, and prospects. *WIREs: Systems Biology and Medicine*, 6:371–388, 2014.

[58] D. A. Fletcher and R. D. Mullins. Cell mechanics and the cytoskeleton. *Nature*, 463(28):485–492, 2010.

[59] A. J. Engler, S. Sen, H. L. Sweeney, and D. E. Discher. Matrix Elasticity Directs Stem Cell Lineage Specification. *Cell*, 126:677–689, 2006.

[60] J. J. Tomasek, E. D. Hay, and K. Fujiwara. Collagen Modulates Cell Shape and Cytoskeleton of Embryonic Corneal and Fibroma Fibroblasts: Distribution of Actin, α-Actinin, and Myosin. *Developmental Biology*, 92:107–122, 1982.

[61] L. Sapir and S. Tzlil. Talking Over the Extracellular Matrix: How do Cells Communicate Mechanically? *Seminars in Cell and Developmental Biology*, 71:99–105, 2017.

[62] P. Friedl, K. S. Zänker, and E.-B. Bröcker. Cell Migration Strategies in 3D Extracellular Matrix: Differences in Morphology, Cell Matrix Interactions, and Integrin Function. *Microscopy Research and Technique*, 43:369–378, 1998.

[63] M. Egeblad, M. G. Rasch, and V. M. Weaver. Dynamic interplay between the collagen scaffold and tumor evolution. *Current Opinion in Cell Biology*, 22:697–706, 2010.

[64] F. Pampaloni, G. Lattanzi, A. Jonas, T. Surrey, E. Frey, and E.-L. Florin. Thermal fluctuations of grafted microtubules provide evidence of a length-dependent persistence length. *Proceedings of the National Academy of Sciences*, 103(27):10248–10253, 2006.

[65] E. M. Lifshitz, A. M. Kosevich, and L. P. Pitaevskii. *Theory of Elasticity (Third Edition)*. 1986.

[66] L. Yang, K. O. van der Werf, C. F. C. Fitié, M. L. Bennink, P. J. Dijkstra, and J. Feijen. Mechanical Properties of Native and Cross-linked Type I Collagen Fibrils. *Biophysical Journal*, 94:2204–2211, 2008.

[67] O. Kratky and G. Porod. Röntgenuntersuchung gelöster Fadenmoleküle. *Recueil des Travaux Chimiques des Pays-Bas*, 68:1106–1122, 1949.

[68] C. P. Broedersz and F. C. Mackintosh. Modeling semiflexible polymer networks. *Reviews of Modern Physics*, 86:995–1036, 2014.

[69] J. Wilhelm and E. Frey. Radial Distribution Function of Semiflexible Polymers. *Physical Review Letters*, 77(12):2581–2584, 1996.

[70] F. Valle, M. Favre, P. De Los Rios, A. Rosa, and G. Dietler. Scaling Exponents and Probability Distributions of DNA End-to-End Distance. *Physical Review Letters*, 95:158105–1–4, 2005.

[71] M. D. Wang, H. Yin, R. Landick, J. Gelles, and S. M. Block. Stretching DNA with Optical Tweezers. *Biophysical Journal*, 72:1335–1346, 1997.

[72] F. C. MacKintosh, J. Käs, and P. A. Janmey. Elasticity of Semiflexible Biopolymer Networks. *Physical Review Letters*, 75(24):4425–4428, 1995.

[73] C. Storm, J. J. Pastore, F. C. MacKintosh, T. C. Lubensky, and P. A. Jamney. Nonlinear elasticity in biological gels. *Nature*, 435:191–194, 2005.

[74] P. A. Janmey, M. E. McCormick, S. Rammensee, J. L. Leight, P. C. Georges, and F. C. MacKintosh. Negative normal stress in semiflexible biopolymer gels. *Nature Materials*, 6:48–51, 2007.

[75] J. P. Winer, S. Oake, and P. A. Janmey. Non-linear Elasticity of Extracellular Matrices Enables Contractile Cells to Communicate Local Position and Orientation. *PLoS ONE*, 4(7):e6382, 2009.

[76] Q. Wen and P. A. Janmey. Effects of non-linearity on cell-ECM interactions. *Experimental Cell Research*, 319:2481–2489, 2013.

[77] M. S. Rudnicki, H. A. Cirka, M. Aghvami, E. A. Sander, Q. Wen, and K. L. Billiar. Nonlinear Strain Stiffening Is Not Sufficient to Explain How Far Cells Can Feel on Fibrous Protein Gels. *Biophysical Journal*, 105:11–20, 2013.

[78] M. L. Gardel, J. H. Shin, F. C. MacKintosh, L. Mahadevan, P. Matsudaira, and D. A. Weitz. Elastic behavior of cross-linked and bundled actin networks. *Science*, 304(5675):1301–1305, 2004.

[79] A. Gautieri, S. Vesentini, A. Redaelli, and M. J. Buehler. Hierarchical Structure and Nanomechanics of Collagen Microfibrils from the Atomistic Scale Up. *Nano Letters*, 11:757–766, 2011.

[80] S. Varma, J. P. R. O. Orgel, and J. D. Schieber. Nanomechanics of Type I Collagen. *Biophysical Journal*, 111:50–56, 2016.

[81] A. J. Licup, S. Münster, A. Sharma, M. Sheinman, L. M. Jawerth, B. Fabry, D. A. Weitz, and F. C. MacKintosh. Stress controls the mechanics of collagen networks. *Proceedings of the National Academy of Sciences*, 112(31):9573–9578, 2015.

[82] P. R. Onck, T. Koeman, T. Van Dillen, and E. Van Der Giessen. Alternative Explanation of Stiffening in Cross-Linked Semiflexible Networks. *Physical Review Letters*, 95:178102–1–178102–4, 2005.

[83] J. C. Maxwell. On the calculation of the equilibrium and stiffness of frames. *The London, Edinburgh, and Dublin Philosophical Magazine and Journal of Science*, 27(182):294–299, 1864.

[84] O. Lieleg, M. M. A. E. Claessens, C. Heussinger, E. Frey, and A. R. Bausch. Mechanics of Bundled Semiflexible Polymer Networks. *Physical Review Letters*, 99:088102–1–4, 2007.

[85] J. K. H. Hörber, E.-L. Florin, and E. H. K. Stelzer. Photonische Kraftmikroskopie. *Physikalische Blätter*, 56(5):41–44, 2000.

[86] C. Tischer, S. Altmann, S. Fišinger, J. K. H. Hörber, E. H. K. Stelzer, and E.-L. Florin. Three-dimensional thermal noise imaging. *Applied Physics Letters*, 79:3878–3880, 2001.

[87] T. F. Bartsch. *Submicroscopic characterization of biopolymer networks in solution by Thermal Noise Imaging.* Dissertation, The University of Texas at Austin, 2013.

[88] M. D. Kochanczyk. *Development of Quantitative Three-Dimensional Thermal Noise Imaging of Biopolymer Networks.* PhD thesis, The University of Texas at Austin, 2012.

[89] K. König, H. Liang, M. W. Berns, and B. J. Tromberg. Cell damage in near-infrared multimode optical traps as a result of multiphoton absorption. *Optics Letters*, 21(14):1090–1092, 1996.

[90] V. Magidson and A. Khodjakov. Circumventing photodamage in live-cell microscopy. *Methods Cell Biol.*, 114, 2013.

[91] P. Kwee, C. Bogan, K. Danzmann, M. Frede, H. Kim, P. King, O. Puncken, R. L. Savage, F. Seifert, P. Wessels, L. Winkelmann, and B. Willke. Stabilized high-power laser system for LIGO. *Optics Express*, 20(10):10617–10634, 2012.

[92] Martin D. Kochanczyk, Tobias F. Bartsch, Katja M. Taute, and Ernst-Ludwig Florin. Power spectral density integration analysis and its appli-

cation to large bandwidth, high precision position measurements. (October 2012):84580H, 2012.

[93] A. Ashkin. Forces of a single-beam gradient laser trap on a dielectric sphere in the ray optics regime. *Biophysical Journal*, 61(2):569–582, 1992.

[94] A. Ashkin, J. M. Dziedzic, J. E. Bjorkholm, and S. Chu. Observation of a single-beam gradient force optical trap for dielectric particles. *Optics Letters*, 11(5):288–290, 1986.

[95] The Nobel Committee for Physics. Groundbreaking Inventions in Laser Physics - Optical Tweezers and Generation of High-Intensity, Ultra-short optical pulses. *The Royal Swedish Academy of Sciences*, 2018.

[96] K. C. Neuman and S. M. Block. Optical trapping. *Review of Scientific Instruments*, 75(9):2787–2809, 2004.

[97] T. F. Bartsch, S. Fišinger, M. D. Kochanczyk, R. Huang, A. Jonáš, and E.-L. Florin. Detecting Sequential Bond Formation Using Three-Dimensional Thermal Fluctuation Analysis. *ChemPhysChem*, 10:1541–1547, 2009.

[98] A. A. E. Saleh and J. A. Dionne. Toward Efficient Optical Trapping of Sub-10-nm Particles with Coaxial Plasmonic Apertures. *Nano Letters*, 12:5581–5586, 2012.

[99] H. Zhang and K. K. Liu. Optical tweezers for single cells. *Journal of the Royal Society Interface*, 5(24):671–690, 2008.

[100] J. Guck, R. Ananthakrishnan, T. J. Moon, C. C. Cunningham, and J. Käs. The Optical Stretcher - A Novel Laser Tool to Micromanipulate Cells. *Biophysical Journal*, 81:767–784, 2001.

[101] A. Ashkin and J. M. Dziedzic. Optical Trapping and Manipulation of Single Cells Using Infra-Red Laser Beams. *Ber. Bunsenges. Phys. Chem.*, 93:254–260, 1989.

[102] R. Feynman. *The Feynman lectures on Physics.* Basic Books, New York, NY, 2013.

[103] R. Huang, I. Chavez, K. M. Taute, B. Lukić, S. Jeney, M. G. Raizen, and E.-L. Florin. Direct observation of the full transition from ballistic to diffusive Brownian motion in a liquid. *Nature Physics*, 7:576–580, 2011.

[104] A. Einstein. Zur Theorie der Brownschen Bewegung. *Annalen der Physik*, pages 371–381, 1906.

[105] P. Langevin. Sur la théorie du mouvement brownien. *Comptes-rendus de l'Académie des Sciences (Paris)*, 146:530 – 533, 1908.

[106] D. S. Lemons and A. Gythiel. Paul Langevin's 1908 paper On the Theory of Brownian Motion [Sur la théorie du mouvement brownien,

C. R. Acad. Sci. (Paris) 146 , 530533 (1908)]. *American Journal of Physics*, 65:1079–1081, 1997.

[107] E.-L. Florin, A. Pralle, E.H.K. Stelzer, and J.K.H. Hörber. Photonic force microscope calibration by thermal noise analysis. *Applied Physics A: Materials Science & Processing*, 66:S75–S78, 1998.

[108] F. Gittes and C. F. Schmidt. Interference model for back-focal-plane displacement detection in optical tweezers. *Optics Letters*, 23(1):7–9, 1998.

[109] A. Pralle, M. Prummer, E.-L. Florin, E. H. K. Stelzer, and J. K. H. Hörber. Three-Dimensional High-Resolution Particle Tracking for Optical Tweezers by Forward Scattered Light. *Microscopy Research and Technique*, 44:378–386, 1999.

[110] C. Tischer, A. Pralle, and E.-L. Florin. Determination and Correction of Position Detection Nonlinearity in Single Particle Tracking and Three-Dimensional Scanning Probe Microscopy. *Microscopy and Microanalysis*, 10:425–434, 2004.

[111] H. Kress, E. H. K. Stelzer, and A. Rohrbach. Tilt angle dependent three-dimensional-position detection of a trapped cylindrical particle in a focused laser beam. *Applied Physics Letters*, 84:4271–4273, 2004.

[112] T. F. Bartsch, M. D. Kochanczyk, E. N. Lissek, J. R. Lange, and E.-L.

Florin. Nanoscopic imaging of thick heterogeneous soft-matter structures in aqueous solution. *Nature Communications*, 7:12729, 2016.

[113] S. W. Hell and J. Wichman. Breaking the diffraction resolution limit by stimulated emission: stimulated-emission-depletion fluorescence microscopy. *Optics Letters*, 19(11):780 – 782, 1994.

[114] S. T. Hess, T. P. K. Girirajan, and M. D. Mason. Ultra-High Resolution imaging by Fluorescence Photoactivation Localization Microscopy. *Biophysical Journal*, 91:4258–4272, 2006.

[115] M. J. Rust, M. Bates, and X. Zhuang. Sub-diffraction-limit imaging by stochastic optical reconstruction microscopy (STORM). *Nature Methods*, 3(10):793–795, 2006.

[116] J Schneider, J Zahn, M Maglione, S J Sigrist, J Marquard, J Chojnacki, H G Krausslich, S J Sahl, J Engelhardt, and S W Hell. Ultrafast, temporally stochastic STED nanoscopy of millisecond dynamics. *Nat Methods*, 12(9):827–830, 2015.

[117] S. A. Jones, S. H. Shim, J. He, and X. Zhuang. Fast, three-dimensional super-resolution imaging of live cells. *Nature Methods*, 8(6):499–505, 2011.

[118] P. Kanchanawong, G. Shtengel, A. M. Pasapera, E. B. Ramko, M. W. Davidson, H. F. Hess, and C. M. Waterman. Nanoscale architecture of integrin-based cell adhesions. *Nature*, 468:580–584, 2010.

[119] N. Ji, D. E. Milkie, and E. Betzig. Adaptive optics via pupil segmentation for high-resolution imaging in biological tissues. *Nature methods*, 7(2):141–147, 2010.

[120] D. B. Phillips, J. A. Grieve, S. N. Olof, S. J. Kocher, R. Bowman, M. J. Padgett, M. J. Miles, and D. M. Carberry. Surface imaging using holographic optical tweezers. *Nanotechnology*, 22:1–7, 2011.

[121] Y. Nakayama, P. J. Pauzauskie, A. Radenovic, R. M. Onorato, R. J. Saykally, J. Liphardt, and P. Yang. Tunable nanowire nonlinear optical probe. *Nature*, 447:1098–1101, 2007.

[122] S. M. Moghimi and A. C. Hunter. Poloxamers and poloxamines in nanoparticle engineering and experimental medicine. *Trends in Biotechnology*, 18:412–420, 2000.

[123] P. C. Seitz, E. H. K. Stelzer, and A. Rohrbach. Interferometric tracking of optically trapped probes behind structured surfaces: a phase correction method. *Applied optics*, 45(28):7309–7315, 2006.

[124] M. J. Schnitzer and S. M. Block. Kinesin hydrolyses one ATP per 8-nm step. *Nature*, 388:386–390, 1997.

[125] Z. Zhang and C.-H. Menq. Three-dimensional particle tracking with subnanometer resolution using off-focus images. *Applied optics*, 47(13):2361–2370, 2008.

[126] W. Mickel, S. Münster, L. M. Jawerth, D. A. Vader, D. A. Weitz, A. P. Sheppard, K. Mecke, B. Fabry, and G. E. Schröder-Turk. Robust Pore Size Analysis of Filamentous Networks from Three-Dimensional Confocal Microscopy. *Biophysical journal*, 95:6072–6080, 2008.

[127] P. Wu, R. Huang, C. Tischer, A. Jonas, and E.-L. Florin. Direct Measurement of the Nonconservative Force Field Generated by Optical Tweezers. *Physical Review Letters*, 103:108101–1–108101–4, 2009.

[128] S. Jeney, E. H. K. Stelzer, H. Grubmüller, and E.-L. Florin. Mechanical Properties of Single Motor Molecules Studied by Three-Dimensional Thermal Force Probing in Optical Tweezers. *ChemPhysChem*, 5:1150–1158, 2004.

[129] Z. Feng, W. N. Chen, P. V. S. Lee, K. Liao, and Vi. Chan. The influence of GFP-actin expression on the adhesion dynamics of HepG2 cells on a model extracellular matrix. *Biomaterials*, 26:5348–5358, 2005.

[130] M. Deibler, J. P. Spatz, and R. Kemkemer. Actin Fusion Proteins Alter the Dynamics of Mechanically Induced Cytoskeleton Rearrangement. *PLoS ONE*, 6(8):e22941, 2011.

[131] F. Hajizadeh and S. N. S. Reihani. Optimized optical trapping of gold nanoparticles. *Optics Express*, 18(2):551–559, 2010.

[132] J. D. Jackson. *Classical Electrodynamics*. Wiley, New York, NY, 1999.

[133] A. Andres-Arroyo, B. Gupta, F. Wang, J. J. Gooding, and P. J. Reece. Optical manipulation and spectroscopy of silicon nanoparticles exhibiting dielectric resonances. *Nano Letters*, 16:1903–1910, 2016.

[134] M. E. Janson and M. Dogterom. A Bending Mode Analysis for Growing Microtubules: Evidence for a Velocity-Dependent Rigidity. *Biophysical journal*, 87:2723–2736, 2004.

[135] J. C. Meiners and S. R. Quake. Femtonewton Force Spectroscopy of Single Extended DNA Molecules. *Physical Review Letters*, 84(21):5014–5017, 2000.

[136] J. Steinwachs, C. Metzner, K. Skodzek, N. Lang, I. Thiesvessen, C. Mark, S. Münster, K. Aifantis, and B. Fabry. Three-dimensional force microscopy of cells in biopolymer networks. *Nature Methods*, 13:171–176, 2016.

[137] E. N. Lissek, T. F. Bartsch, and E.-L. Florin. Resolving Filament Level Mechanics in Collagen Networks using Activity Microscopy. *bioarXiv*, 382903, 2018.

[138] P. Fratzl. *Collagen Structure - Structure and Mechanics.* Springer Science+Business Media, LLC, New York, NY, New York, NY, 2008.

[139] S. V. Murphy and A. Atala. 3D bioprinting of tissues and organs. *Nature Biotechnology*, 32(8):773–785, 2014.

[140] K. M. Park, Y. M. Shin, K. Kim, and H. Shin. Tissue Engineering and Regenerative Medicine 2017: A Year in Review. *Tissue Engineering Part B: Reviews*, 00(00), 2018.

[141] K. Wang, L.-H. Cai, B. Lan, and J. J. Fredberg. Hidden in the mist no more: physical force in cell biology. *Nature Methods*, 13(2):124–125, 2016.

[142] A. Malandrino, M. Mak, R. D. Kamm, and E. Moeendarbary. Complex mechanics of the heterogeneous extracellular matrix in cancer. *Extreme Mechanics Letters*, 21:25–34, 2018.

[143] J. Kim, J. Feng, C. A. R. Jones, X. Mao, L. M. Sander, H. Levine, and B. Sun. Stress-induced plasticity of dynamic collagen networks. *Nature Communications*, 8(842):1–7, 2017.

[144] M. W. Allersma, F. Gittes, M. J. DeCastro, R. J. Stewart, and C. F. Schmidt. Two-Dimensional Tracking of ncd Motility by Back Focal Plane Interferometry. *Biophysical Journal*, 74:1074–1085, 1998.

[145] D. Vader, A. Kabla, D. Weitz, and L. Mahadevan. Strain-Induced Alignment in Collagen Gels. *PLoS ONE*, 4(6):e5902, 2009.

[146] S. L. Schor. Cell proliferation and migration on collagen substrata in vitro. *Journal of Cell Science*, 41:159–175, 1980.

[147] T. Elsdale and J. Bard. Collagen substrata for studies on cell behavior. *The Journal of Cell Biology*, 54:626–637, 1972.

[148] A. J. Licup, A. Sharma, and F. C. Mackintosh. Elastic regimes of subisostatic athermal fiber networks. *Physical Review E*, 93:012407–1–012407–12, 2016.

[149] T. M. Koch, S. Münster, N. Bonakdar, J. P. Butler, and B. Fabry. 3D Traction Forces in Cancer Cell Invasion. *PLoS ONE*, 7(3):e33476, 2012.

[150] S. I. Fraley, Y. Feng, R. Krishnamurthy, D.-H. Kim, A. Celedon, G. D. Longmore, and D. Wirtz. A distinctive role for focal adhesion proteins in three-dimensional cell motility. *Nature Cell Biology*, 12(6):598–604, 2010.

[151] M. T. Kasimir, E. Rieder, G. Seebacher, G. Silberhumer, E. Wolner, G. Weigel, and P. Simon. Comparison of different decellularization procedures of porcine heart valves. *The International Journal of Artificial Organs*, 26(5):421–427, 2003.

[152] T. W. Hudson, S. Y. Liu, and C. E. Schmidt. Engineering an Improved Acellular Nerve Graft via Optimized Chemical Processing. *Tissue Engineering*, 10(9-10):1346–1358, 2004.

[153] N. Vyavahare, M. Ogle, F. J. Schoen, R. Zand, D. Claire Gloeckner, M. Sacks, and R. J. Levy. Mechanisms of bioprosthetic heart valve failure: Fatigue causes collagen denaturation and glycosaminoglycan loss. *Journal of Biomedical Materials Research*, 46(1):44–50, 1999.

[154] C. Martin and W. Sun. Simulation of long-term fatigue damage in bioprosthetic heart valves: effects of leaflet and stent elastic properties. *Biomechanics and Modeling in Mechanobiology*, 13:759–770, 2014.

Vita

Emanuel Norbert Lissek was born in Frankfurt am Main, Germany in 1988, and grew up north of the city in a small town called Echzell. After graduating with his Abitur from the prestigious Augustinerschule Friedberg in 2008, he went on to complete a year of civil service working with learning disabeled young adults. In 2009 Emanuel started his undergraduate studies in Physics at the Leipzig University in Leipzig, Germany with a research focus in material design for biophysical applications. Finally, in the Fall 2012 Emanuel moved to Austin, Texas to pursue his Ph.D. in Physics, and joined the laboratory of Prof. Ernst-Ludwig Florin, focusing on the experimental study biopolymer networks.

This dissertation was typeset with LaTeX[†] by the author.

[†] LaTeX is a document preparation system developed by Leslie Lamport as a special version of Donald Knuth's TeX Program.